UNIVERSIDADE DE LISBOA
FACULDADE DE CIÊNCIAS
DEPARTAMENTO DE FÍSICA

Emission channeling studies of Indium Phosphide at low temperatures at CERN-ISOLDE.

Lígia Marina Pinto de Almeida Amorim

Mestrado em física - ramo física nuclear e partículas

2009

UNIVERSIDADE DE LISBOA
FACULDADE DE CIÊNCIAS
DEPARTAMENTO DE FÍSICA

Emission channeling studies of Indium Phosphide at low temperatures at CERN-ISOLDE.

Lígia Marina Pinto de Almeida Amorim

Mestrado em física - ramo física nuclear e partículas

Oriented by
Professor Luis Peralta - FCUL
Dr. Ulrich Wahl - ITN

2009

UNIVERSIDADE DE LISBOA
FACULDADE DE CIÊNCIAS
DEPARTAMENTO DE FÍSICA

Emission channeling studies of Indium Phosphide at low temperatures at CERN-ISOLDE.

Lígia Marina Pinto de Almeida Amorim

Mestrado em física - ramo física nuclear e partículas

Oriented by
Professor Luis Peralta - FCUL
Dr. Ulrich Wahl - ITN

Coordination with CERN-ISOLDE by
Dr. João Guilherme Correia

Lisboa
2009

Acknowledgements

To my supervisors in the front page without whom this work was impossible
and all the silent teachers to howm I own my growth along my path:

In ISOLDE-CERN

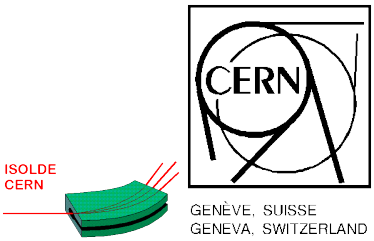

(a) (b)

The coordination with CERN-ISOLDE
Dr. João Guilherme Correia,
who made a scientist out of me, despite the endless sweat and patience that meant. But abouve for taking a chance on me.

In Instituto Tecnológigo e Nuclear

The coordination of the RBS-C study
Dr.Edurado Alves, who infected work with joy and enthusiasm at ITN, and
Dr.Carlos Marques, who showed me every step of RBS.

In Centro de Física Nuclear

The coordination of the cooling station
Prof. Ribeiro da Sílva, who taught me how to tighten screws, introduced instrumentation to my hands, technology to my mind and made a handyman out of me.

To my family and friends:

Thanks to my husband who gave me the strength and love I needed, even in the times he missed me the most.
Thanks to the rest of the family for the constructive criticism, stress is necessary to motivate change.

To all the group I have been working with, for being so tight and making me a part of it, providing a fruitfull interaction.

Resumo da Tese

O trabalho desta tese consiste no estudo do sistema InP (semicondutor III-V Fosfeto de Índio) a baixa temperatura, com a técnica de "canalização electrónica" que usa amostras implantadas com isótopos radioactivos no acelerador ISOLDE - CERN [1]. Assim, no âmbito deste trabalho, foram implantados átomos radioactivos de ^{111}In num mono-cristal de InP. Após o recozimento da amostra, para que a rede cristalina desta recuperasse dos defeitos provocados pela implantação, foi estudada a localização do isótopo $^{111}In/^{111}Cd$ na rede, com a técnica de "canalização electrónica". Este estudo foi feito para várias temperaturas desde a temperatura ambiente (300K) até aos 50k em intervalos de 50K.

A técnica de "canalização electrónica" permite determinar com grande precisão ($< 0,02nm$) a posição de átomos nas redes cristalinas. Com a vantagem única da informação obtida ser específica dos núcleos radioactivos introduzidos nos materiais a estudar e de permitir usar pequenas doses ($< ppm$) de implantação.

Os átomos radioactivos decaem emitindo partículas carregadas, estas partículas atravessam o cristal interagindo com os átomos do cristal. Utilizando amostras mono-cristalinas a simetria da disposição dos átomos no cristal dão origem à canalização das partículas carregadas emitidas. Isto é, se considerarmos que as partículas emitidas são negativas (electrões de conversão, β^-) e que estas têm uma trajectória inicial com um ângulo inferior ao "ângulo crítico", em relação a um eixo principal do cristal, elas são atraídas pelos centros positivos dos átomos desse eixo, sendo canalizadas nesta direcção. Por outro lado se forem positivas (α^{2+}, β^+), as partículas são repelidas pelos centros dos átomos, sendo canalizadas não pelos eixos principais do cristal mas pelo espaço intersticial entre átomos. Como exemplo: se os isótopos implantados ocuparem uma posição que está perto da posição substitucional da rede numa certa direcção, as partículas (negativas) emitidas nessa direcção serão canalizadas. No entanto para os isótopos que estiverem desviadas de posições regulares da rede será mais difícil de conseguir o efeito de canalização, ao longo destes eixos. Desta forma é possível determinar a localização na rede do isótopo implantado detectando a intensidade de partículas que saem do cristal numa distribuição bi-dimensional (XY), correspondentes a projecção de diferentes orientações principais do cristal, por triangulação.

O decaimento do ^{111}In para estados excitados ^{111}Cd é por captura electrónica, não fornece energia de recuo suficiente para que o ^{111}Cd se liberte da rede e se reposicione. Assume-se assim que o decaimento dos estados excitados do ^{111}Cd, com emissão de electrões de conversão tem como origem a posição natural do isótopo ^{111}In na rede de InP. No caso deste estudo não foi o decaimento do isótopo implantado $^{111}In \rightarrow {}^{111}Cd$ que deu origem aos electrões detectados, mas sim o decaimento do próprio ^{111}Cd excitado, resultante do primeiro decaimento, para o seu estado fundamental.

A câmara de canalização electrónica "on-line" aplica-se numa linha de feixe do ISOLDE, permitindo in-situ a implantação, o recozimento e a aquisição de dados. Desta forma evita-se a perca de actividade durante o processo de preparação e montagem da amostra. Este "setup" é utilizado preferencialmente para o estudo de localização de elementos com isótopos de tempo de vida média curtos, desde algumas horas até segundos.

No âmbito da cadeira de estágio deste mestrado, desenvolveu-se um sistema de criogenia na câmara "on-line" para permitir a descida da temperatura da amostra até aos 50k durante a implantação e durante as medidas. Até este trabalho não era possível estudar no ISOLDE o comportamento individual de elementos específicos da rede, impurezas ou constituintes com a diminuição da temperatura. Desta forma este trabalho teve como objectivo predominate (entre outros) testar os limites e capacidade do sistema concebido para experiências de "canalização electrónica" a baixa temperatura. No futuro a implementação de medidas a baixa temperatura com a técnica de canalização de electrões vai permitir estudar fenómenos de natureza incoerente nas redes cristalinas e/ou a localização de impurezas implantadas a baixa temperatura.

O sistema InP representa um caso ideal de estudo por duas razões. A primeira é que sendo este composto um semicondutor foto-sensível com importantes aplicações tecnológicas, os seus parâmetros de rede são bem conhecidos para uma larga gama de temperaturas. A segunda razão é que se trata de um material que apresenta

[1] O "On-Line Isotope Mass Separator" ISOLDE é uma infraestrutura dedicada à produção de uma grande variedade de feixes de isótopos radioactivos para as mais variadas experiências.- http://isolde.web.cern.ch/ISOLDE/

uma baixa constante de Debye, o que implica que as variações das vibrações atómicas com a temperatura são significativas, influenciando o efeito de "dechanneling", concorrente com a "canalização electrónica", que é provocado, entre outras coisas, pelas vibrações térmicas dos átomos na rede. Desta forma este composto representa um sistema padrão para estudar e interpretar os espectros de "canalização de electrões" a baixa temperatura.

A apresentação desta tese está dividida nos seguintes temas:

- No capitulo 2 são apresentados os princípios físicos da "canalização electrónica" e o contexto teórico em que se inserem, incluindo uma descrição detalhada do procedimento experimental das técnicas de "canalização electrónica" e de "Rutherford Backscattering" (RBS) e a teoria de interações de partículas carregadas com os átomos do cristal, com a definição dos parâmetros mais relevantes como ângulo crítico e poder de paragem.

- O capitulo 3 é dedicado à descrição da parte experimental deste trabalho. Desta forma caracteriza-se o sistema estudado, dando especial atenção às características do composto InP e do isótopo ^{111}In.

- Os resultados obtidos nesta experiência, assim como a sua análise são apresentados no capitulo 4.

  Primeiro é descrita a preparação da amostra, com a sua implantação e recozimento.

  Depois são incluídos os gráficos que representam os dados. São referidos os parâmetros utilizados nas simulações e os resultados das correlações dos dados adquiridos e simulados.

- Esta tese acaba no capitulo 5, com a discussão dos resultados, dos factores que podem ter influenciado os dados e com a proposta de estudos no seguimento desta tese.

- Todos os dados relevantes para a análise dos dados ou para as simulações, que sejam adjacentes ao trabalho em si, são adicionados em anexo:

  No anexo A estão dispostos todos os dados encontrados na literatura para utilizar nas simulações associados à r.m.s. de deslocamento. Os valores utilizados estão descritos na secção 3.1.

  No anexo B são descritos em maior detalhe os procedimentos da técnica de RBS-channeling.

  No anexo C expõem-se, a termo ilustrativo, a variedade de isótopos disponível para o elemento In no ISOLDE.

  O anexo D compila os valores de energia de ligação atómica dos elementos até ao Rf.

Como estudo complementar da "canalização electrónica" o RBS-channeling (Rutherford Backscattering Channeling) foi usado no estudo de uma amostra de InP. Este estudo é apresentado neste trabalho como ilustração do método e procedimento.

Neste trabalho comprova-se que o sistema de refrigeração da experiência funcionou em condições (durante cerca de uma semana) entre os 50K e a temperatura ambiênte proporcionando uma temperatura relativamente estável com oscilações de cerca de um grau. Conforme esperado a diminuição da temperatura é observada nos resultados experimentais. Durante o processo de análise dos dados foram encontrados alguns problemas que parecem estar associados com limitações na simulação do efeito de "dechanneling" para InP, possivelmente por se tratar de um compsto com elementos pesados. Este problema parece ser mais relevantes a temperaturas mais elevadas (mais próximas da temperatura ambiente). Para além disso houve um problema de contaminação, que embora não se conseguisse determinar a origem, de concentração desprezável.

Como estudo complementar é sugerido que se estude a influencia do recozimento da rede de InP no a "canalização electrónica", isto é, estudo de "canalização electrónica" em função da temperatura de recozimento da amostra. É importante também que se repita a experiência com uma energia de implantação diferente, desta forma varia-se o "dechanneling" com vista em testar o modelo de cálculo do efeito de "dechanneling". No futuro pretende-se evoluir para o estudo do comportamento de impurezas em função da temperatura de implantação, em sistemas semiconductores e isolantes.

Abstract

^{111}In radioactive atoms were implanted into a single crystal of InP. After annealing for lattice recovery of implantation defects, the lattice site location of $^{111}In/^{111}Cd$ was studied with the emission channeling technique, from room temperature (300K) down to 50K at CERN-ISOLDE [2].

This work aims to test a recently developed cooling station for emmission channeling experiments. InP is a material with a relatively low Debye temperature, where significant changes of atomic vibrations are expected with temperature, thus providing an ideal test ground of the effects, which can be expected to influence the data, i.e., dechanneling from lattice vibration and changes of the root mean square displacement (r.m.s.) of the atomic position of the probe atom.

In the future we intend to apply these studies to monitor individual impurities or lattice constituents, with temperature, upon phase transitions as well as studying lattice sites of dopants implanted at low temperature.

[2]"The On-Line Isotope Mass Separator ISOLDE is a facility dedicated to the production of a large variety of radioactive ion beams for a great number of different experiments" http://isolde.web.cern.ch/ISOLDE/

Contents

1 Motivation/Resume

Many macroscopic properties of materials depend on microscopic phenomena, which are activated by temperature. Two examples from the many interesting subjects and systems to study, e.g., the annealing of defects that are generated upon implantation of impurity elements, which can be frozen in specific configurations at low temperatures and on a different context, the study of intrinsic phenomena where electric, magnetic and lattice parameters are coupled as it happens at the copper planes of high-Tc superconductors upon the superconducting transition. These might lead to the local anisotropy of atomic relaxations and vibrations, which can, in principle be studied quantitatively by emission channeling at low temperatures.

The emission channeling technique consists in the detection of charged particles, originating from the radioactive decay of implanted ions inside a single crystal, to study the location of impurity elements in the crystalline structure.

At the microscopic scale emission channeling provides the tracking of position and vibration of radioactive isotopes, the probing elements, in a single crystal. At ISOLDE, almost all of the periodic table elements can be envisaged to study, easily providing the appropriate isotope of an element of interest. The InP (III-V semiconductor) was chosen to study due to the relatively small Debye temperature and expected noticeable anisotropy of atomic vibrations as a function of temperature. The viability of performing electron emission channeling at low temperatures was studied looking for ways to expand possibilities and applications of the emission channeling technique to low temperature measurements.

The presentation of this work follows in this order:

- On chapter 2 the physical principles of channeling and its theoretical background are presented. In the applied case of "electron emission channeling" and of "Rutherford Backscattering" (RBS) spectometry the description is detailed. The theory of the interaction of charged particles with crystal atoms is discussed along with the definition of the most important parameters for this phenomenon, as critical angle and stopping power.

- The chapter 3 is dedicated to the experimental overview of this work. As such the system of study and setup are characterized, in particular the most relevant features of the compound InP and of the isotope ^{111}In.

- The results of this experiment along with their analyses are gathered in the chapter 4. First the preparation of the sample, with the implantation of the radioactive isotope and annealing are described. Then the measurements are presented. The simulations are briefly approached and the fitting of the measurements with the simulations are again compiled in plots.

- This work ends with a discussion, chapter 5, of the results obtained, the aspects that influenced them and the consideration of future work that would complement these results in order to obtain further conclusions.

- All data relevant for this work that is more specific or requires a more detailed description is compiled in the appendices:

  In the appendix A the data used to calculate the root mean square (r.m.s.) displacement is gathered from all data found in the literature. As one can find from this appendix there are many discrepant

values of Debey temperature as function of temperature and even of r.m.s. displacement for the room temperature. The values used are described in section 3.1.

A detailed RBS procedure, for characterizing an InP sample, is exemplified in appendix B. The work presented in this appendix was part of the earlier development of this experiment.

An illustration of the variety of the isotopes available merely for the indium element at ISOLDE is compiled in the appendix C.

For purposes of consult, further in this presentation the atomic-electron binding energies are tabulated in appendix D

2 About channeling

2.1 Channeling Effect

A crystal is a solid in which the constituent atoms are arranged regularly, repeating a pattern periodically in all three spatial dimensions. At the atomic scale a crystal is rather empty, since the atoms have a small positively charged nucleus and a low density negatively charged electron cloud, made of more localized electrons in the deepest atomic electron's shells and the ones which are essentially shared, populating the levels of the band structure that is characteristic of the solid. This way the Coulomb potential $\left(V(r) = \frac{q_1 q_2}{r}\right)$ between "the travelling charge" and each (many) body (electrons and the nuclei of the crystal) is alltogether transformed into a screened Coulomb potential

$$V(r) = \frac{q_1 Z q_2}{r} \phi\left(\frac{r}{a}\right) \tag{2.1}$$

between two bodies, the "travelling" charge and the positive centers of the crystal, where q_1 and q_2 are the charges of the two bodies respectively, Z is the charge of the nucleus, a is the Bohr radius and r is the distance between them. The screening function assures the boundary conditions, it forces the potential to behave as the coulomb potential for small radius, $\phi\left(\frac{r}{a}\right) \rightarrow 1$ for $r \rightarrow 0$ and limits the potential when the radius rises, $\phi\left(\frac{r}{a}\right) \rightarrow 0$ for $r \rightarrow \infty$.

The result is that a negatively/positively charged particle travelling inside a crystal will be attracted/repelled by the atoms, where there is an atomic positive core (accordingly to the screened potential). Since the crystal has a repeated pattern of atoms, there are directions in which the atoms are aligned in planes (crystal principal planes) and in strings (crystal principal axis).

If a negatively charged particle is traveling, inside a crystal, in a direction that makes a small angle with a crystal axis/plane, the particle is continuously attracted slightly bound to the axis direction/plane and is channeled through it. This effect is known as channeling. If on the other hand the travelling particle is positively charged it will be repelled positive centers of the parallel planes/axis and will then be preferentially confined near the center of the channels.

Particles emitted with large angles, regarding a preferential orientation, will not be channeled, being randomly scattered to other directions.[1] For a better understanding the figure 2.1 shows the interactions concepts for each case of negative and positive particles emitted from different lattice sites.

The channeling effect is detected by comparison between the yield of particles coming out of the crystal in different orientations. A direction of the crystal through which the channeling occurs has a bigger/smaller number of charged particles aligned with it depending on wether the particle is negative or positive. In the figure 2.1 the small plots of yield in the end of each direction ($\{100\}$, $\{110\}$, $\{111\}$) represent the yield variation within a small angle around those directions. When there is an increase of the yield due to the channeling the plot line is green and in red is represented the lowering of the yield due to the blocking effect.

Within a typical angle of $\pm 3^o$ angular range the intensity yield varies very much depending on the position of an impurity on the crystal lattice. By measuring those anisotropies along several principal directions of the lattice, two main techniques, Rutherford Backscattering channeling and emission channeling, provide unique high precision information about lattice sites of impurities and of their root mean square displacement-r.m.s., either due to vibrations or due to the interaction of impurities with lattice point defects.

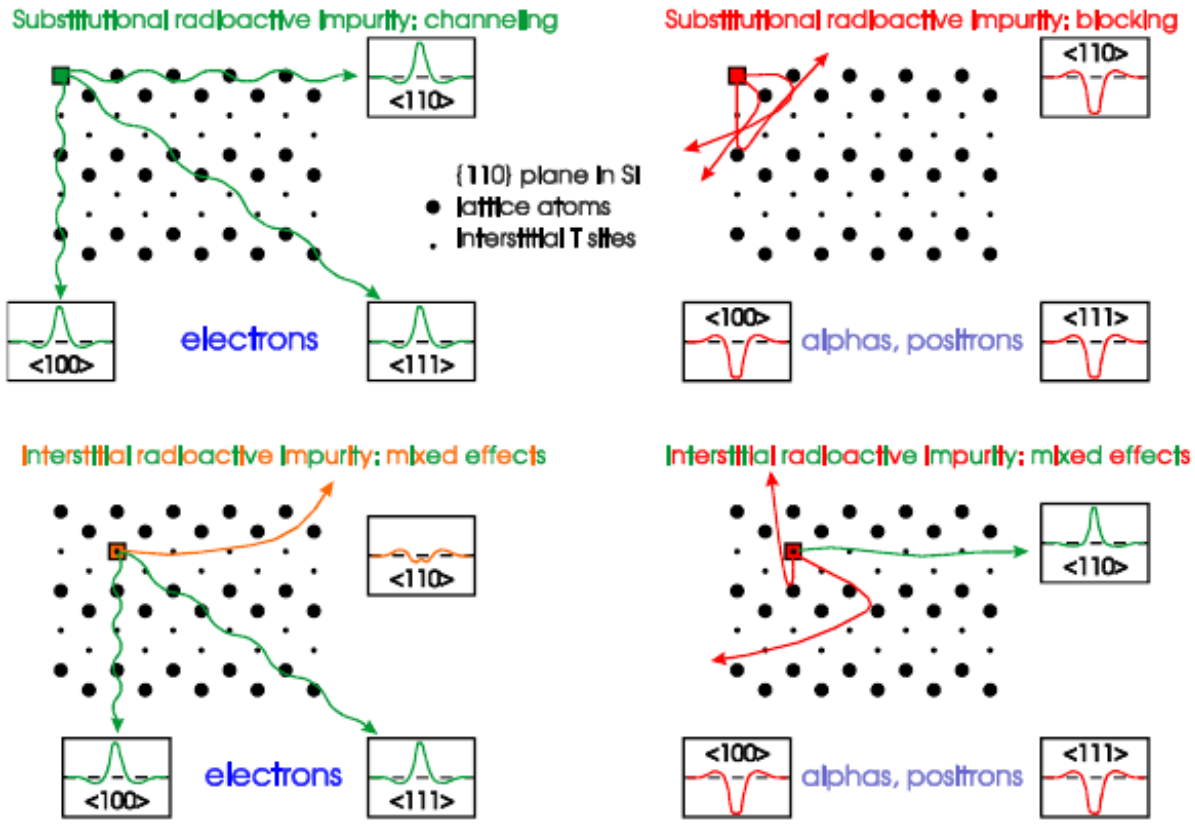

Figure 2.1: Channeling and blocking effects [1] in emission channeling experiments. The upper figure on the left/right illustrates the channeling/blocking of a negatively/positively charged particle (an electron/alpha particle) by the positive centers of the atoms of a crystal, when the particle is emitted from a substitutional position along the $< 100 >$, $< 110 >$ and $< 111 >$ axial directions. The lower figure on the left illustrates the blocking effect of a negatively charged particle (an electron), when the particle is emitted from an interstitial position where blocking is measured for $< 110 >$ and channeling $< 100 >$ and $< 111 >$. The lower figure on the right illustrates the channeling effect of a positively charged particle, when the particle is emitted from an interstitial position in-between planes with channeling, along the $< 110 >$ direction and blocking effect is observed along the axial directions $< 100 >$ and $< 111 >$.

Rutherford Backscattering channeling

Rutherford Backscattering (RBS) is performed with the help of a probing beam generally He^+, $2 - 3MeV$, ions produced by a small Van De Graaff accelerator (see figure 3.5). The collision with an atom results in scattering of the probe beam, being the backscattered probes those that had one quasi frontal collision. The energy of the probe after the collision is used to identify the element it was scattered by. In other words, by measuring the energy of the backscattered particles this technique provides the study of the target's composition.

The probing ions lose energy continuously, when travelling in and out of the crystal, due mainly to the interactions with the atomic electrons of the compound to study. This allows to probe the composition stoichiometry as function of depth, by measuring the energy of the backscattered outgoing particles. However this effect also contributes to hinder the study of the constituents with lighter masses. This is due to the fact that the probing particles have less energy upon collision with light elements than with heavy ones. Consequently the yield of backscattered particles from light elements can not be properly distinguished from the yield of particles that hit heavier elements deeper on the matrix and loose more energy on their way in and out of the target.

Emission channeling

The "emission channeling" technique (EC) uses radioactive impurities implanted into a single crystal to emit the charged probes. The advantage of EC is that there is a number of β and α particle emitter isotopes providing positive $\alpha = He^{2+}$ and negative $\beta =$ electron probes. Any light or heavy element, if radioactive, will emit well identified probes, which can be channelled and used for lattice location experiments.

The high precision of emission channeling is also due to the use of bi-dimensional position sensitive electron detectors, which raises the gain factor for four orders of magnitude of sensitivity, regarding RBS channeling. Hence lower doses can be used, the measurement is more realistic for any available element and the damage to the sample involved in the process of implantation is reduced.

The advantage of being at ISOLDE is the fact that about 800 isotopes of 80 elements (see figure 3.9) are produced there, from which we can almost always find the appropriate one, of the elements in interest to use in each case of study.

2.2 Interaction of charged particles with the crystal atoms

The interaction of charged particles inside a solid are mainly of Coulombian nature, and in the case of electrons they are described by the potential [1]:

$$V(r) = \frac{Z_1 Z_2 e^2}{r} \phi\left(\frac{r}{a}\right), \tag{2.2}$$

a screened potential with a term $\phi\left(\frac{r}{a}\right)$ that applies the boundary conditions, where a is the screening radius.

Many screened Coulomb potentials were conceived empirically in the attempt to describe the interactions of a fast moving ion, of charge $Z_1 e$, with ions, of charge $Z_2 e$, in a solid. The two potentials below are the ones that better described the channeling effect[1]:

- Lindhard's potential was thought to be analytically simple when averaged as a continuum potential, which is very important for the channeling techniques.

$$V_{Lindhard}(r) = \frac{Z_1 Z_2 e^2}{r}\left(1 - \frac{\frac{r}{a}}{\sqrt{(\frac{r}{a})^2 + 3}}\right), \tag{2.3}$$

  where $a = 0.8853 a_0 \left(z_1^{\frac{1}{2}} + z_2^{\frac{1}{2}}\right)^{-\frac{2}{3}}$ depends on the Bohr radius a_0.

- ZBL-potential is based on simple sum of exponentials.

$$V_{ZBL}(r) = \frac{Z_1 Z_2 e^2}{r} \sum_{i=1}^{4} \alpha_i e^{-\frac{\beta_i r}{a_{ZBL}}}, \tag{2.4}$$

  where the coefficients $\alpha i = (0.1818, 0.5099, 0.2802, 0.02817)$, $\beta i = (3.2, 0.9423, 0.4029, 0.2106)$, and the ZBL screening radius $a_Z BL = \frac{0.8853 a_0}{Z_1^{0.23} + Z_2^{0.23}}$.

The channeling effect of high-energy particles in a crystal can be described using a continuum approximation of the potential. Although this approximation is useful to illustrate the effect it is hard to include atom vibrations and disable the description of defects. The treatment of data is therefore done numerically, using binary collision Monte Carlo methods for the case, e.g., of heavier positive particles as α^{2+}. In order to simplify, and to explain the stopping power and critical angle its considered that the potential seen by an energetic particle in a crystal is continuous, although the Monte Carlo binary collisions used for the simulations don't use this approximation.

The continuum approximation potential $U(R)$, for any of the screened potentials $V(R)$, is obtained by[1]:

- considering the channeling of a string of atoms and averaging the atomic potential along the direction of

the string on the z direction,

$$U(R) = \frac{1}{d}\int_{-\infty}^{\infty} V(\sqrt{x^2+y^2+z^2})dz \Rightarrow$$
$$U(R) = \frac{2Z_1Z_2e^2}{d}\int_0^{\infty} \frac{\phi\left(\frac{\sqrt{R^2+z^2}}{a}\right)}{\frac{\sqrt{R^2+z^2}}{a}}\frac{1}{a}dz, \tag{2.5}$$

where $R = \sqrt{(x^2+y^2)}$, d is the distance between atoms in the row.

- considering the channeling by planes of atoms and averaging the atomic potential in two dimensions parallel to the plane on x-z,

$$\begin{aligned} U(y) &= \frac{1}{A_p}\int_{-\infty}^{\infty} V(\sqrt{x^2+y^2+z^2})dxdz = \\ &= \frac{1}{A_p}\int_{-\infty}^{\infty} V(\sqrt{R^2+y^2})2\pi RdR \Rightarrow \\ U(y) &= \frac{2\pi Z_1Z_2e^2}{A_p}\int_0^{\infty} \frac{\phi\left(\frac{\sqrt{R^2+y^2}}{a}\right)}{\frac{\sqrt{R^2+y^2}}{a}}\frac{R}{a}dR, \end{aligned} \tag{2.6}$$

where y is the distance to the plane, A_p is the unit area per atom in the plane and $R = \sqrt{(x^2+z^2)}$.

2.3 Channeling through a critical angle

The charged particles resulting from the decay are emitted isotropically. If the particle is emitted within a critical angle of a crystal preferential orientation (crystal axis or plane), the channeling effect will be enough to confine the particle trajectory in the preferential orientation. The critical angle is then the largest angle a particle can have, with an axis or plane, that allows the channeling effect (Fig. 2.2).

Neglecting the slowing of the particle along the axial orientation, the energy is kept constant in that direction, $E_{//} = C^{ste}$, then the perpendicular values of energy $E_\perp = C^{ste}$ must also remain constant, as the total energy value E_0 is invariant.

$$E_\perp = E_{p\perp} + E_{k\perp} = C^{ste} \approx E_0\phi^2 + E_{K\perp} \tag{2.7}$$

Where $E_{p\perp}$ is the perpendicular potential energy and $E_{k\perp}$ is the perpendicular kinetic energy. The critical angle $\psi_{critical}$ is the highest angle, the trajectory undergoes with the axial orientation and is reached when the particle crosses the center line of the channel. Its values can be expressed by means of the potential energy at the critical point when the perpendicular energy is zero at the minimum proximity distance.

$$E_{K\perp}(r_{min}) = 0 \tag{2.8}$$

So the critical angle $\psi_{critical}$ is estimated by considering the form on eq.2.10:

$$\begin{cases} E_0\psi^2 = E_p(r_{min}) \\ p_\perp = p\sin\psi \approx p\psi \text{ for small angles and} \end{cases} \Rightarrow \tag{2.9}$$

$$\begin{aligned} E_{k\perp} &= \frac{p_\perp^2}{2m} = \frac{P_0^2\psi^2}{2m} \Rightarrow \\ \psi_{critical} &= \sqrt{\frac{E_p(r_{min})}{E_0}}. \end{aligned} \tag{2.10}$$

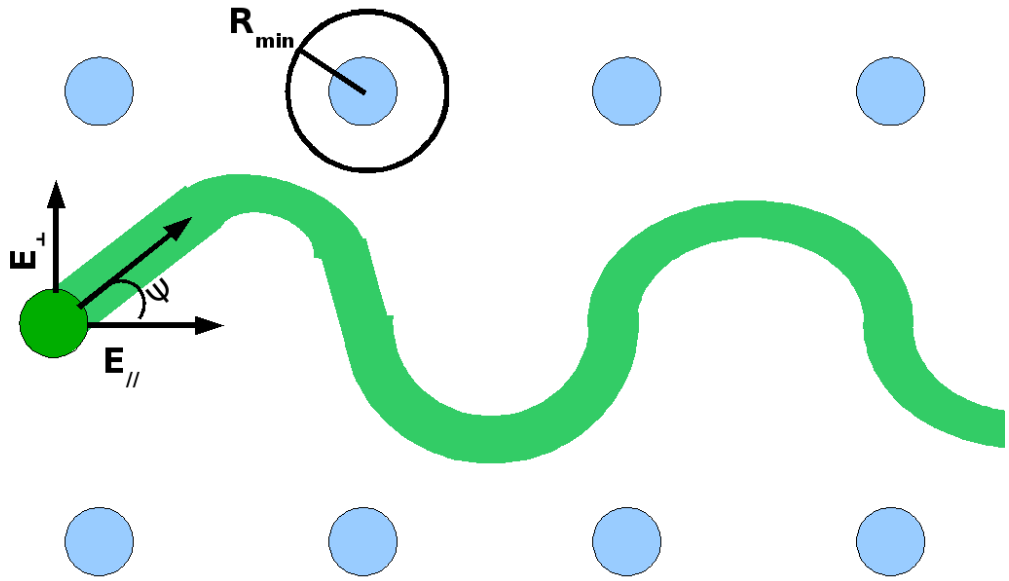

Figure 2.2: Two dimensional critical angle schema

Considering a string of atoms interacting with a charged particle and using the respective potential, the critical angle becomes [1]:

$$\psi_{critical} = \sqrt{\frac{2Z_1Z_2e^2}{d\,E_0}}\sqrt{\int_0^\infty \frac{\phi\left(\frac{\sqrt{R^2+z^2}}{a}\right)}{\frac{\sqrt{R^2+z^2}}{a}}dz}. \tag{2.11}$$

For heavy particles with high energy, when the angle ψ is smaller than the ratio of the screening radius, a, and the distance between atoms in the string, d, the critical angle is

$$\psi_{critical} = \sqrt{\frac{2Z_1Z_2e^2}{d\,E_0}}, \tag{2.12}$$

i. e., when the energy is higher than:

$$E_0 > \frac{2Z_1Z_2e^2d}{a^2}. \tag{2.13}$$

For lower energies or light particles, such as electrons, it becomes

$$\psi_{critical} = \sqrt{\frac{\sqrt{3}a}{\sqrt{2}d}\sqrt{\frac{2Z_1Z_2e^2}{d\,E_0}}}. \tag{2.14}$$

The same way, the channeling along planar crystallographic directions occurs when the charged particle is under an angle lower than the critical angle with a principal plane [1]:

$$\psi_{critical} = \sqrt{\frac{2\pi Z_1Z_2e^2}{A_pE_0}}\sqrt{\int_0^\infty \frac{\phi\left(\frac{\sqrt{R^2+y^2}}{a}\right)}{\frac{\sqrt{R^2+y^2}}{a}}\frac{R}{a}dR}. \tag{2.15}$$

This becomes

$$\psi_{critical} = \sqrt{\frac{2\pi Z_1 Z_2 e^2 a}{A_p E_0}} \tag{2.16}$$

for any energy, where A_p is given by

$$A_p = \frac{1}{\rho d_p} \tag{2.17}$$

with atomic density ρ and periodical atomic distance d_p.

Case of ^{111}In in InP

The axial critical angle of an electron $(Z_1 = 1)$, originated from the ^{111}In electron conversion with maximum energy $E_{e\,max}$ and minimum energy $E_{e\,min}$

$$E_{e\,max} = 241,7keV$$
$$E_{e\,min} = 144,6keV$$

(energy values are calculated in the table 3.9), in the InP compound with atomic charges for indium $Z_{2-In} = 49$ and for phosphorus $Z_{2-P} = 15$ and so mean charge of $Z = 32$, is given by equation 2.12 and presented in the table 2.1

	$\Psi_{critical}$					
	E_{max}			E_{min}		
Orientation	In axis	P axis	Mixed	In axis	P axis	Mixed
$< 100 >$	1,8073	1,0000		2,3367	1,2929	
$< 110 >$	2,1493	1,1892		2,7789	1,5375	
$< 111 >$			1,5694			1,5694
$< 211 >$	1,6331	0,9036		2,1115	1,1682	

Table 2.1: The critical angle of an electron produced by electron conversion of ^{111}Cd in the InP compound, using the distance between atoms calculated in table 3.3 and equation 2.12

Channeling effect

The interactions outcome will differ for particles emitted in different directions:

- If the particle is emitted at an angle with a crystal axis lower than the critical angle the particle will channel in all components of the trajectory's direction perpendicular to the axis. This implies the confinement of the particle to the surroundings of the axis, resulting in a trajectory around the axis.
- If the particle is emitted with an angle with a crystal plane lower than the critical angle the trajectory will suffer channeling in the direction components perpendicular to the plane. Such effect results in the confinement of the particle to the plane's proximity, this means no change of the particle's trajectory in the directions parallel to the plane.
- If the particle is emitted with an angle above the critical angle, the potential will produce no channeling effect but a random reorientation of the trajectory.

The channeling and blocking effects cause a deviation from the otherwise isotropic distribution of charged particles. The emitted particles that leave the crystal are collected by a detector, and the deviation, due to these effects, creates an anisotropy of the distribution of the charged particles. This is preferentially observed along the principal axis within the critical angle.

Stopping power

The charged particles are continuously slowed down by the interactions with the nuclei and electrons of the crystal. The stopping power ε is a measure of the energy loss due to those interactions.

$$\varepsilon = \frac{1}{\rho}\left(\frac{dE}{dx}_{nuclei} + \frac{dE}{dx}_{electron}\right), \tag{2.18}$$

where ρ is the mass density and dx the space traveled.

Heavy charged particles interacting with matter

In emission channeling the α particles are the only heavy elements used as probes and only the scattering with electrons must be taken into account because other scattering would result in the dechanneling of the particles and effect is non-relativistic.

In the RBS studies also only the collisions with electrons of the material must be considered for the stopping power calculation, since harder encounters would result in the scattering of the ion and there is only interest in studying the interactions until a backscattering collision and back to the detector. There is also no need for a relativistic approach due to the big mass of the ions in comparison to its energy (about 2MeV). In these cases the Bethe-Bloch theory is applicable for high energy particles, when the electronic contribution is dominant[1]. Te Bethe's equation for the electronic energy loss in a target is:

$$\frac{dE}{dx}_{electron} = \frac{4\pi Z_1^2 Z_2 e^4}{mv^2}\rho_a L_0, \text{ where} \tag{2.19}$$

$$L_0 = \ln\left(\frac{2mv^2}{Ei}\right), \tag{2.20}$$

: Where ρ_a is the atomic density, Z_1 is the ion atomic number, m_e is the electron mass, Z_2 is the atomic number of the target atoms and Ei is the average excitation level of the electrons in the target atoms.

Electrons or positrons interacting with matter

If on the other hand, the charged particles are light (as electrons) their interactions with the nuclei will result in elastic scattering. This way only the interactions of the charged particle with the electrons are relevant for the stopping power and these are well described by the Bethe-Bloch theory for relativistic particles [1].

To compute the mean rate at which an electron loses energy by collision processes in passing through matter Bethe developed the mean stopping power formula:

$$\frac{dE}{dx}_{electrons} = \frac{2\pi\rho Z e^4}{mv^2}\left\{ln\left(\frac{(\gamma+1)E^2}{2E_i^2}\right) - \left(\frac{2}{\gamma} - \frac{1}{\gamma^2}\right)ln2 + \frac{1}{\gamma^2} + \frac{1}{8}\left(1-\frac{1}{\gamma}\right)^2\right\} \tag{2.21}$$

In the case of high energy ($E > keV$) electrons traveling in a solid, as in the case of study (which is in the order of $10^2 keV$), the energy loss due to collisions when passing through matter is given by the Beth mean stopping power formula [5].

This stopping power formula does not take into account the atomic binding energies,and so it is intended for energies greater than the binding energies ($E \gg eV$, in the case of study the binding energies are of the order of $5eV$ 3.1).

Lindhard's reciprocity principle

The simulation's aim is to calculate the rate of particles reaching the detector coming from inside a single crystal. The channeling effect is used to calculate the outcoming point and direction, and with this the trajectories that would reach the detector are selected. This method means the calculus of a total of 4π spherical angle trajectories build and only a small fraction of 0.1% (fig. 2.3) is in the direction of the detector.

Lindhard's reciprocity principle states that the trajectory of particles flowing in a crystal is invariant

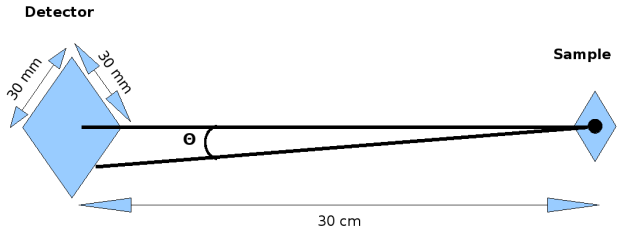

Figure 2.3: The setup geometry.

with respect to reversing the sense of direction, if one can neglect irreversible processes such as deceleration of particles caused by scattering at the electrons of the crystal (case of emitters located not to far from the surface). Theorem, which implies a correspondence between the channeling effects of a beam entering a single crystal and that of sources are inside the crystal. So if instead of simulating random trajectories originating at the emitter atom at the a beam of particles coming from the detector with the same energy is simulated to enter the crystal.

Heavy particles

Charged particles with masses higher/equal to the proton mass and energies above few keV can be described by the laws of classical mechanics. The quantum mechanical effects are reduced to interactions with nuclei and consequent large angular deflections neglected in the channeling effect. The effects of the particle's and crystal atom's electrons can be introduced as screening in the potential and as retarding forces. So the potential used is a sum of the Coulomb potentials from the lattice atom's nuclei screened because of the electrons.

Often the program used for the simulations is FLUX[13]. The program starts by the defining of the unit and reduced cells. The movement in the orientation (z) direction is neglected in the channeling effect, the particle goes too fast and sees "mean potentials" transverse to the travelling directions, so the track of the ion is defined by its position and momentum in the xy directions (x, y, p_x, p_y). The subcell is divided in a grid of bins, the program follows the track of the ion through successive grids, along the z direction. The deflections due to interactions with the subcell atoms are calculated with the ZBL-Potential. Each iteration (along z) the program saves the position of the ion in the subcell and, due to the symmetry of the crystal lattice, when the ion position falls off of the represented subcell the program substitutes the grid by the next one that corresponds to the one in the direction the ion falls on[1].

Light particles (e^-, e^+)

The energy involved in nuclear decay is typically of the order of keV up to MeV, that implies a relativistic approach for light particles. Additionally, if the "De Broglie" wavelength (relation of wave-particle duality[1]:

$$\lambda_\perp = \frac{h}{p_\perp} \tag{2.22}$$

is of the order of the potential, then the quantum effects are preponderant. In the electron case for $E \ll 10MeV$, that is the situation upon β^- decay and conversion electron emission, the motion is characterized by a relatively low number of bound states, which means it should be described using quantum-mechanics. In the case of positrons and high energetic electrons the number of bound states is much higher so it would be less important and it would be difficult, for the computational reasons, to use quantum-mechanics description.

Spin interactions, particle-host, are not relevant for most of the channeling effects, therefore the description of the quantum amplitude, that determines the relativistic wavefunction for a spinless particle, is given by the Klein-Gordon equation:

$$\left[\hbar^2 c^2 \Delta_{xyz} + \left(i\hbar\frac{\delta}{\delta t} - V(r)\right)^2 - m_0^2 c^2\right]\Psi'(r,t) = 0. \tag{2.23}$$

Since most of the time dependence of the motion is in the direction of z, the wave function time-dependent term can be given by a plane wave along-z,

$$\Psi(r,t) = e^{i\left(k_z z - \frac{E_e}{\hbar}t\right)}\xi(x,y,z) \tag{2.24}$$

where E_e is total energy

$$E_e = \hbar^2 k_z^2 c^2 + m_e^2 c^4. \tag{2.25}$$

Assuming that velocity is mainly in the direction z ($v_z \sim v$), apart from a $\frac{V^2}{2\gamma m_e c^2}$ term which can be considered a second order relativistic correction, a "schrödinger like" structure equation is obtained:

$$\begin{aligned} -\frac{\hbar^2}{2\gamma m_e}\Delta\xi - \frac{V^2}{2\gamma m_e c^2}\xi + V\xi = i\hbar v\frac{\delta}{\delta z}\xi \Rightarrow \\ -\frac{\hbar^2}{2\gamma m_e}\Delta\xi + V\xi \sim i\hbar v\frac{\delta}{\delta z}\xi. \end{aligned} \tag{2.26}$$

Using the continuum approximation of the potential, the potential V will be replaced by the mean potential in the perpendicular direction $U(x,y)$. Thus, by the "separation of variables" method, the equation is split into

$$\begin{cases} -\frac{\hbar^2}{2\gamma m_e}\Delta_{xy}\psi_1 + U\psi_1 = E_\perp\psi_1 \\ -\frac{\hbar^2}{2\gamma m_e}\Delta_z\psi_2 = i\hbar v\frac{\delta}{\delta z}\psi_2 \end{cases} \tag{2.27}$$

and the solution will be given by the product of the z-direction plane wave (the solution of the second equation) and the solution of the first equation :

$$\xi(x,y,z) = \psi_1(x,y)e^{-i\frac{E_\perp z}{\hbar v}}. \tag{2.28}$$

In the overall Klein-Gordon equation, the solution found is

$$\Psi(r,t) = \psi_1(x,y)e^{-i\frac{E_\perp z}{\hbar v}}e^{i\left(k_z z\frac{E_e}{\hbar}t\right)} \tag{2.29}$$

provided that the ψ_1 obeys to "transverse schrödinger" equation:

$$-\frac{\hbar^2}{2\gamma m_e}\Delta_{xy}\psi_1 + U\psi_1 = E_\perp\psi_1, \tag{2.30}$$

where γ is once again the Lorentz factor and so the γm_e is the relativistic mass. In order to use in the simulations the result must be solved numerically, so, and since the potential is periodical, it is expanded in Fourier series, in the reciprocal lattice vectors ($g_{nm} : g_{nm} = ng_1 + mg_2$):

$$\begin{cases} \psi_1^j(R) = e^{(ik_\perp \cdot R)} \sum_{nm} C_{nm}^j e^{(ig_{nm} \cdot R)} \\ U(x,y) = \sum_{nm} U_{nm} e^{(ig_{nm} \cdot R)} \end{cases} \quad \text{with} \quad U_{nm} = \frac{1}{A} \int_A U(R) e^{(ig_{nm} \cdot R)} d^2R, \tag{2.31}$$

and being A the area of the 2dimensional unit cell, acting as the normalization factor. Therefor the solution is a linear combination of the eigenfunctions [1]:

$$\psi(r,t) = e^{\left(ik_\perp \cdot R + k_z z - \frac{E_e}{\hbar} t\right)} \sum_j \alpha^j \sum_{nm} C_{nm}^j e^{(ig_{nm} \cdot R)} e^{\left(-\frac{E_\perp^j}{\hbar} \frac{z}{v}\right)}, \tag{2.32}$$

where α^j are coefficients determined by the boundary conditions that are defined by the application of Lindhard's theorem. According to the Bloch theorem that states that the wavefunction of a particle placed in a periodic potential is given by:

$$\psi_{nk}(r) = e^{ik.r} u_{nk}(r), \tag{2.33}$$

where the corresponding energy eigenvalue ϵ_n, with periodically of the reciprocal lattice vector g_{nm} is

$$\epsilon_n(k) = \epsilon_n(k + g_{nm}) \tag{2.34}$$

and k is the wavevector. Applying the "schrödinger transverse" equation, and through several mathematical procedures the Fourier expansion results in the matrix equation

$$\frac{\hbar(k_\perp + g_{nm})^2}{\gamma m_e} C_{nm}^j + \sum_{n'm'} C_{n'm'}^j U_{n-n',m-m'} = E_\perp C_{nm}^j, \tag{2.35}$$

where $k_\perp$ is the transverse Bloch wavevector and $E_\perp^j$ is the transverse energy eigenvalue. Limiting the n and m variables to enough terms to achieve the necessary precision, which is called the "many beam" approach. For instance, in electron emission channeling it typically is used with $10 < n \; or \; m < 40$, which gives an accuracy of electron flux of about 1%.

Interaction Potential

The potentials used to describe the interactions between electrons and the ions of the crystal are the Doyle-Turner potentials (calculated using first-principle Hartree-Fock methods), which consist of the sum of m (typically 4) Gaussian terms [1]:

$$V_{DT} = -16\pi^{\frac{5}{2}} e^2 a_0 \sum_{j=1}^{m} \frac{a_j}{b_j^{\frac{3}{2}}} e^{-4\pi^2 \frac{r^2}{b_j}}, \tag{2.36}$$

where the Doyle-Turner coefficients a_j and b_j are tabulated in table 3.4 and a_0 is the Bohr radius.

Afterwards one averages the potential in the z directions for the case of study, in this case InP, expands in Fourier series and describes the vibrations by 3D-Gaussian distributions with deviation u_1, assuming a simple Einstein model and isotropic symmetry. This way the potential used for a given R location, for N atom type J is:

$$U_{DT,th\ nm} = -\frac{2\pi e^2 a_0}{dA} \sum_{J=1}^{N} \sum_{j=1}^{4} a_{j,J} e^{-ig_{nm}\cdot R_j} e^{-\frac{1}{4} g_{nm}^2 \left(\frac{b_j}{4\pi^2} + 2u_{1,J}^2\right)}, \tag{2.37}$$

being the potential for InP $< 100 >$ as illustrated in the figure 2.4.

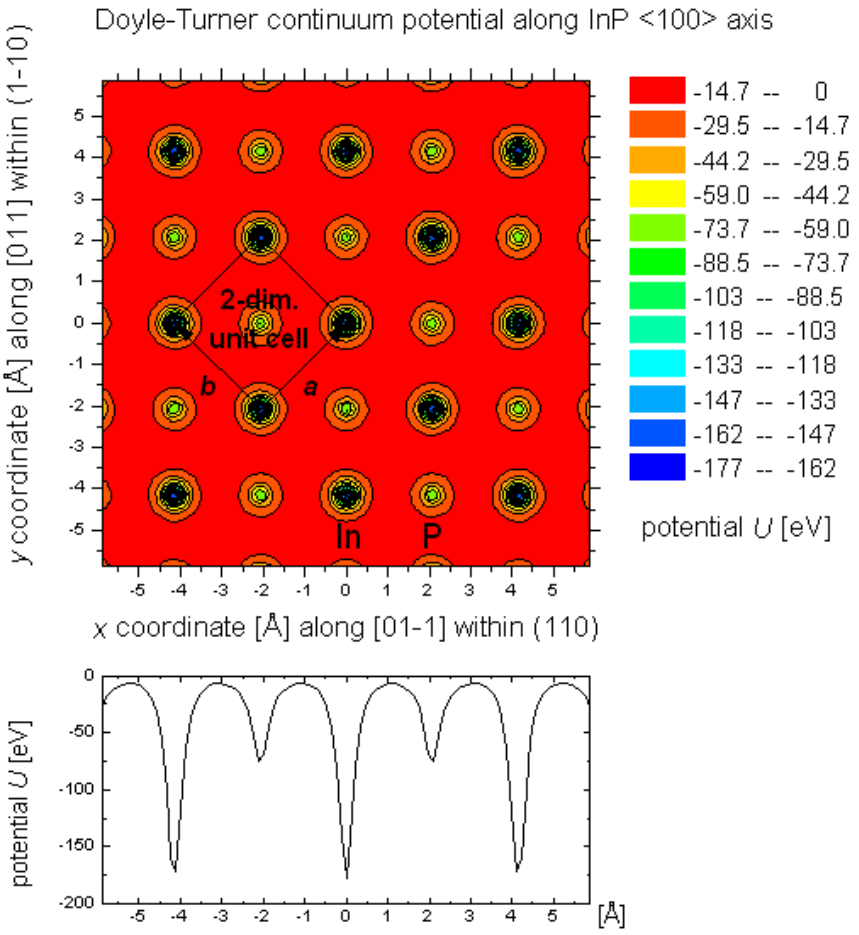

Figure 2.4: Two dimensional $< 100 >$ InP Doyle-Turner potential. The upper plot is a cut of the $[100]$ plane in a color code of the potential intensity in the direction $< 100 >$. The lower plot shows the potential as a function of the depth, in the crystal also in the direction $< 100 >$.

Implementation

Using a set of diagonalization routines, the eigenfunctions (represented by C^j_{nm}) and eigenvalues are calculated. Since the solution is as shown in eq. 2.32, the simulated boundary conditions are given by a particle entering the crystal (z=0) with the emission energy. At the surface of the crystal the wavefunction must match a planewave, i. e.:

$$\alpha^j = C^{j*}_{00}. \tag{2.38}$$

Dechanneling

The dechanneling is a process where electrons are scattered out of a channeling direction. It is hard to estimate and is the larger source of uncertainty of the technique analysis. There are two processes that contribute for dechanneling, i. e., scattering of electrons by electrons in the crystal and deviations of the potential from the ideal average continuum[1].

Since the e^- channeling is described by diffraction theory the dechanneling can be parametrized by the mean free path associated $\lambda_{dechanneling}$. The two processes are described by the mean free path associated, for scattering by the electrons (λ_{el}) and deviations of the potential (λ_{th}), so the dechanneling is given by:

$$\frac{1}{\lambda_{dechan}} = \frac{1}{\lambda_{el}} + \frac{1}{\lambda_{th}}. \tag{2.39}$$

The scattering of the flying electrons by electrons of the crystal is hard to quantify, since the amount of energy lost in each interaction varies strongly and the distribution of the energy loss is not straitforward calculated. In the case of electron channeling, this process is of higher importance since, the channeling is done along the rows and planes of the lattice atoms increasing the possibility of scattering by the atomic electrons.

Dechanneling due to interaction with the crystal electrons

There are three different models to calculate this kind of dechanneling. One considers total inelastic scattering according to Fernandez-Varea while the other two are based on the creation of plasmons theory [1]. On the first case, one considers that for each scattering a non-relativistic electron loses an amount of energy ΔE and by knowing the energy loss $\frac{dE}{dx}_{el}$, the total inelastic scattering mean free path can be calculated according to:

$$\frac{1}{\lambda_{el}} = -\frac{1}{\Delta E}\frac{dE}{dx}_{el} \tag{2.40}$$

where $\frac{dE}{dx}$ is the energy loss equation 2.21 when $\gamma \to 1$. The probability of low energy loss scattering is higher than the probability of high energy loss scattering. This results in the need to introduce in the ΔE factor, the distribution of energy loss per collision [1].

On the other cases, the plasmon creation model assumes that the energy lost of a relativistic electron collision is fixed as $\hbar\omega_p$, so the mean free path is:

$$\frac{1}{\lambda_{plasmon}} = -\frac{1}{\hbar\omega_p}\frac{dE}{dx}_{electron,electron\,plasma} \tag{2.41}$$

where $\frac{dE}{dx}_{electron,electron\,plasma}$ is the plasmon-related energy loss.

The deviations of the potential due to defects in the crystal are rather complicated to take into account. However the deviations due to the thermal vibration of the atoms can be more prominent than the scattering with electrons of the crystal and these are more simple to estimate.

Dechanneling due to the thermal vibrations of the crystal atoms

The thermal vibrations cause the crystal atoms' to deviate from their rest position, changing slightly the potential from the ideal average continuum potential that the electron feels during channeling. Since the deviations are small, this changes can be introduced in the potential using first order of the perturbation theory.

Having the solution to a simple system one adds a "perturbing" Hamiltonian to the solution, representing a weak disturbance to the system. Since the disturbance is small and the system has continuity, the various physical quantities associated with the perturbed system can be expressed as 'corrections' to those of the simple

system. This method can be used recursively until one finds the perturbed system as close as possible to the original complex system. In this case there is only need for a first order perturbation, so the potential deviation ΔU from the average continuum potential $U_{th}(R)$ is given by:

$$\Delta U = U(R - R_a) - U_{th}(R_a) \tag{2.42}$$

where $U(R)$ is the "unperturbed" potential, R is the ideal atomic position and R_a the displaced position due to thermal vibrations, which follows a three-dimensional Gaussian probability distribution.

The perturbed potential is then applied to a formula that represents the system. In this case the depletion of an eigenstate ψ^j, initially populated with P^j, per unit length z, is calculated using the variance of the perturbed potential U_{th}:

$$-\frac{dP^j}{dz} = P^j \frac{d}{(\hbar v)^2} \mid \langle \psi^j | U^2(R - R_a) - U_{th}^2(R) | \psi^j \rangle - \mid \langle \psi^j | U(R - R_a) - U_{th}(R) | \psi^j \rangle \mid^2 |_{th} \tag{2.43}$$

using Dirac notation, where $\langle \psi^j | B | \psi^j \rangle = \frac{1}{A} \int_A \psi^{j*} B \psi^j d^2R$ is the quantum mechanical expectation value of B, A is a normalization factor and $\mid \ldots \mid_{th}$ is the thermal averaging over two-dimensional Gaussian probability distribution.

Using the the Doyle-Turner potentials U_{DT} for U and the Bloch wave functions for ψ the second term $\mid \langle \psi^j | U(R - R_a) - U_{th}(R) | \psi^j \rangle \mid^2$ is small face the first one and represents the depletion without change of the state. Since the currently available computer power is limited, this term is neglected resulting in an overestimation of the dechanneling due to vibration of about 10%.

The Fourier representation of the eigenstate is inserted in the equation 2.43 (using the pq and nm indices), and using the fact that the Fourier transform of a Gaussian is a Gaussian the equation is simplified in the matricial form, using the "dechanneling matrix" F_{pqnm}, to[1]:

$$-\frac{dP^j}{dz} = \frac{P^j}{\lambda_{th,j}} \approx P^j \sum_{pq} \sum_{nm} C_{pq}^{j*} F_{pqnm} C_{nm}^j \Rightarrow \tag{2.44}$$

$$\frac{1}{\lambda_{th}^j} = \sum_{pq} \sum_{nm} C_{pq}^{j*} F_{pqnm} C_{nm}^j \tag{2.45}$$

which is solved using the boundary condition

$$P^j(z = 0) = C_{00}^j C_{00}^{j*}. \tag{2.46}$$

Simulation

The simulations are calculated in several steps:

- First the implantation depth profile must be simulated[1].
- Define the unit and reduced unit cells, each projected in 2D principal axis (which are measured during the experiments.
- The Fourier components of the interaction potential must be calculated.
- Each 2D pattern is simulated by considering discrete electron energies specific of each or by a set of multiple energies, weighted by the histogram shape of he β^- energy spectrum.

Fitting Procedure

Fitting is a long analysis process, for which we use a "home made" program called FDD. For each fit, in FDD, there are many steps:

1. Import pattern - Load the measurement's pattern to be fitted.

[1] Using SRIM program the implantation profile can be fairly estimated.

2. Calibrate - Use a file of calibration associated with the setup used for this experiment, which provides the correct angular range of the measurement, taking into account the distance of the detector from the sample.

3. Reduce pattern limits and skip bad channels- Since the detector is connected with the electronic weiring in the surroundings of its surface, the external pixels may give unreliable information, for this reason the pattern's exterior points are reduced and neglected in the fitting process. Besides there are some dead pixels in the detector, which can be removed from the fitting routine by setting their values to zero manually.

4. Normalize - Using the lower yield areas (relative to the directions in which the channeling effect didn't occur) of the pattern as background counts, the program does a first normalization. This normalization is refined after fitting, since the simulated patterns are normalized.

5. Import simulations library - For each crystal orientation the simulations of each lattice site and other parameters (such as r.m.s. displacements, resolution, and displacements of the lattice sites in the three directions $< 100 >$, $< 110 >$, $< 111 >$) are alltogether compiled in a library. This library has the theoretical data to fit with.

6. Choose one or a sequence of simulations to fit with - The fitting program was altered/improved during this project. In a EC lattice location study many direction's patterns are studied. For each direction the location of the probe in different lattice sites produces different patterns. There are many parameters optimized in the fitting process, such as the angular resolution σ, the root mean square displacement of the atoms u_1. On top of all that there is an infinity of locations where the original radioactive probe can be in the lattice, even though there is a discretization of the lattice site, this implies many simulations. Depending on the number of axe and on the precision intended the simulation library can contain up to 1000 simulations.

7. Find the best fit - After fitting all simulations and comparing the chi square of the fit χ^2, the lower value of χ^2 indicates the best fit, and so the simulation/group of simulations used and the fractions obtained for each, in the fit, reveal the most probable reality.

8. Save the best fit result and all important information about that fit (σ, χ^2, fraction, u_1, scale, lattice site), for analysis.

The fitting process includes:

- the optimization of the experimental pattern's orientation and centering, in relation to the simulation pattern. This process is essential but it is not extensive. Many times the orientation could be continuously changed until the pattern would be oriented in a totally different orientation and if the orientation is much deviated from the simulation's, than the fitting would give no realistic outcome.

- the optimization of the pattern's normalization, giving a scale value.

- the fitting of the pattern is done with two simultaneous patterns or more, the random pattern and one or more simulation patterns. The result is the chi square of the fit χ and the fractions used to optimize the fit, i. e., the fraction of each simulated pattern and the random pattern. A fit is as meaningfull as low the correlation factor is. The higher the fractions used the higher the percentage of probes are supposedly in the sites of the simulations.

The fitting program allows the user to fit up to 4 simultaneous patterns, including the random. In which case the fraction of a good fit ($\chi^2 < 5$) gives the proportion of lattice sites inhabitance of the probes.

Changes in the fitting program

There are many variables that are fitted during the fitting procedure, in a "fit loop" the experimental pattern's parameters (such as the orientation and the center) are optimized and in each iteration of the "fit loop", each "fit", the parameters involved in the match of the patterns ("fit") are optimized (such as the fraction of the random and simulated pattern and the experimental pattern's normalization). The "fit loop" stops when the χ^2 value stabilizes or the number of iterations reaches a certain value. After each fitting the program used to modify the experimental pattern's parameters, using them as initial input parameters for further "fit loop"s.

As a first approximation study of the experimental pattern all simulation patterns, of the simulation library, should be fitted. The best "candidates" are found, i. e., the simulation patterns that are most probable

to give a best fit. This is a rough general fitting, after which each "candidates" and the simulation patterns with small differences (fitting parameter variations) from the "candidates" are "re-fitted", with different initial parameters and higher number of "fits", in a refining process. It is then that the best "fit" is found.

In order to automate the first rough general fitting, in the course of this work, the program was altered to allow the user to request the fitting with a list of consecutive simulation patterns. The program now allows the user to select an initial and final simulation pattern, afterwards it runs the "fit loop" iteratively with all simulations, in the library list, within those selected. The simulation libraries are build so successive variations of one parameter are put in a roll. This way the user can proceed with the study of a parameter's variation, around a "candidate" simulation, automatically.

Further changes were applied to improve the reproducibility of the process. The change of the input parameters at the end of each "fit loop" is very usefull for two main reasons. First, if one wants to improve the fit results, by increasing the number of "fit"s in a "fit loop", this is equivalent to running the "fit loop" again, with the same simulation pattern (since the parameters were changed in the end of the first "fit loop"). Secondly, if the simulation pattern used in the "fit loop" gave good results, this will optimize the parameters for the fitting procedure, but if the fit gave a bad correlation value then the parameters found don't represent any improvement, in consecutive bad fits, or in the rough general fitting, this can result a faulty change of the parameters, for instance the disorientation of the pattern. This change of the parameters also reduces the reproducibility of the results, since the results are dependent on the sequence of "fit loop"s done before. In order to do the automatic fitting of a "list" of simulations, this was altered and at the end of each "fit loop" the pattern is "reseted" and a new feature was added so the user can choose the number of successive "fit loop"s the program does for each simulation (when using the automatic fitting of a list of simulations).

2.4 Rutherford Backscattering Spectrometry (RBS)

Rutherford Backscattering (RBS) is a technique used to determine the composition of a crystal as a function of depth. In the case of a single crystal Rutherford Backscattering channeling can also measure the crystallinity, the depth of surface disarrangement and the crystal defects as a function of depth.

To study the emission channeling effect of an element in a compound a highly pure and crystalline single crystal is required. This way the techniques of RBS and RBS-channeling are complementary and crucial to the EC technique, helping to characterizing a sample for its use.

In this work the ITN Van De Graaff accelerator facility provided the He^+ 2MeV probing beam. This mono-energetic beam was used to analyze the surface and crystallinity of one of our InP samples.

In order to get familiar with the technique and to test a sample used in other EC projects, RBS studies of a sample of InP implanted with ^{73}As was made, in the beginning of this work. Its analyses are included in this report in section 3.2 as an example of the procedure and of what we expect to obtain by studying a similar sample to be implanted with ^{111}In. A more detailed description of the experimental procedure is given in appendix B.

Elements distinction

Rutherford Backscattering results from the dispersion of the incoming particle by the nuclear charges of the atoms of the sample. The energy of the scattered ion/particle is dependent on the mass of the atom that scattered it and of the initial energy of the beam.

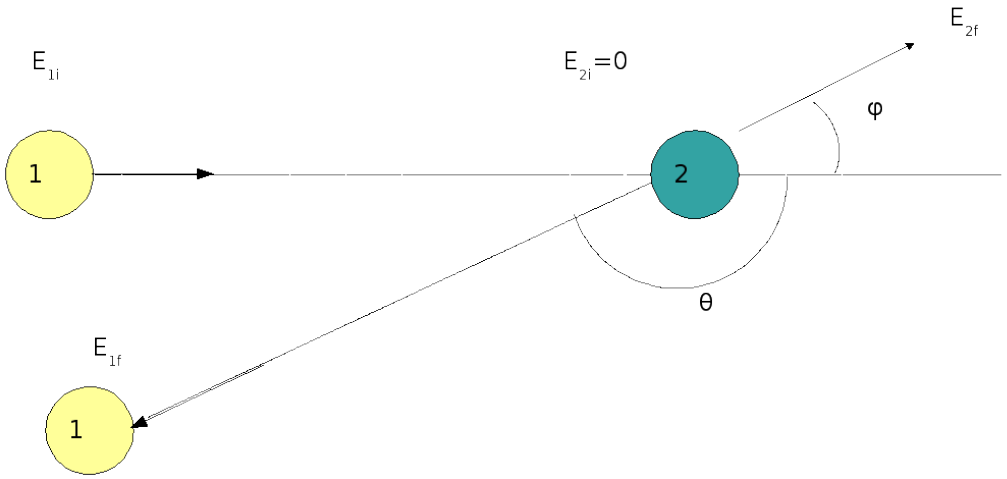

Figure 2.5: Classical Backscattering

Considering the invariance of energy and momentum in a classical 2 body interaction, as shown in figure 2.5, the final energy E_f of each scattered projectile is proportional to its initial energy E_i according to:

$$\begin{cases} E_f = E_i \\ p_f = p_i \end{cases} \Rightarrow E_{1f} = KE_{1i}$$

$$\begin{cases} E_{1i} + 0 = E_{1f} + E_{2f} \\ p_{1i} = p_{1f} + p_{2f} \end{cases} \Rightarrow \begin{cases} E_{1i} = E_{1f} + \frac{p_{2f}^2}{2m_2} \\ \begin{cases} p_{1i} = -p_{1f}\sin\theta + p_{2f}\cos\varphi \\ 0 = p_{1f}\cos\theta + p_{2f}\sin\varphi \end{cases} \end{cases} \Rightarrow \begin{cases} p_{2f} = \frac{p_{1f}\sin\theta + p_{1i}}{\sqrt{\frac{1-p_{1f}^2\cos^2\theta}{p_{2f}^2}}} \\ \sin\varphi = \frac{-p_{1f}\cos\theta}{p_{2f}} \end{cases}$$

The value of proportionality between the initial and final energies is the cinematic factor K, being m_j, $p_i j$, $p_f j$ the mass, initial and final momentum of the projectile/target atom $j = 1$ or $j = 2$:

$$
\begin{aligned}
p_{2f}^2\left(1-\frac{p_{1f}^2\cos^2\theta}{p_{2f}^2}\right) &= \left(p_{1f}\sin\theta+p_{1i}\right)^2 \Rightarrow \\
p_{2f}^2 &= p_{1f}^2\cos^2\theta+p_{1f}^2\sin^2\theta+p_{1i}^2+2p_{1i}p_{1f}\sin\theta \\
&= 2E_{1f}m_1+2E_{1i}m_1+4\sqrt{E_{1f}E_{1i}\cos\theta m_1} \Rightarrow \\
E_{1i} &= E_{1f}+\frac{2E_{1f}m_1+2E_{1i}m_1+4\sqrt{E_{1f}E_{1i}\cos\theta m_1}}{2m_2} \Rightarrow \\
E_{1i}\left(1-\frac{m_1}{m_2}\right)-E_{1f}\left(1+\frac{m_1}{m_2}\right) &= \frac{2m_1}{m_2}\sqrt{E_{1f}E_{1i}\cos\theta} \Rightarrow \\
\frac{E_{1f}}{E_{1i}} &= \frac{m_1\cos\theta+\sqrt{m_2^2-m_1^2\sin_2\theta}}{m_1+m_2} \Rightarrow \\
k &= \left(\frac{\sqrt{{M_2}^2-{M_1}^2 sen^2\theta}+M_1 cos\theta}{M_1+M_2}\right)^2
\end{aligned}
\tag{2.47}
$$

Cross Section

The probability of occurrence of a backscatter process is given by its cross section times the particle flux density. The probability of an event detection is given by the product of the event's probability, and times the the detection probability, given by the product of the detector solid angle times its efficiency.

The detection probability is characteristic of the detector and the setup symmetry:

$$
\begin{aligned}
\frac{d\sigma(\theta)}{d\Omega}d\Omega N_{atoms} &= \frac{scattered\ ions\ into\ d\Omega}{IncidentIons} \Rightarrow \\
\frac{d\sigma}{d\theta} &= \frac{-b}{\sin\theta}\frac{db}{d\theta}
\end{aligned}
\tag{2.48}
$$

Where b is the impact parameter.

Impact parameter without recoil

The simplest case considers an elastic collision. The minimum distance, r_{min}, reached by a charged particle of momentum p due to coulomb repulsion, is calculated by the conservation of angular momentum of that particle. This way the ion interaction with the crystal atom, is given by[8]:

$$
\vec{L}=\vec{r}\times\vec{p}\ since\ \vec{v}\equiv\vec{r}\times\vec{\omega}\ \Rightarrow m_1vb=m_1r^2\frac{d\phi}{dt} \tag{2.49}
$$

The impact parameter is the minimum distance component perpendicular to the ion's initial trajectory. The figure 2.6 is a schema of the interaction and the variables related.
Using the Coulomb potential

$$
V_1(r) = \frac{Z_2e^2}{r}dr: \tag{2.50}
$$

$$
\vec{F}_{1\,2} = \int\frac{Z_2e^2}{r}d\vec{r}=\frac{Z_1Z_2e^2}{r^2}\frac{\vec{r}}{r} \Rightarrow \tag{2.51}
$$

$$
\begin{cases}
\Delta p = 2p_i\sin\frac{\theta}{2} \\
F=\frac{Z_1Z_2e^2}{r^2}=\frac{dp}{dt} \Rightarrow
\end{cases}
$$

$$
\begin{aligned}
\Delta p &= \int F\cos\phi dt=\frac{Z_1Z_2e^2}{vb}(\sin\phi_f-\sin\phi_i)\Rightarrow\Delta p=\frac{Z_1Z_2e^2}{bv}2\cos\frac{\theta}{2} \Rightarrow \\
b &= \frac{Z_1Z_2e^2}{m_1v^2}\cot\frac{\theta}{2}
\end{aligned}
\tag{2.52}
$$

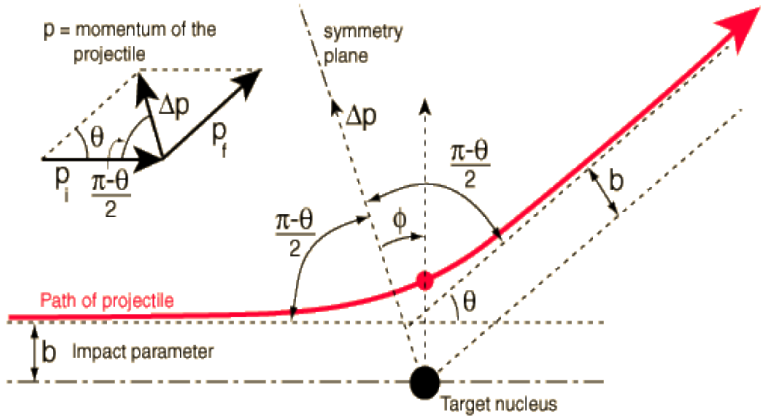

Figure 2.6: Impact parameter of a repulsion interaction. (This figure was reconstructed [36])

The cross section becomes:

$$d\sigma(\theta) = \left(\frac{Z_1 Z_2 e^2}{4E}\right)^2 \frac{1}{\sin^4 \frac{\theta}{2}}. \tag{2.53}$$

Impact parameter with recoil

When the ion collides with a crystal atom, due to the large ion's mass and high energy before interaction, the crystal atom can recoil. For this calculation the angular momentum of both, ion and atom, is considered to be conserved. This implies using a reduced mass[8],

$$\mu = \frac{m_1 m_2}{m_1 + m_2}, \tag{2.54}$$

instead of the ion mass, and a reduced angle θ_c correspondent to the one-body problem with reduced mass, instead of the angle of scattering θ

$$\tan\theta = \frac{\sin\theta_c}{\cos\theta_c + \frac{m_1}{m_2}}, \tag{2.55}$$

as shown in figure 2.7. The impact parameter is consequently given by :

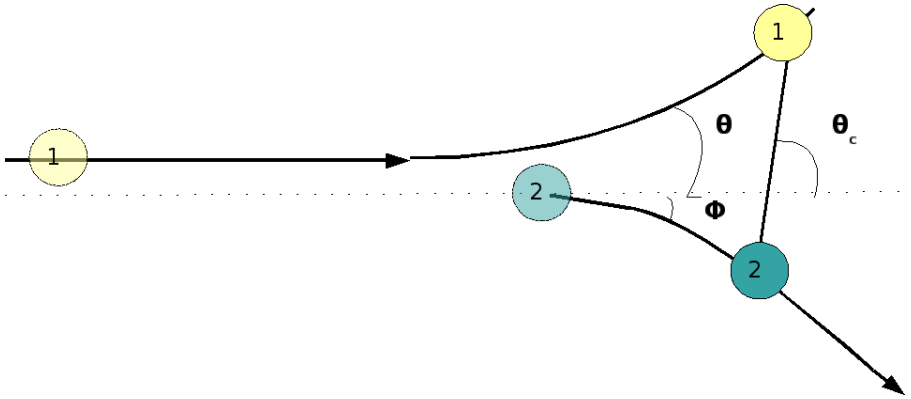

Figure 2.7: Impact parameter with recoil.

$$b = \mu r^2 \frac{d\phi_c}{dt} \tag{2.56}$$

This makes the cross section:

$$\sigma(\theta) = \left(\frac{Z_1 Z_2 e^2}{4E_{1i}}\right)^2 \frac{1}{\sin^4\theta} \frac{K^2\left(m_1+m_2\right)^2}{m_2\sqrt{m_2^2 - m_1^2\sin^2\theta}}. \tag{2.57}$$

Depth profile

The trajectory of the ions inside the crystal includes coulomb interactions with the crystal's electrons that contribute to the slowing down of the ions, continuously, while traveling in and out until the ions leave the crystal.

The energy of a backscattered ion depends on the mass of the element with which the ion collided, as it was explained before. The difference between the energy value calculated for a collision with an element and the energy of the measured ion is created by the slowing process. This allows the determination of the scattering collision depth.

As in channeling the stopping power, ε defined in section 2.3, is:

$$\varepsilon \equiv \frac{1}{\rho}\frac{dE}{dx}, \tag{2.58}$$

where ρ is the matter's density, E is the energy and x the depth of the ion.

In the case of RBS, the heavy ions are not relativistic, so the depth sensitivity is calculated then as:

$$\begin{aligned} \Delta E &= \rho\varepsilon\Delta x \Rightarrow & (2.59)\\ &= \rho_a Na M\varepsilon\Delta x \Rightarrow & \\ \Delta x &= \frac{\Delta E}{\varepsilon\rho_a M Na} & (2.60) \end{aligned}$$

Where Na is the Avogadro number, ρ_a is the atomic density and M is the atomic mass of the sample. In the case of compounds (AB) the stopping power is a pondered sum:

$$\varepsilon_{AB} = \frac{n_A}{n_{A+B}}\varepsilon_A + \frac{n_A}{n_{A+B}}\varepsilon_B, \tag{2.61}$$

where n_A/n_B is the number of atoms of the element A/B in a sample of n_{A+B} atoms. Using known elements of the sample's composition, the energy corresponding to backscattering by a certain element is calculated and two of such calculated values are used to calibrate the RBS spectrum in energies. The energies corresponding to a certain element are assigned to perform a spectrum calibration, in depth.

Crystallinity

When the Rutherford Backscattering technique is used to study a single crystal, the measure of backscattering yield is a function of the orientation of the crystal axis regarding the detectors due to the channeling effect.

The crystallinity is a measure of the relation between the mean yield, obtained by measuring the backscattering yields of several random orientations and the axis oriented yield, obtained when the crystal is oriented along a principal axis of the crystal. A crystal that has many structural defects will provide less channeling effect to the beam ions. Thus this physical variable translates a measure of the structural quality of the crystal.

Surface peak

The surface peak is an evidence of the dechanneling caused by the atoms of the surface, which are 100% exposed to the beam without the channeling effect and any structural disarrangement in the surface region. When a sample is grown, then cut and chemically treated or polished the surface boundaries often accumulate defects. This damage layer is measured by RBS, since it does not participate in the channeling effect and it is characterized by a larger yield of backscattered ions in preferential orientations. This raise of the yield at the beginning of the energy spectrum is called surface peek.

Counting the number of multichannel channels of the surface peek and using the energy calibration, the use of the stopping power formulas, allows the estimation of the damaged surface defect and density of defects.

3 Experimental

3.1 Indium phosphide (InP)

Choice of the material

The present study of emission channeling with ^{111}In in InP is the first case to use the setup with the cryogenic station installed. This study aims also a test of the equipment and finding its limits, looking forward to improving the cooling concepts [12].

InP has a low binding energy and a large atomic charge number (Z). The low binding energy implies a relatively low Debye temperature and so a relevant temperature dependence of the lattice vibrations. The large atomic charge number implies a dramatic channeling potential change with atomic vibration or structure defects, hence providing more sensitivity to the atomic displacement for the EC technique. Both of these characteristics are expected to be significant for the dechanneling effect, upon temperature variations.

Besides the physical properties, which are of main interest for this work, there are many utilities for the indium phosphide compound (InP). InP is a binary III-V semiconductor that has superior electron velocity comparing to the semiconductors silicon and gallium arsenide compound meaning why is used in high-power and high-frequency electronics.

Indium phosphide also has a direct bandgap, which means that the minimal-energy state of the conduction band and the maximal-energy state of the valence band are in the same crystal momentum (k-vector). This makes InP useful for optoelectronics devices like laser diodes. Also used as a substrate for epitaxial indium gallium arsenide based opto-electronic devices. Indium phosphide also has one of the longest-lived optical phonons of any compound with the zincblende crystal structure.

Indium phosphide parameters

The choice of InP had to do with many of its physical properties, but also with the fact that the study was planned to focus on an element of the crystal, and so the choices were reduced to single-crystals with elements ISOLDE could provide (in more detail on section 3.3) and for which an isotope suitable for emission channeling exists both of which represents a significant limitation.

Basic Parameters at 300 K	
Crystal structure	Zinc Blende
Group of symmetry	Td2-F43m
Number of atoms in $1cm^3$	3.96×10^{22}
Heat of formation	5.89 eV = 560 kJ/mol[17]
Debye temperature	425 K
Density	4.81 g/cm3
Dielectric constant (static)	12.5
Dielectric constant (high frequency)	9.61
Effective electron mass	0.08mo
Electron affinity	4.38 eV
Lattice constant	5.8687 $\mathring{A}$
Optical phonon energy	0.043 eV

Table 3.1: Basic Parameters at 300 K [44]

Thermal properties	
Bulk modulus	7.1·1011 dyn cm-2
Melting point	1335K [4]
Specific heat	0.31 J g-1 °C-1
Thermal conductivity	0.68 W cm-1 °C-1
Thermal diffusivity	0.372 cm2 s-1
Thermal expansion, linear	4.60·10-6 °C-1
Melting point	Tm = 1333 K
For $0 < P < 40$ kbar	Tm = 1333 - 2.0·P (P in kbar)

Table 3.2: Thermal properties [45]

crystal structure

The first-neighbor distance in all four bonds of a zinc-blend structured compound is calculated as [30]

$$d(In-P) = \frac{\sqrt{3}}{4} d_0, \tag{3.1}$$

where d_0 is the lattice constant which is the same in the three directions. The crystal lattice constants give the norm of the primitive translation vectors $< 100 >$, $< 010 >$ and $< 001 >$, which are in this case all of the same size. The zinc blend structure can be seen as the merge of two face-centered cubic structures, one for each element or the same in the case of diamond, with the same lattice constant but deviated by the first-neighbor distance, in this case $d(In-P)$, with an angle between the bonds of $\theta = 109.5^o$.

The distance between atoms in the different directions is calculated from the ratio of the vector's norm and the number of atoms that the vector goes through. In crystals with this structure in the $< 100 >$ direction there are two principal axis per unit cell which are parallel, i.e. there is one along atoms of each element. Considering the coordinates system as in figure 3.1, there is one atom in the origin and in the end of the primitive translation vector, which are shared with the next and previous vectors ($< 200 >$ and $< -100 >$), giving a distance between atoms $d_{<100>}$ of one atom in the distance of d_0.

$$d_{<100>} = d_0 \tag{3.2}$$

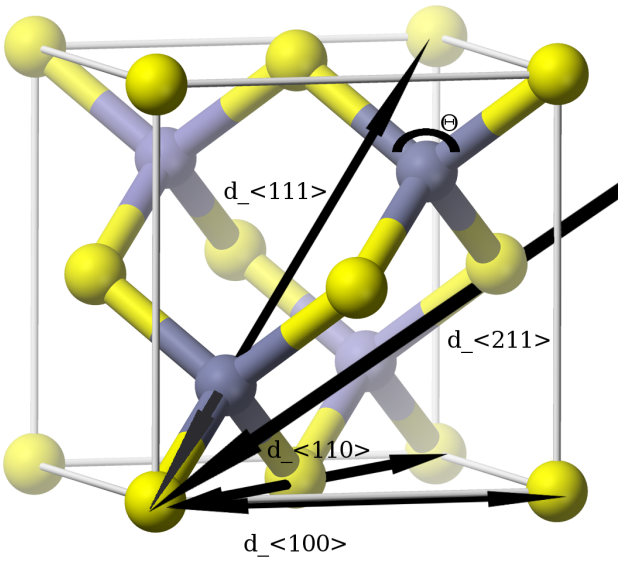

Figure 3.1: The InP compound unit cell[42], where the In atoms are represented, not in scale, by the yellow spheres and the P atoms by the grey spheres.

The $< 110 >$ direction also has two principal axis, each along atoms of one element, can be decomposed in two primitive translation vectors $< 100 >$ and $< 010 >$ and its vector passes through one atom in the origin, one in the end of the vector and the face-center atom, the first two are shared but not the face-center one, giving a total of two atoms. So the norm $\| < 110 > \|$ is calculated according to 3.3 and the distance between atoms is given by 3.4.

$$\| < 110 > \| = \sqrt{\| < 100 > \|^2 + \| < 010 > \|^2} \Rightarrow \tag{3.3}$$

$$d_{<110>} = \frac{\sqrt{2}d_0}{2} \tag{3.4}$$

In the $< 111 >$ direction both elements are aligned in the same principal axis, however the vector passes through one atom in the origin, one at the end of the vector and one of the other element at $\frac{1}{3}$ or $\frac{2}{3}$ of the vector. So the distance is calculated as the ratio between the vector's norm $\| < 111 > \|$ and the number of atoms:

$$\| < 111 > \| = \sqrt{\| < 100 > \|^2 + \| < 010 > \|^2 + \| < 001 > \|^2} \Rightarrow \tag{3.5}$$

$$d_{<111>} = \frac{\sqrt{3}d_0}{2} \tag{3.6}$$

In the $< 211 >$ direction there are again two parallel principal axis, each with atoms of one element, there is an atom at the origin of the vector, one at the centered-face in the plane $[100]$ and another in the end of the vector. The distance is given by:

$$\| < 211 > \| = \sqrt{\| < 200 > \|^2 + \| < 010 > \|^2 + \| < 001 > \|^2} \Rightarrow \tag{3.7}$$

$$d_{<211>} = \frac{\sqrt{6}d_0}{2} \tag{3.8}$$

The coefficients used on the Doyle-Turner potentials are in the table 3.4

distance between atoms		
Orientation	d	($\mathring{A}$)
$< 100 >$	$d_{In-In} = d_{P-P}$	5,8687
$< 110 >$	$d_{In-In} = d_{P-P}$	4,1498
$< 111 >$	$\overline{d_{In-P}} = \frac{1}{2} d_{In-In}$	5,0824
$< 211 >$	$d_{In-In} = d_{P-P}$	7,1877

Table 3.3: The distance between atoms at room temperature. Where $\overline{d_{In-P}}$ is the mean distance between an In atom and a P atom.

Doyle-Turner Coefficients for electron $f_{el}(s)$										
z	element	$a_1(\dot{A})$	$b_1(\dot{A}^2)$	$a_2(\dot{A})$	$b_2(\dot{A}^2)$	$a_3(\dot{A})$	$b_3(\dot{A}^2)$	$a_4(\dot{A})$	$b_4(\dot{A}^2)$	E
15	P	1.8882	44.8756	2.4685	13.5383	0.8046	2.6424	0.3204	0.3608	0.0617
49	In	3.1528	66.6492	3.5565	14.4454	2.8180	2.9758	0.8842	0.3345	0.1025

Table 3.4: Doyle-Turner Coefficients by [29]

Properties of the compound as function of temperature

The lattice constant measurements found in the literature are shown in the plots of the figure 3.2.

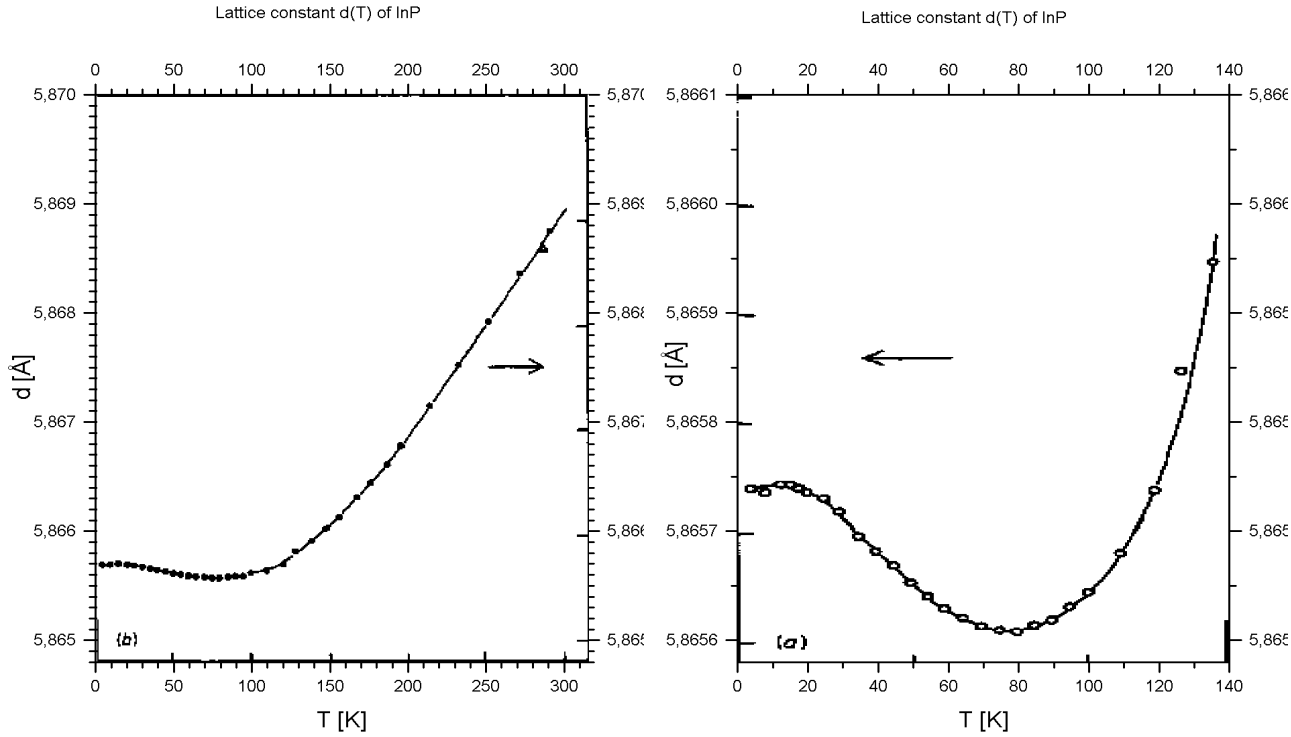

(a) lattice constant

(b) zoom in low temperatures

Figure 3.2: The lattice constant as function of temperature. [40]

Lattice constant	
T (K)	a ($\mathring{A}$)
51	5.86565
100	5.86565
150	5.86607
200	5,86688
293	5,86878

Table 3.5: Values for the lattice constant, taken from the plots 3.2a and 3.2b for the experimental temperatures used in this work.

Debye temperature

The figures 3.3a and 3.3b show the Debye temperature variations as a function of temperature for several III-V semiconductors.

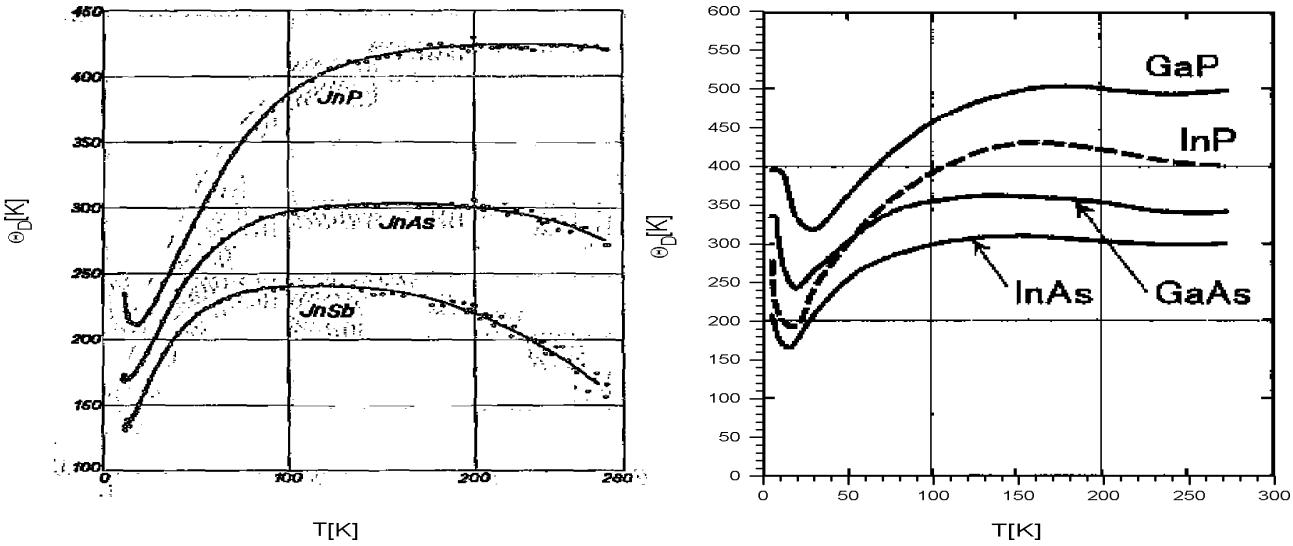

(a) Debye temperatures by [19]

(b) Debye temperatures by [18]

Figure 3.3: The Debye temperatures were calculated by measured heat capacity (C_v).

Root mean square displacement

The root mean square displacement (r.m.s.) characterizes the vibration amplitude or the displacement from the ideal sites on a crystalline lattice. If the thermal vibration is the main responsible, for r.m.s. then it is used to estimate the values from the Debye temperature accordingly with [16]:

$$u_1^2 =< x^2 >= \frac{3\hbar^2}{4Mk_B\Theta_D}\left\{1+4\left(\frac{T}{\Theta_D}\right)^2\int_0^{\frac{\Theta_D}{T}}\frac{x}{e^x-1}\,dx\right\}, \tag{3.9}$$

where M is the mass of the crystal's atoms, k_B is the Boltzmann constant and Θ_D is the Debye temperature. In order to calculate the vibration of an impurity sitting at a substitutional lattice site, one applies an effective Debye temperature (Θ'_D):

$$\Theta'_D = \sqrt{\frac{M}{M'}}\Theta_D, \tag{3.10}$$

where M' is the mass of the impurity.

These values, plotted in figure 3.4 were obtained or calculated with the eq. 3.10, using many sources of

the literature. It is easy to see that there are many discrepancies. The values used in this work were based on rms displacement measurements at room temperature and extrapolation down to 50K.

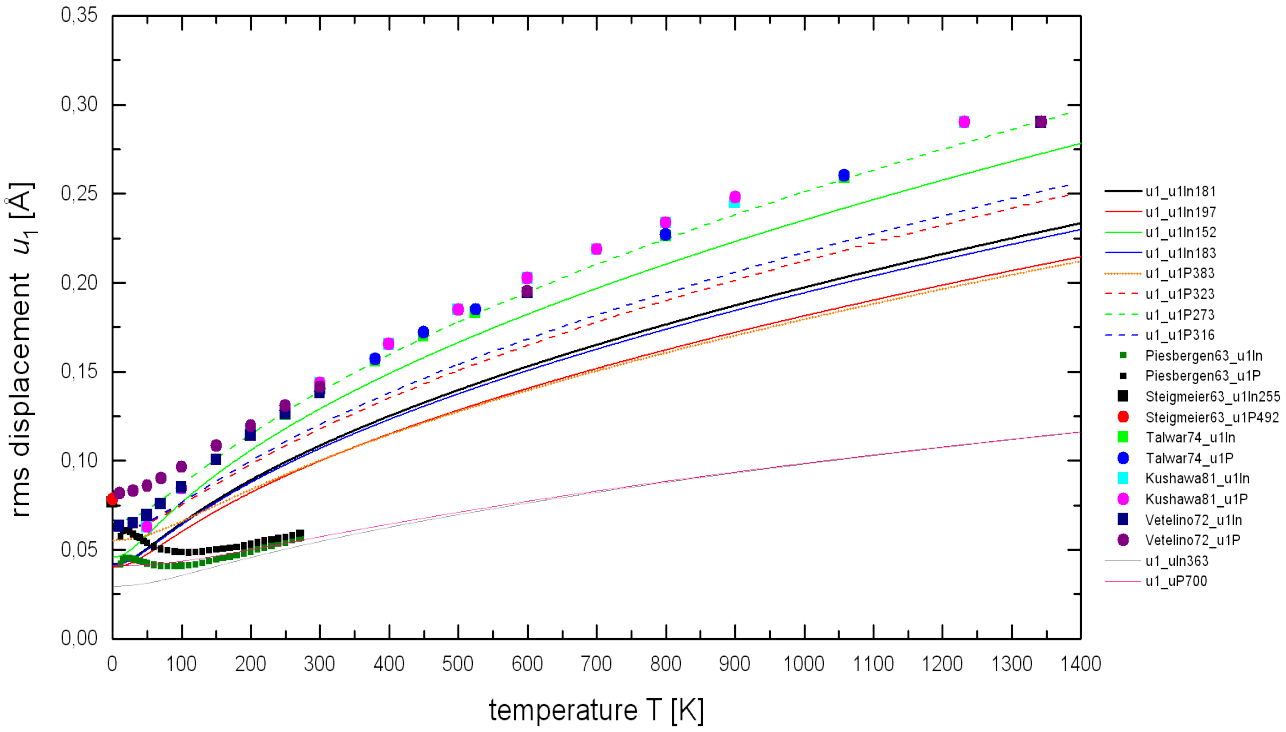

(a) Plot of the alltogether data on r.m.s. collected from the literature

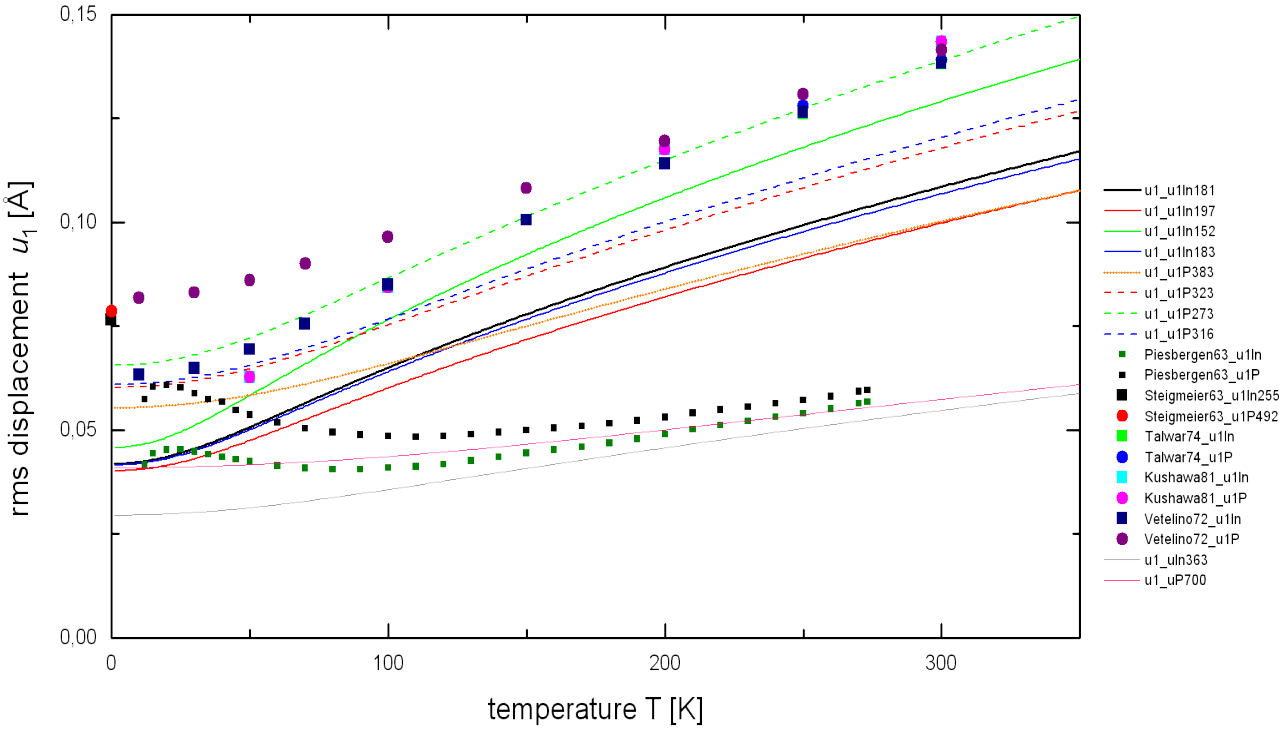

(b) Zoom of the plot for low temperatures

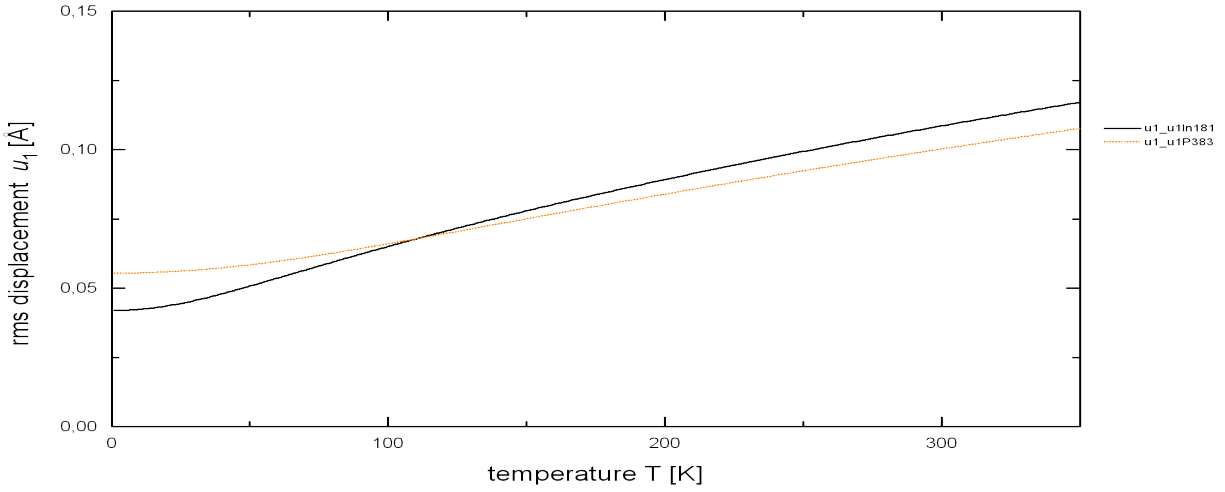

(c) The values used in this work

Figure 3.4: R.m.s. displacement as function of temperature, using the r.m.s. displacement and Debey temperatures collected from the literature, all data is in the annex A. The grey and pink dash lines are extrapolated values from the theoretical upper limit of the Debye temperature given by [24] and [23]. The other dashed lines are the phosphorus and the full lines are the indium, values extrapolated from the room temperature measurements. The dots represent the simulated (Talwar_74 by [22], Kushawa_81 by [21], Vetelino_72 by [20]) and the calorimetric (Piesbergen_63 by [19]) values.

3.2 Sample characterization

RBS channeling experiments were done on InP sample for the characterization of the surface and the crystalline quality. For a different EC study, the localization of ^{73}As in the InP lattice sites, the RBS channeling technique was use to study a 20 year old sample. This study was done in the beginning of this work, it was also useful to get to know the technique, but above all it gave a notion of the minimum purity and crystallinity to expect from a sample of this compound.

Van De Graaff accelerator

At ITN a He or H radio-frequency ion source is used to create positive ions He^+ or H^+, which are subsequently accelerated by a Van de Graaff accelerator up to 2.5MeV towards the standard RBS chamber. The accelerator, shown in figure 3.5, mainly consists of:

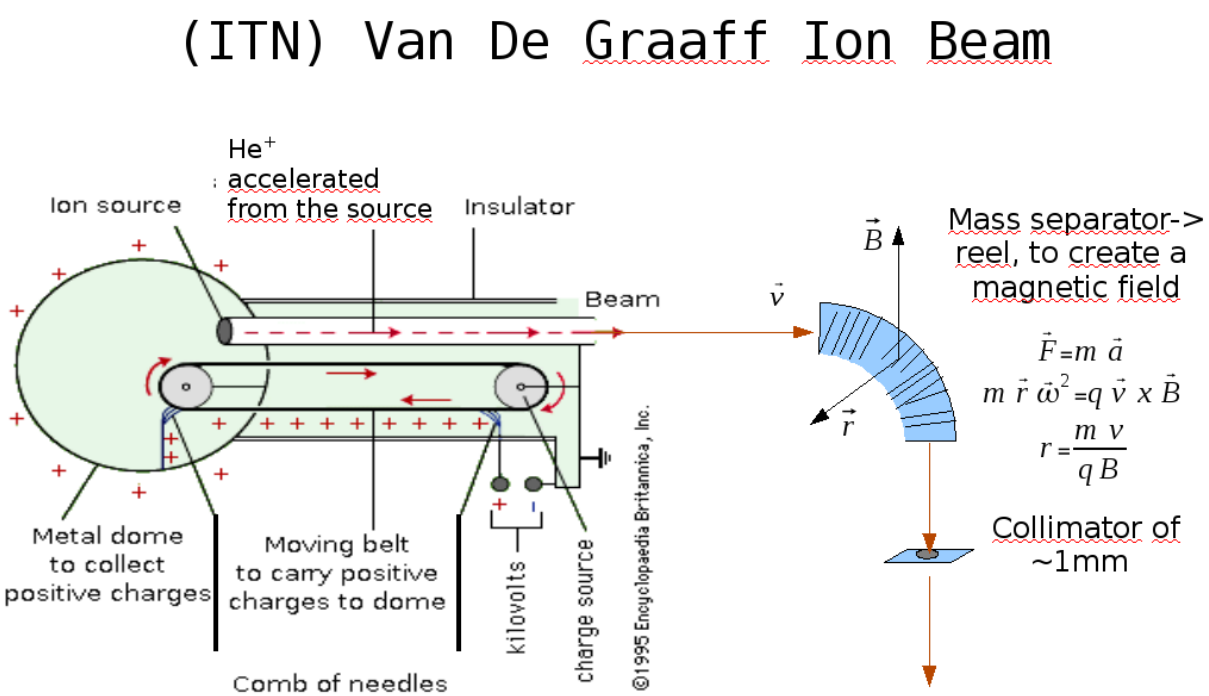

Figure 3.5: Van De Graaff ion beam (figure based on [37])

- a rubber belt, or a similar flexible insulator material.
- two metallic cylinders, used to roll the rubber belt.
- a large hollow metal sphere, the dome. Its surface is used as the charge container.
- two electrode combs of needles, of sharp metal points, used to connect with the rubber belt. They are positioned:

  the first near the exit cylinder and connected to a high positive potential;

  and the second inside the metal sphere to which it is connected.
- gas of high dielectric constant fills the Van der graaf, used to improve the isolation of the high voltage.

The Van der Graaff is an electrostatic accelerator changing mechanical work, of the belt, for potential energy, accumulated in the dome. The first comb is connected to a high-voltage (HV) source inducing high electrical fields in the tips of its needles. As a source of electrons, by field emission, the comb or the belt, depending on if the HV source is negative or positive, generates a corona discharge in the gas of the chamber [7](in ITN's case SF6), which has high dielectric strength in order to inhibit the spark formation, i. e., avoid discharges between the comb and the insulator container. The charged particles are then attracted by the first metallic cylinder and spayed onto or captured from the belt's surface, respectively for negative or positive HV-sources, since the belt is located on their way, between the comb and the cylinder. In the case of ITN the HV source is positively charged, so the comb will collect electrons from the belt's surface. The rubber belt then rotates over the cylinders carrying the charged particles against the potential gradient, to the dome. The dome behaves as a Faraday cage- hence any charges on the conducting dome accumulate outside canceling the field on the interior-, so the charges on the belt feel no opposing fields from the dome, only the fields created by them selves and so the charges are repelled from the belt flowing through the second comb to the dome.

As the belt continuesly moves, a constant current travels on the belt, to the inside surface of the sphere accumulating a high concentration of charges. The metal dome's charge grows until the rate of incoming charges equals the charge lost through leakage and through the corona discharges. The metal sphere and the exiting extremity of the Van der Graaff can this way maintain a very high potential difference, used to accelerate the ions to the order of the MeV.

After accelerating the He or H ions, into a mono-energetic beam of high energy, the ions are separated, in mass charge ratio, by a magnet and collimated to a 1mm beamspot on the sample.

RBS channeling study of an InP sample

Assembly

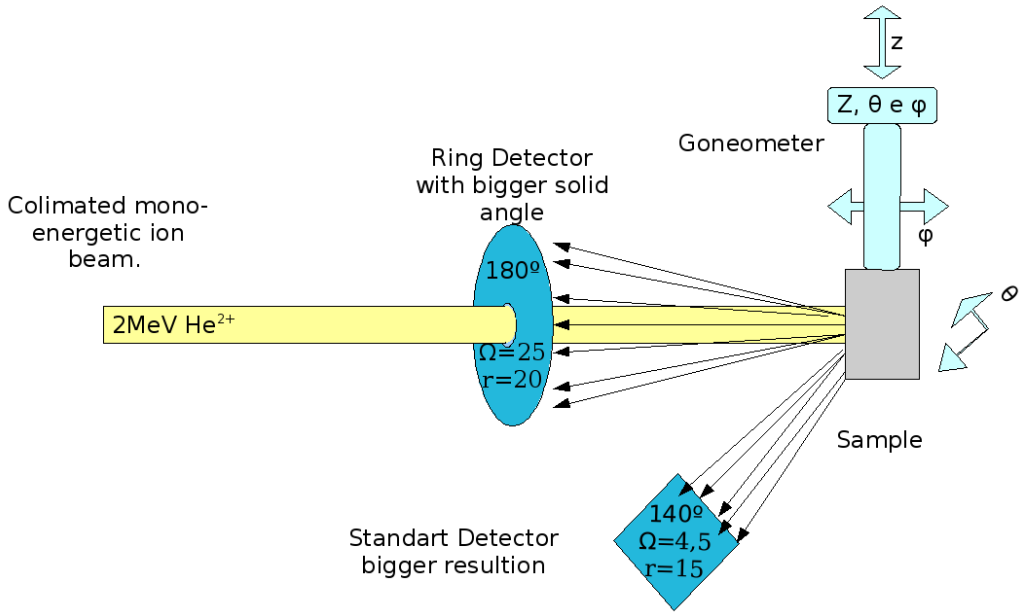

Figure 3.6: Backscattering experiment schema

- Beam:- 2Mev, He^+ collimated to 1mm spot.
- z, ϕ, φ Goniometer:- hardware controller for angular and height precision manipulation of the sample.
- Detectors:

  Standard (2)– high resolution detector, and smaller solid angle.

Ring (1)– lower resolution, larger solid angle, good for data analysis test. Has the form of a ring, through which the He^+ beam passes to hit the sample.

Detector	θ (^{o})	Ω (rad)	resolution (keV)
standard	140	4.5	15
ring	180	25	20

Table 3.6: The detectors characteristics. θ is the angle between the detector's normal and the beam, Ω is the solid angle.

- Vacuum:- usual vacuum primary and turbo pomp, plus valves.
- Schema:- Figure 3.6
- Conditions:

  Temperature:- room temperature

  Vacuum:- high vacuum
- Nomenclature:

  θ- is the polar angle of the sample with the beam.

  ϕ- is the azimuthal angle.

Orientation of the crystal

The first step in RBS channeling technique is to find the polar (θ) and azimuthal (ϕ) orientation of the sample which corresponds to the beam being aligned with its principle axis. In order to find the principal axis, it is necessary to find two principle planes. A principle axis will be in the crossing of the two principle planes. The yield of RBS is measured varying a specific angle, let it be ϕ for instance. After finding the angular value in which the yield has a minimum, due to the channeling effect, the process is repeated in a slightly different θ. This way the plane is defined by the two minimums.

Once found two minimums, one uses a plot like 3.7a to find the angles θ and ϕ in which the principal plane can be found. These values are then corrected by measuring the yield of RBS in their surroundings.

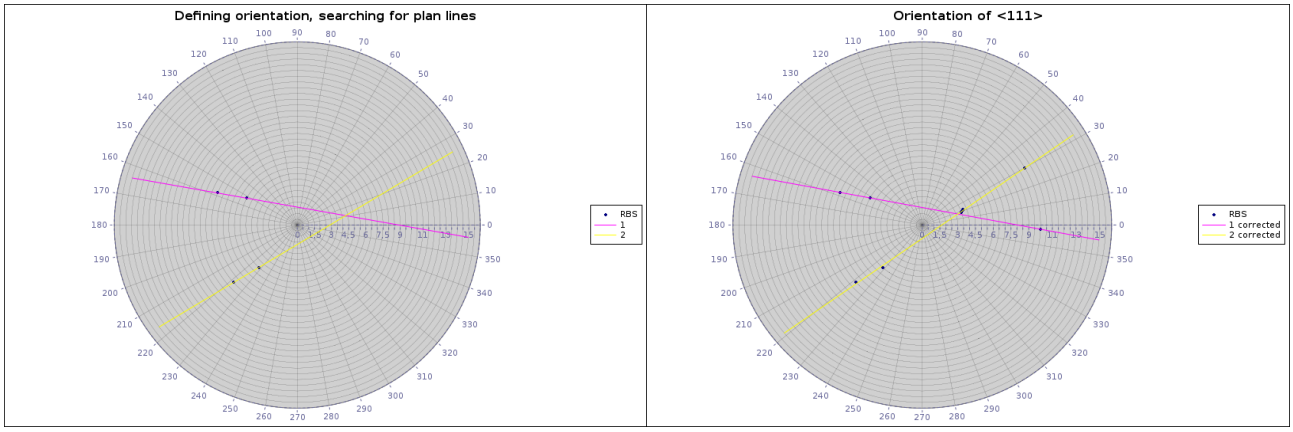

(a) Plot of the $< 111 >$ orientation

(b) Plot of the $< 100 >$ orientation

Figure 3.7: Stereographic projection of θ and ϕ (in degrees) used to search for the planes, to orient the sample. The θ angle is plotted as the radial distance to the center and the ϕ angle is plotted as the angle done between the point radial line and horizontal. Both angles are plot in degrees.

The number of planes and their azimuthal angles of interception are characteristics for the different principal axis ($< 100 >, < 110 > or < 111 >$) and can be used to identify the orientation of the crystal surface, if this should be unknown (usually it is specified by the manufacturer).

Spectrum

The RBS stoichiometric study of a sample is done in a random orientation, so the channeling effect is put a side. In order to do this in the crystals, and specially in single crystals, the RBS energy spectrum is gathered integrating various random orientations, averaging to reduce the channeling effect.

The RBS channeling yield is done by measuring the energy spectrum in a principal axis orientation and comparing it with the random, as one can see in the figure 3.8 two detectors are measuring since . One can also compare the difference between the spectra gathered by the two detectors in that figure.

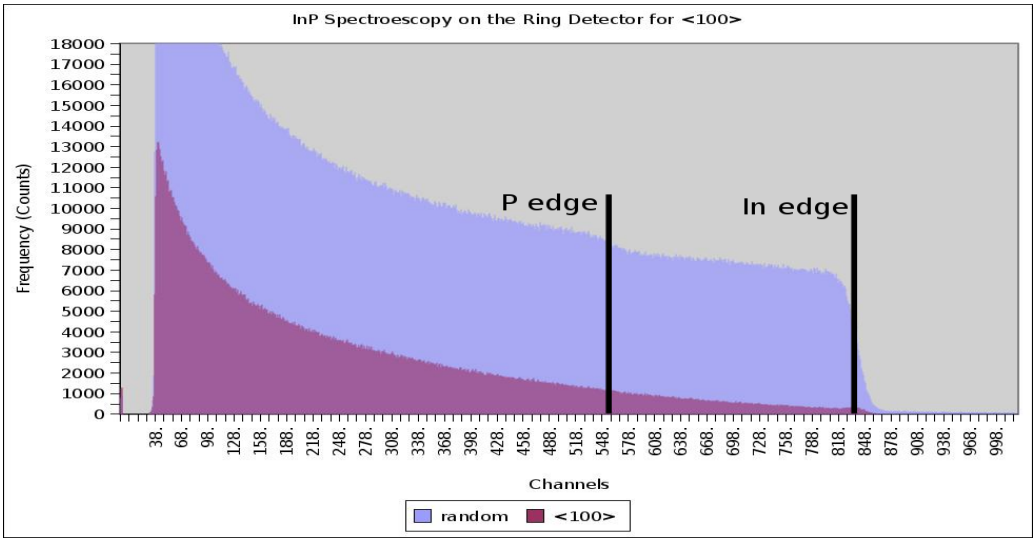

(a) Ring detector

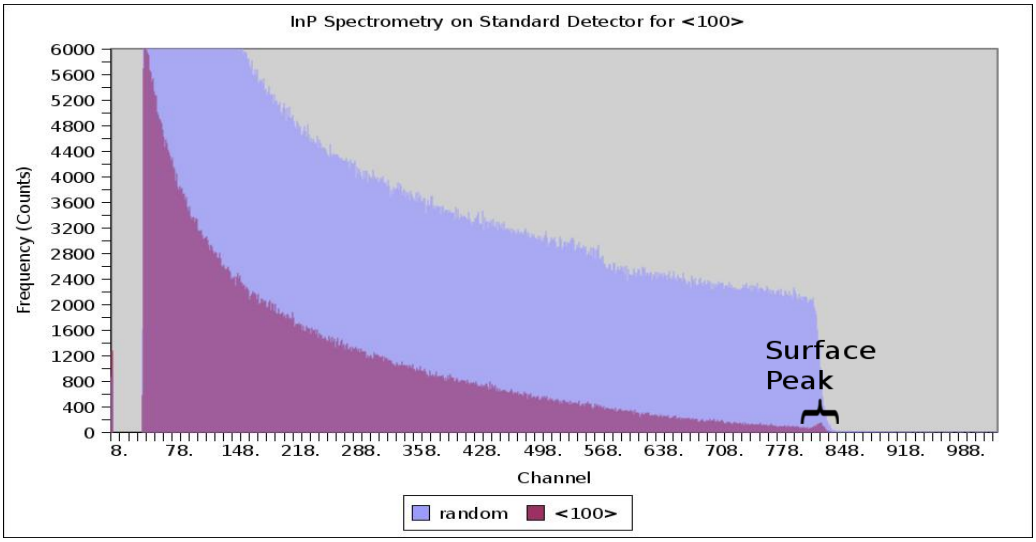

(b) Standard detector

Figure 3.8: The spectrum of $< 100 >$ orientation

Conclusions

The sample has a surface peak of roughly $80\mathring{A}$, a crystallization quality, or ratio of random and oriented yield in the first 50 channels after the surface peak, of $\chi_{min} = 5\%$, purity and proportion between compounds very good. Although only heavier substances than In could be undoubtedly visible, the comparison of the simulations and the results imply that the sample's purity is high.

3.3 ^{111}In

Choice of isotope

ISOLDE

ISOLDE, the On-Line Isotope Mass Separator, is dedicated to the production of high-energy radioactive ion beams, for many different experiments and applications. For many ISOLDE users it is essential, or greatly preferred for the beam to be delivered with a high degree of chemical purity, and thus, the separation between nuclei with different proton number Z but same number of mass (isobars) is required.

The CERN booster accelerator is used to create a beam of protons up to 1.4GeV, for many experiments, one of each is ISOLDE (another is LHC).

The target must be chosen so that it will produce the element of interest with a cross-section favorable and the least contamination of other isotopes if possible. There are four main steps in the ion beam creation [9][10]:

- A target is bombarded by the high-energy protons, from the booster, breaking some of the target's nuclei in a spallation (a large number of nucleons are emitted as a result of the hit of a high-energy particle), fragmentation or fission process.
- The produced atoms must be released out off the target. The ISOLDE method uses thick targets to enhance the isotope production, so to extract the nuclei of interest the target is heated to create a vapor-pressure of the radioactive elements to the temperature at which the element of interest are released by diffusion, desorption at the target's surface or by a chemical process, e. g. by introduction of a strong reactant element like fluorine that will form molecules with the radioactive element of interest, which are then easily ionized and extracted to the users. The atoms released are transferred by a tube. Controlling the tube's temperature, the tube's absorption and condensation, this becomes chemically selective (allowing to reduce the losses of the element of interest and enlarging the losses of another).
- In order to deliver and accelerate the elements of interest these must be ionized.The methods of ionization are complex and determines the beam contamination ratio and efficiency, for a specific isotope:

  Surface Ion Sources - An atom of low work function can be ionized by contact with a surface of high work function, provided the surface is hot enough to thermally release the ions. It uses the simplest set-up, a metal tube which has a higher work function than the atom that should be ionized heated up to 2400^oC, but it is of high efficiency and selectivity in the creation of Group I element beams. a number of other elements of low work function, in particular In, can also be ionized that way, W and Ta surfaces are commonly used.

  Plasma Ion Sources - The plasma is produced by accelerating electrons from a heated cathode into a low pressure gas mixture (typical Ar and Xe) with an anode, keeping the electrons in a voltage of about 130 V. This method is used to ionize elements that cannot be surface-ionized. To create noble gas isotopes' beams, continuous water flow are made to cool the transfer line in order to suppress the transport of less volatile elements.

  RILIS - The RILIS creates ions inside a hot cavity surface ion source, it uses the atomic physics technique step-wise resonance photo-ionization. By exploiting the unique electronic structure of different atomic species it is an efficient and highly Z selective ionization process.
- The ions are accelerated, separated by mass and charge ratio, collimated and directed to one of the beam line ends, where the appropriated setup is mounted for a specific experiment.

By using different target materials, different mass ranges are obtained. Each experiment applies for a beam time for the target that is most convenient. In the beginning of the year an agenda is created.

In the table of elements (3.9) those elements of which radioactive nuclei have been produced as ion beams at ISOLDE are marked yellow. In the ISOLDE Yield Database [11] the beam intensities for isotopes of these elements are listed. For isotopes where no new yields are listed yet from the PSB (PS Booster with 1.0 or 1.4 GeV protons), one can get an idea from looking at the available SC yields (0.6 GeV protons).

http://isolde.web.cern.ch/ISOLDE/

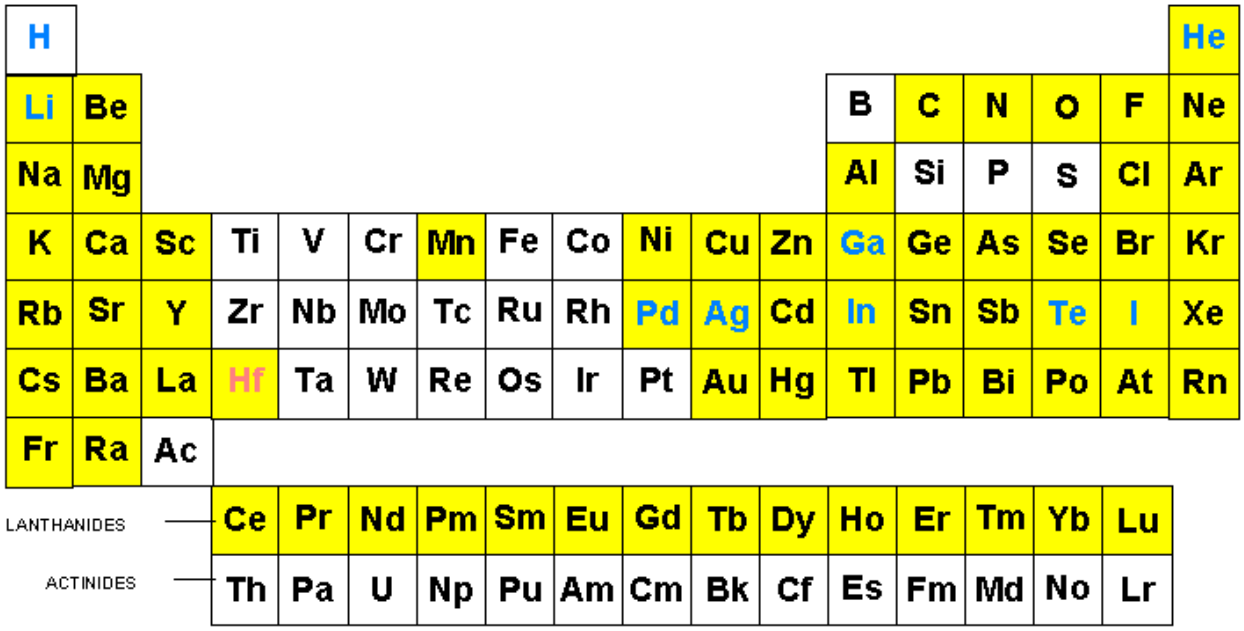

Figure 3.9: The elements available in the ISOLDE facility [38] - only beams from the elements with yellow background are available. The letters printed in blue mark that mainly neutron rich isotopes are produced, while red stands for neutron deficient ones.

Variety of In isotopes

Possible decay modes are chosen either β^- or electron conversion. Since the β^- decay implies a three body interaction the electron's energy varies with the energy of the neutrino, and so the spectrum of energies is continuum, which is more cumbersome for analysis. The electron conversion, due to the discreet energy spectrum, is a easier decay mode for analyses.

On top of that, the energy of decay had to be higher than the $\sim 20keV$ detection limit and if possible lower thanthe detector's saturation energy (about 200-250 keV).

Furthermore the decay could not be too fast for schedule reasons, nor to slow because the time window we had for the experiment was of the order of two weeks. There were two possible choices of isotopes, the $^{111}In(2.8d) \rightarrow {}^{111}Cd(C.E.)$ and $^{114}In(49.5d) \rightarrow \beta^- \rightarrow {}^{114}Sn$, see figure 3.10. Both were implanted but only the ^{111}In's study is presented in this work.

Another ^{111}In and the ^{114}In samples were used for emission channeling lattice location study at room temperature as function of the annealing temperature (see annealing description in section 3.4) and they are still in process of analysis. The objective of those experiments is to study the defect reduction as a function of the annealing temperature. The differences expected between the two isotope's study are due to the different decay energies and life times, since both should occupy substitutional sites of In.

Properties of the isotope

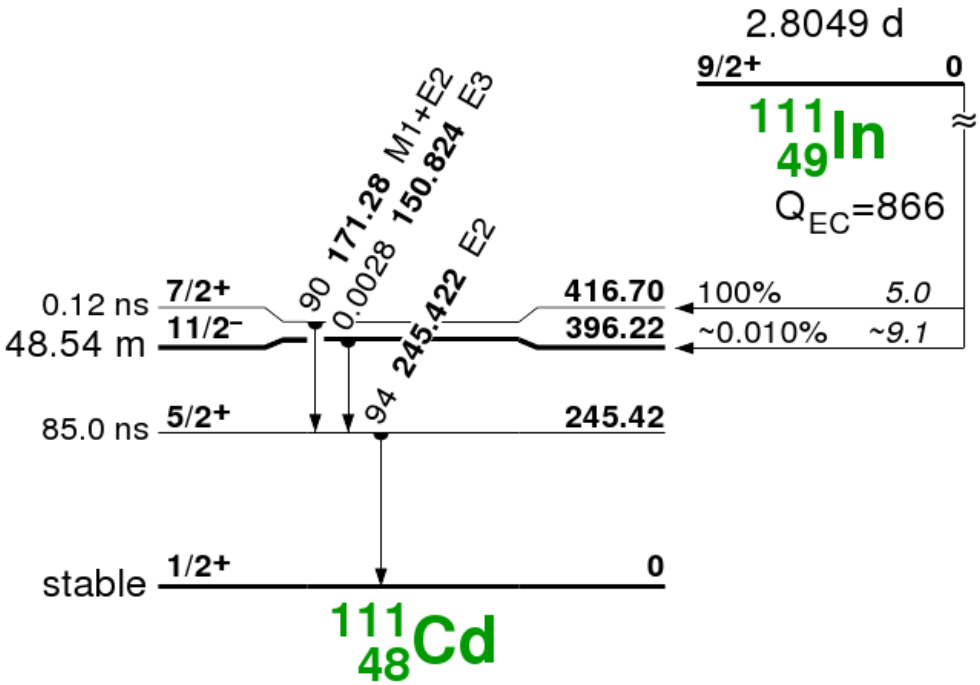

(a) ^{111}In decay

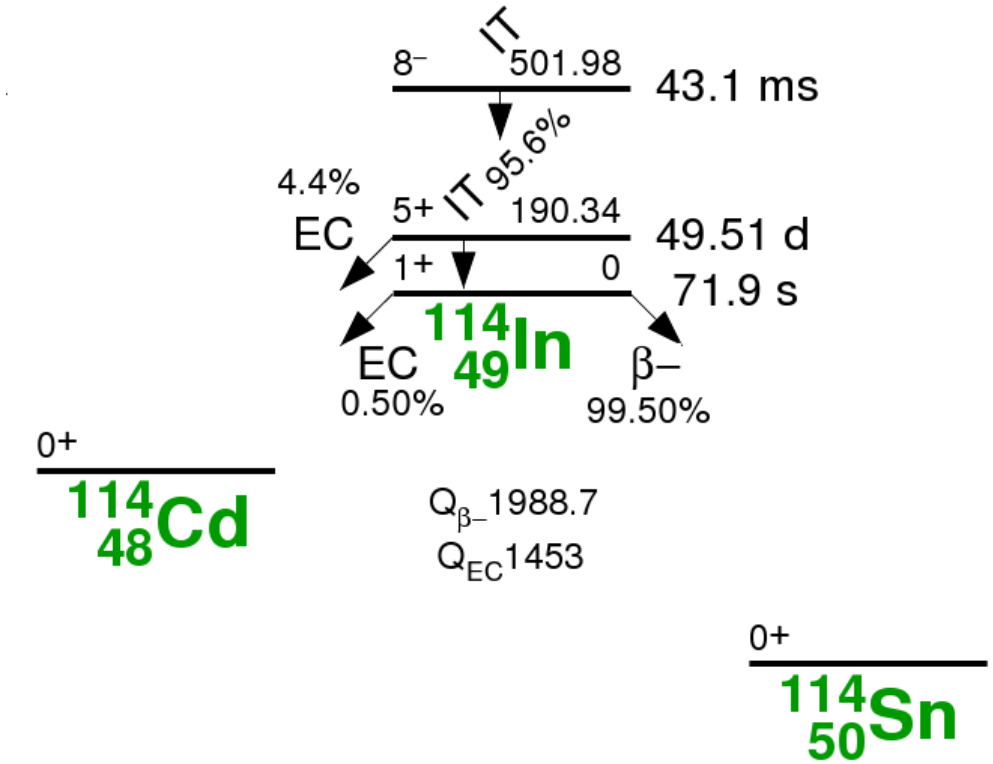

(b) ^{114}In decay

Figure 3.10: The ^{111}In decay to ^{111}Cd and the ^{114}In decay to ^{114}Cd and ^{114}Sn[39]

Energies

The ^{111}In isotope decays by electron capture. Then what is detected are the electrons emitted upon internal decay of excited states on the ^{111}Cd isotope to the ground state. γ decay competes with electron conversion at the closest shells (K and L), which energies are given by

$$E_{CE} = E_\gamma - B_{e'}, \tag{3.11}$$

where E_γ is the gamma transition energy and $B_{e'}$ is the electron atomic binding energy. The E_γ values are shown in table 3.7, the B_e- energies are tabulated in 3.8 (for other elements consult D.1) and the calculated E_{CE} in table 3.9.

$^{111}_{48}Cd\ \gamma s$ (2.8047 d 5)	
E γ (keV)	I_γ (%)
150.824 ± 0.013	0.0028
171.28 ± 0.03	90
245.395 ± 0.02	94

Table 3.7: Energy of the $^{111}_{48}Cd\ \gamma s$ [43], where I_γ is the intensity per 100 decays.

Cd atomic binding energies			
K	L1	L2	L3
26.7112	4.0180	3.7270	3.5375

Table 3.8: Cd electron binding energies of K and L shells. - taken from the in appendix table D.1

$^{111}_{48}Cd$ conversion electron			
$E_\gamma(keV)$	e shell	$E_{CE}(keV)$	I_{CE} (%)
171.28	K	144.568	8
171.28	L1	167.262	1
171.28	L2	167.553	1
245.40	K	218.689	5
245.40	L1	241.382	1
245.40	L2	241.673	1

Table 3.9: $^{111}_{48}Cd$ conversion electron energies, calculated from the tables 3.7 and 3.8. The CE intensity per 100 decays (I_{CE}) was taken from [39].

When using the ^{111}In decay, the emission channeling technique is in fact measuring the electrons emitted by $^{111}_{48}Cd$, but this information can be used to determine the lattice location of the parent isotope, $^{111}_{49}In$, because in decaying the nuclei of Cd gets such a low recoil energy, lower than the crystal structure binding energy for a vacancy to be created (heat of formation).

Considering the atomic mass $M_{^{111}In} = 1.03307444 \times 10^8 keV/c^2$ of the ^{111}In neutral isotope and $M_{^{111}Cd} = 1.03306579 \times 10^8 keV/c^2$ as the mass of the ^{111}Cd neutral isotope [43]. Still since in this case the indium decays by electron conversion, the atom has a hole in the K shell. The q-value of the electron capture $p + e^- \rightarrow n + \nu$, $Q_{^{111}In \rightarrow ^{111}Cd}$ is given by:

$$\begin{aligned} Q_{^{111}In \rightarrow ^{111}Cd} &= M_{^{111}_{49}In_{62}}c^2 - M_{^{111}_{48}Cd_{63}}c^2 \\ &= E_\gamma + E_\nu + B_{K\,^{111}_{48}Cd_{63}} \\ &= 859.4keV, \end{aligned} \tag{3.12}$$

where c is the speed of light and $B_{K\,^{111}_{48}Cd_{63}}$ is the binding energy of the K shell electron of the ^{111}Cd isotope, which is captured. Although in the literature [39] the value given for Q_{EC} is of $866keV$.

This implies that the recoil energy on ^{111}Cd, due to the decay, is:

$$\begin{cases} Q_{^{111}In\rightarrow^{111}Cd} = E_{^{111}Cd} + E_\nu + E_\gamma + B_{K\,^{111}_{48}Cd_{63}} \\ P_{^{111}Cd} = P_\nu = P \text{ (in the center of mass reference frame)} \end{cases} \Rightarrow \tag{3.13}$$

considering the neutrino has no mass

$$\begin{cases} E_{^{111}_{48}Cd} = \frac{P^2}{2M_{^{111}Cd}} \\ Q_{^{111}In\rightarrow^{111}Cd} = \frac{P^2}{2M_{^{111}Cd}} + Pc + E_\gamma + B_{K\,^{111}_{48}Cd_{63}} \end{cases} \Rightarrow$$

$$P = 1.41\times10^{-6}keV/c \Rightarrow E_{^{111}_{48}Cd} = 8.64\times10^{-4}keV \tag{3.14}$$

where the $Q_{^{111}In\rightarrow^{111}Cd}$ used is the tabelated, E_γ is the energy of decay of the ^{111}Cd to its ground state, which is mainly in the first decay of 171.28 keV and after of 245.42keV (as one can see from the fig. 3.10a) summing up to 416.7keV. Since the recoil energy $E_{^{111}_{48}Cd} = 0.864eV$ is significantly smaller than the binding energies of the compound $B_{InP} = 5.81eV$ from table 3.1, it is assumed that the ^{111}Cd will occupy the same lattice site as the parent isotope (^{111}In).

In the case of ^{114}In the β particles, emitted upon decay, are directly detected. The β^- are emitted in a continuous spectrum of energies, since its a two particles decay involving an electron and a neutrino. This can be of some disadvantage for experimental reasons of the setup, since its halflife is much bigger and it can't be implanted in too high doses to avoid the increase of defect creation with amorphisation of the InP lattice, the ^{111}In is preferred for this study.

3.4 Emission channeling setup

EC on-line chamber

The experimental chamber is installed on-line with the ISOLDE-CERN ion beam, In particular this setup is dedicated to the study of short life time isotopes ($T_{\frac{1}{2}} < 6h$) due to the fact that this chamber has both the implantation and detection blocks installed. Thus the detection can start just following implantation, avoiding the decay losses during sample transfer. The EC on-line setup is composed of the following parts [12]:

- Beam line - At ISOLDE each experiment has its setup and so there are beam lines that end in a valve, to which one can mount one's setup.
- Chamber - Main structure to which all blocks of the setup are mounted. Has many entrances and a center cavity in which sits the goniometer that holds the sample. The chamber contains several devices to help aligning and setting up the beam (3.11b):

  Collimators - there are two collimators, the first one collimates the beam before entering the main chamber and the second one ($\varnothing 1mm$) is located in the main chamber close to the sample holder.

  laser alignment block- a laser device with 3 movements (z, rotation and tilt) is used to align the collimators, thermal shield, sample holder and Faraday cup along the same optical beam axis of the chamber. The laser device is mounted in the first collimator chamber.

  Faraday cup - a copper cup is used as a Faraday cup, consisting of a trap for charged particles to measure the current of the beam and calculate the rate of implanted ions. The movable Faraday cup is inserted in the chamber from a side flange and positioned behind the goniometer sample holder. It can be active only when the goniometer has been moved to its uppermost position.
- Goniometer - Controls the position and orientation of a sample. It is mounted in a special flange on the chamber top and reaches the center of the chamber with an arm with the sample holder at the end. The goniometer has an annealing block installed that provides a controlled (by an external controller) heating of its sample holder.
- Vacuum circuit- Consists of a primary plus a turbo pump connected to the bottom flange of the chamber. All the chamber flanges are CF equipped with copper or flat viton O-rings, for easy operation of the most usually opened flanges.
- Detector - The detector block (detector chamber, xy solid state detector and shutoff valve) is mounted in a flange at 17 degrees with the beam line. A second spare detector flange at 30 is available on the left side of the chamber.
- Cooling station - The cooling station is a closed cycle He refrigerator, adapted to the chamber. In order to control the temperature of the sample, the goniometer heater resistance was used to heat the sample holder while the He refrigerator is working to set different temperature values from room temperature down to 50K. This method is precise, calibrated and reproducible.

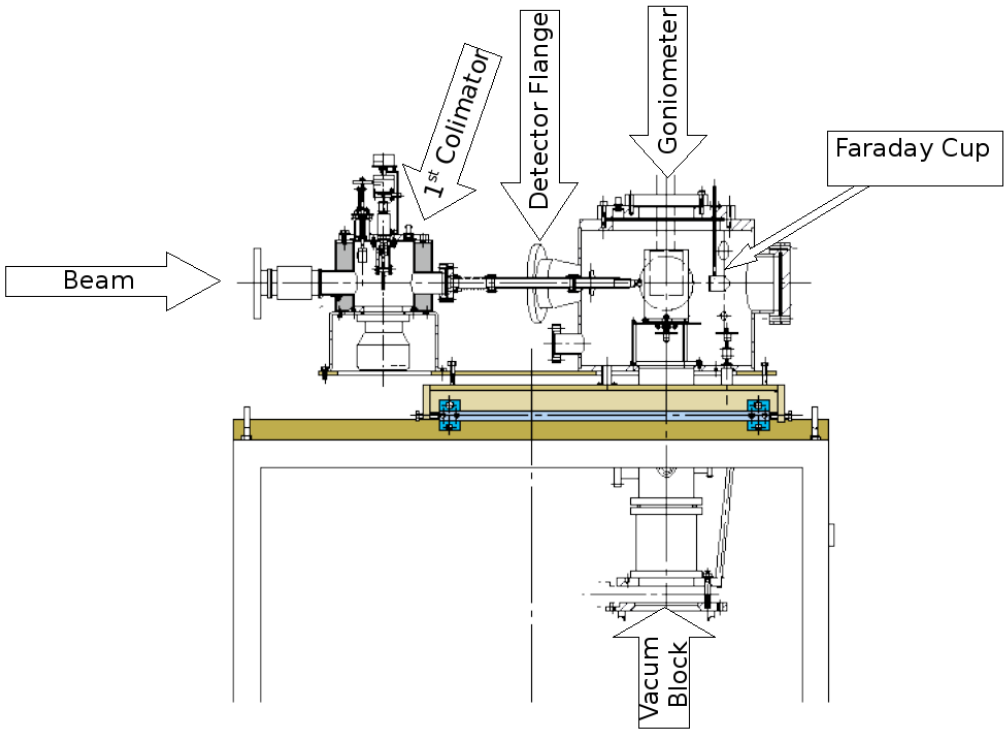

(a) Chamber schema

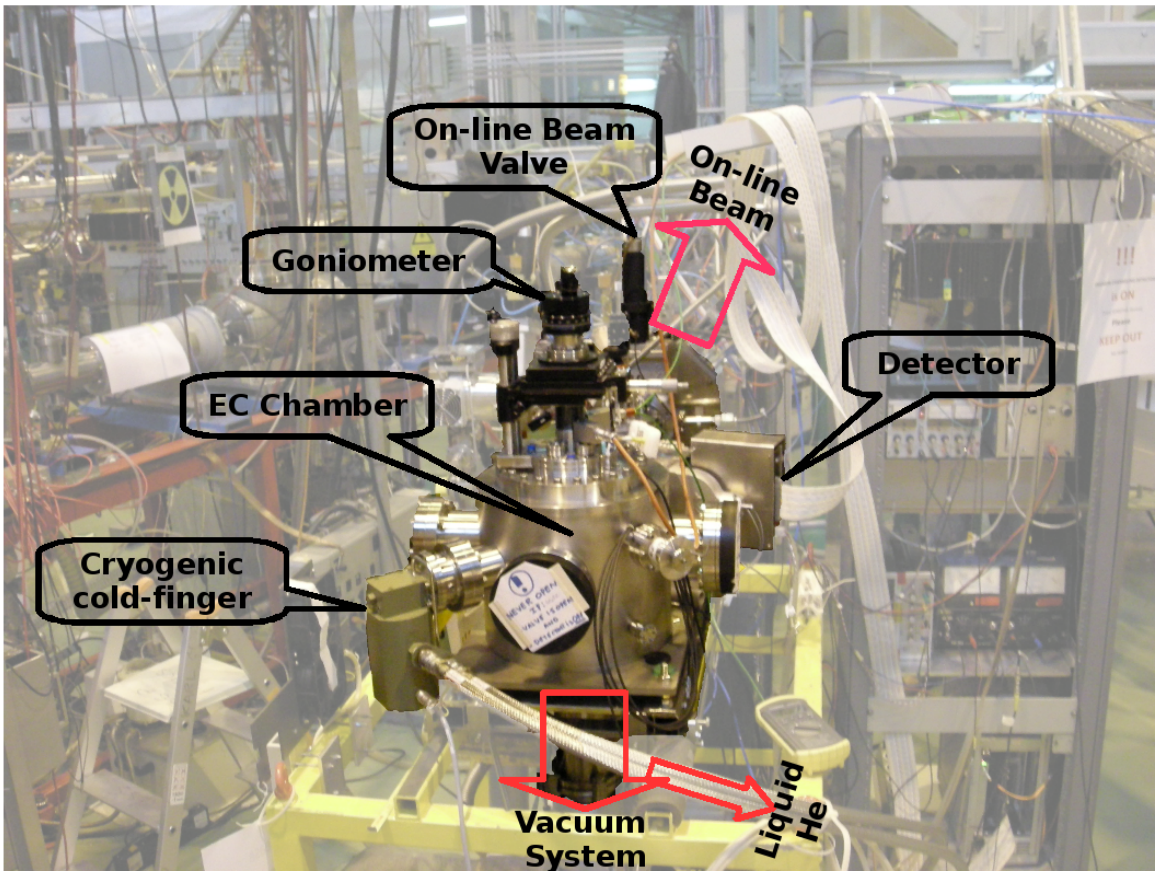

(b) on-line chamber mounted at an ISOLDE beam line

Figure 3.11: The setup mounted in the on-line beam line at ISOLDE.

EC resolution

The angular resolution of the EC experiments is calculated by the detection resolution and the emitter resolution, assuming both approximated to two-dimensional isotropic Gaussians with standart deviations of σ_d and σ_e respectively and a distance between the sample and the detector d:

$$\Delta\theta = \frac{\sqrt{\sigma_e^2 + \sigma_d^2}}{d} \tag{3.15}$$

The detection resolution on its turn depends on the setup and detector geometry, and the detector "pixel" resolution.

The emitter resolution depends on the size of the implantation spot, since the charged particles are

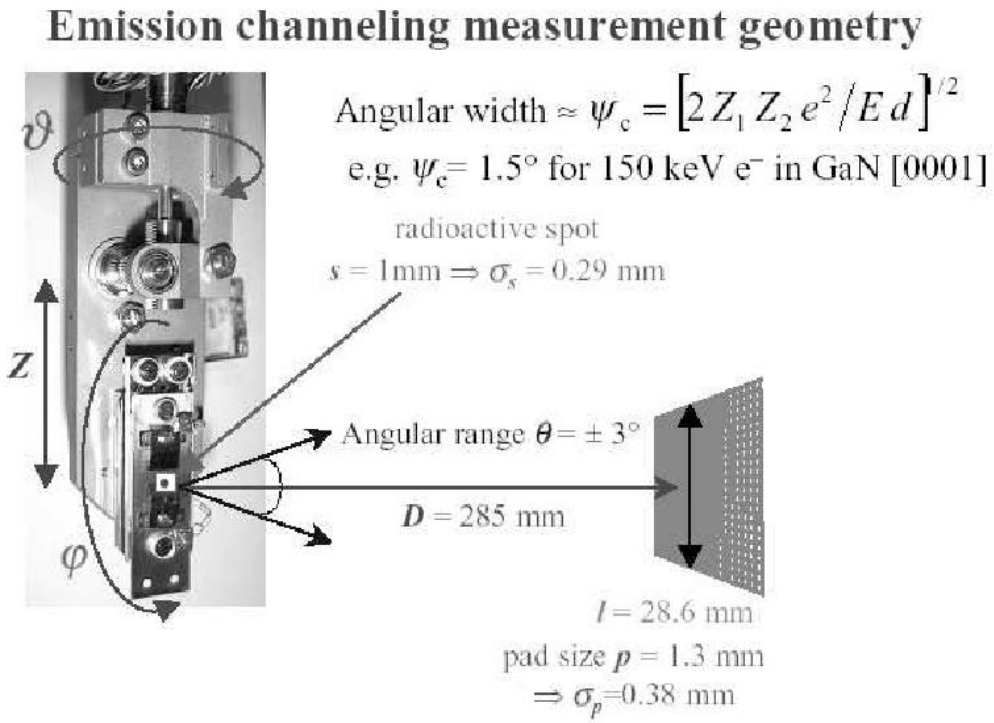

Figure 3.12: Resolution of the EC technique.[1]

produced by the implantanted isotopes and it is difficult to achieve beam spots much smaller than $1mm$ diameter. This is taken into account in the simulations using a Gaussian smoothing corresponding to the spot size.

Additionally to the size of the spot, another thing that influences the resolution is the fact that the measurement is done in different orientations, for which the ion distribution is no longer isotropic, but due to the angle between implantation and detection, the distribution is ellipsoidal. However this effect has been neglected in the analysis.

Implantation values

The isotopes implanted in the crystal cause defects along their trajectory. To minimize the influence of such defects with the channeling effect the implantion must be of small concentration, relatively to the crystal density. Usually, for EC experiments, depending on the sample's structural resistance and Half-life of the isotope/elements of study, the implantation doses range from $10^{12} - 10^{14} atoms/cm^2$. The ion beam is collimated to a 1mm diameter spot at the sample, the distribution of the ions in depth is approximately a Gaussian. Using the program SRIM [15][1] the simulated distribution of the ^{111}In atoms, for 50keV beam

[1]SRIM consists of "a group of programs which calculate the stopping and range of ions (up to 2 GeV/amu) into matter using a quantum mechanical treatment of ion-atom collisions... During the collisions, the ion and atom have a screened Coulomb collision, including exchange and correlation interactions between the overlapping electron shells."-[15]

has full width at half maximum of $FWHM = 116\mathring{A}$, an expected range $= 241\mathring{A}$ and a maximum of $\rho_{^{111}In} = 7.0 \times 10^{18}\, at/cm^3$.

3.5 Implantation parameters

Implantation

- date: 09/09/2008 07:00 to 09:57
- beam line: GLM-ISOLDE
- sample: 312
- element: ^{111}In
- collimator: $1mm$ diameter
- energy: $50keV$
- number of ions: $1.6 \times 10^{11} ions$
- dose: $2 \times 10^{13} cm^{-2}$
- tilt angle: 10^o
- pressure: $10^{-7} mbar$

Using the SRIM program [15] the implantation ion range and target damage were simulated, the results were plotted as $\frac{atoms/cm^3}{at/cm^2}$. From the resulting plot one can easily calculate the density distribution, multiplying the distribution values by the dose. Obtaining a maximum value of implanted ion density of $\rho_{^{111}In} = 7.0 \times 10^{18}\, at/cm^3$. Since the density of the sample is $\rho_{InP} = 4.81\, g/mol = 1.99 \times 10^{22}\, atoms_{In}/cm^3$, the ratio of probe/sample atoms is $\sim 352\, ppm$. Other than the ion distribution, the program provides the calculus of the damage done by the implantation, i.e., it calculates in particular the mean number of vacancies caused per ion of the beam. In this simulation the value given was of $593\, vacancies/ion$, this implies a density of defects of $20 at\% at 0K$. A big fraction of these defects are eliminated at room temperature and most of it after the annealing at 300^oC. It is for this reason and to make sure that the implanted ions get to their lower energy lattice location, that the annealing is so important in the sample preparation for the emission channeling technique as in any activation process on a material using implantation.

Tilt angle

The surface orientation is also normally a preferential orientation of the crystal, therefore if the implantation occurred along the orientation of a principal axis of the crystal, the ions would be channeled through the crystal and the depth of implantation would increase. Also the implantation would lose its Gaussian depth profile, which would complicate the simulation of implantation profile.

In order to prevent this effect, the crystal is mounted with a slight tilt angle of 10 degrees.

Annealing

The implantation method creates a cascade of defects and the annealing is a process of heating, used to recover the crystal lattices. Also the implanted isotopes may not be in their preferential location, either because they had no energy or the crystal structure was not in its perfect form. Giving thermal energy the atoms and isotopes will gain the energy to reorganize in the most stable lattice sites. The annealing done on the sample for this work was of 10 min at 300^oC.

Cooling station

Principles of the cooling system developed within the scope of this work

The general concept behind refrigeration is the Carnot cycle. If one considers a cylinder with two entries of gas, one more pressurized than the other, with a piston and a compressor with refrigerant gas, the carnot cycle mainly consists in the exchange of work for the transfer of heat from a cold source to a hot source. The pressurized gas produces work against the piston (the piston is moved up, with the entrance of the refrigerating gas), with an isothermal expansion. Then the gas is allowed to expand lowering the temperature, with an adiabatic expansion, and the heat is transmitted from the cold source to the gas. Afterwords pushing the piston the gas is pressured out of the cylinder, closing the cycle with an adiabatic compression and transferring heat from the gas to the hot source. The process is illustrated in a plot of pressure as function of the volume (3.13).

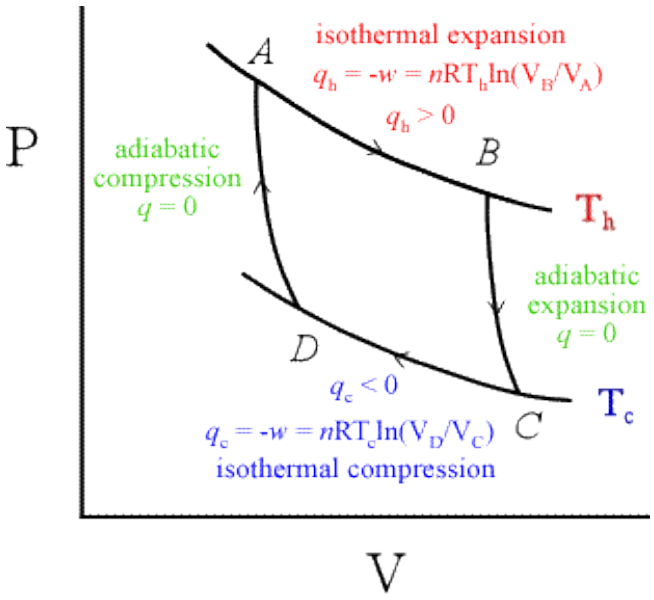

Figure 3.13: Carnot Cycle[41]

Cooling station blocks

The cooling station mounted on the EC chamber can be divided in five main parts [12]:

- The compressor, a large block that produces the power work needed to keep an entry at low pressure and one at high pressure (3.14a).
- The cold finger, a device in which the cycle of helium will take place and so all the process of cooling (3.14b).
- A resistance is applied around the cold finger to control the temperature, since the cycles lead allways to decrease temperature with a constant duty cycle. A diode is attached to the cold-finger as the reference temperature gauge.
- The controller calculates the current needed to heat the resistance in order to achieve a set point temperature in the reference diode (3.14c).
- Conduction path - conductive path that transmits the cold-finger second cycle cold (b2) to the sample(3.14d) .
- The shielding - Since the setup is in high-vacuum conduction at the sample holder and radiation are the most important means of heat transfer. In order to reduce the radiation on it the shield conducts cold (of the cold-finger second stage) through its path, allowing the movements of the goniometer and still covering all the conduction path (3.14e). This is also a mechanism to prevent the condensation of residual gases on the sample surface due to the large difference of temperature between the walls of the chamber, at room temperature, and the low temperature sample holder.

(a) Helium compressor

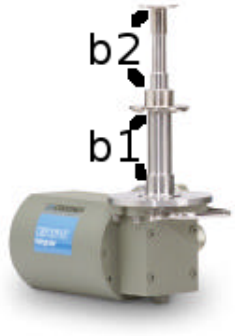

(b) Cryogenic refrigerator head

(c) Process controller

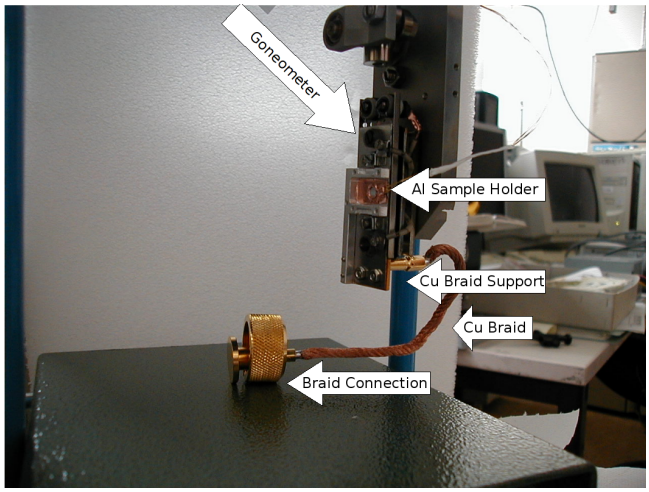

(d) Conduction Path

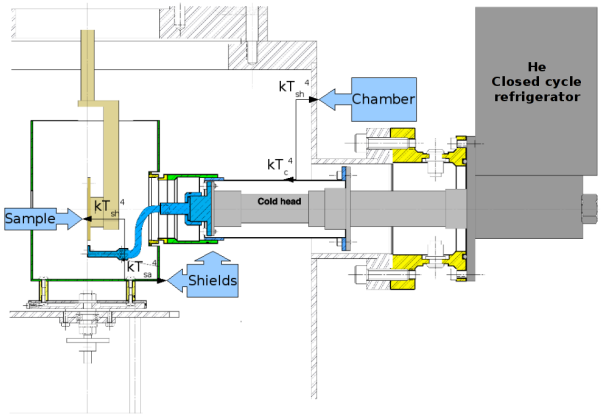

(e) Shielding

Figure 3.14: Cooling parts

Temperature study of the setup

The plot of figure 3.15 shows the lowering of the temperature as a function of time from room temperature with the heating power supplies "off"[12].

In order to stabilise the temperature with values between 50k and room temperature, (namely 100K, 150K and 200K), the high temperature annealing block of the goniometer was used to control the sample's temperature. The cooling station is equipped with a heater to control the temperature, which is placed in the cold-finger second stage, however the goniometer heater is much closer to the sample which consists of a considerable advantage in the control feedback. The temperature controller of the goniometer annealing block regulates the power needed to compensate the difference between the set-point and the measurered temperature ($T_{reference}$).

With this setup the cold-finger (second stage of the refrigerator) varies from 10 to 25k with temperature of the sample holder ranging the 50-200K. For this range of temperatures, the cooling power is about 1,4 Watt. The power of the goniometer heater was limitted to about 1watt, by limitting the heater's current (I). So the heater and the cold-finger would reach an equilibrium of heat flow to the sample, providing a specific and stable temperature in the sample.

Knowing the resistance of the goniometer annealing block (R), measured at room temperature to be 0.7Ωand at 50K is 0.5Ω, the power was easily calculated using the formula $P = I^2R$. There are however the heat sources during the extent of the cooling path, this means a drop of the cooling power from the cold-finger to the sample holder, i. e., the effective power of the cold-finger concerning the sample is lower than the 1,4 watt the cold-finger actually gives. The goniometer heater also has limited contact with the sample holder, since there was the need to isolate as much as possible the sample from the goniometer, to prevent it to behave as a room temperature heat source, which represents a loss of power from the heater to the sample holder.

The current limit was tuned by hand and in the end the power provided by the goniometer annealing block

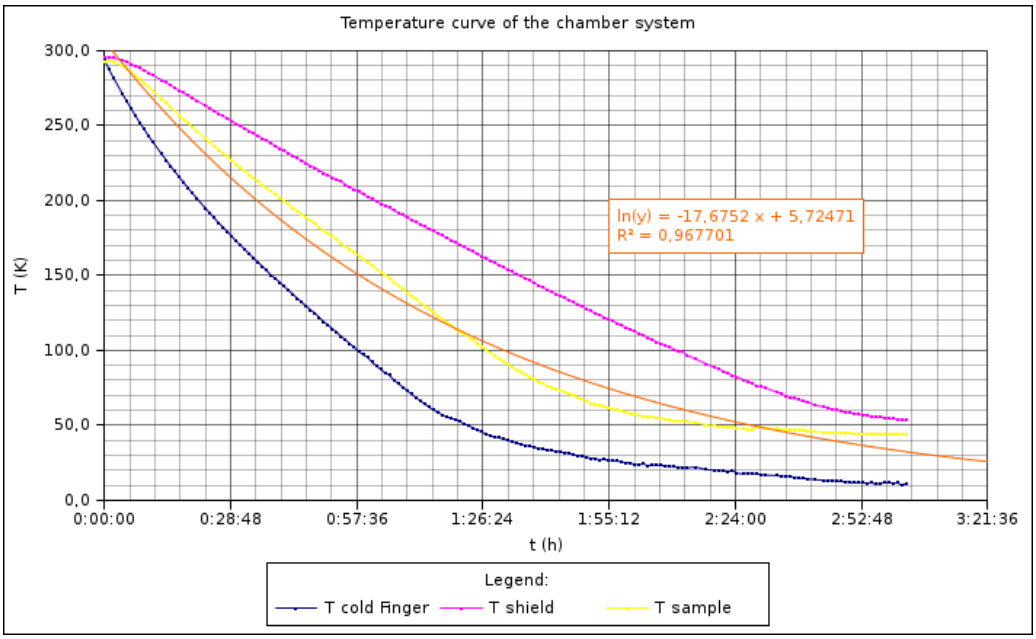

Figure 3.15: Temperature curve for the cold-finger, shield and sample as function of time

(P_{heater}), to stabilize the sample temperature (T_{sample}) around 100K,was of about 0.8 watt, for a set point temperature ($T_{setpoint}$) of 152K. If we consider no loss of power from the annealing block, one can roughly estimate an effective power of the cooling system, since this has to mach the calculated value for the goniometer annealing block in equilibrium, i. e., a drop of about 0.6 watt from that which the cold-finger provides. These values, for different temperatures, are shown in the table 3.10. The stabilization of the temperature as a function

Power exchange to the sample holder						
$T_{sample}(K)$	$T_{reference}(K)$	$T_{setpoint}(K)$	I_{heater} (Å)	$I_{limit}(\mathring{A})$	P_{heater} (watt)	$P_{difference}$ (watt)
101	15.0	152	1.15	2.0	0.79	0.61
150	20.0	220	1.35	2.5	1.09	0.31
200	25.5	303	1.35	2.5	1.09	0.31

Table 3.10: The difference of power calculated between the goniometer annealing block and the cold-finger.

of the set point is plotted in 3.16.

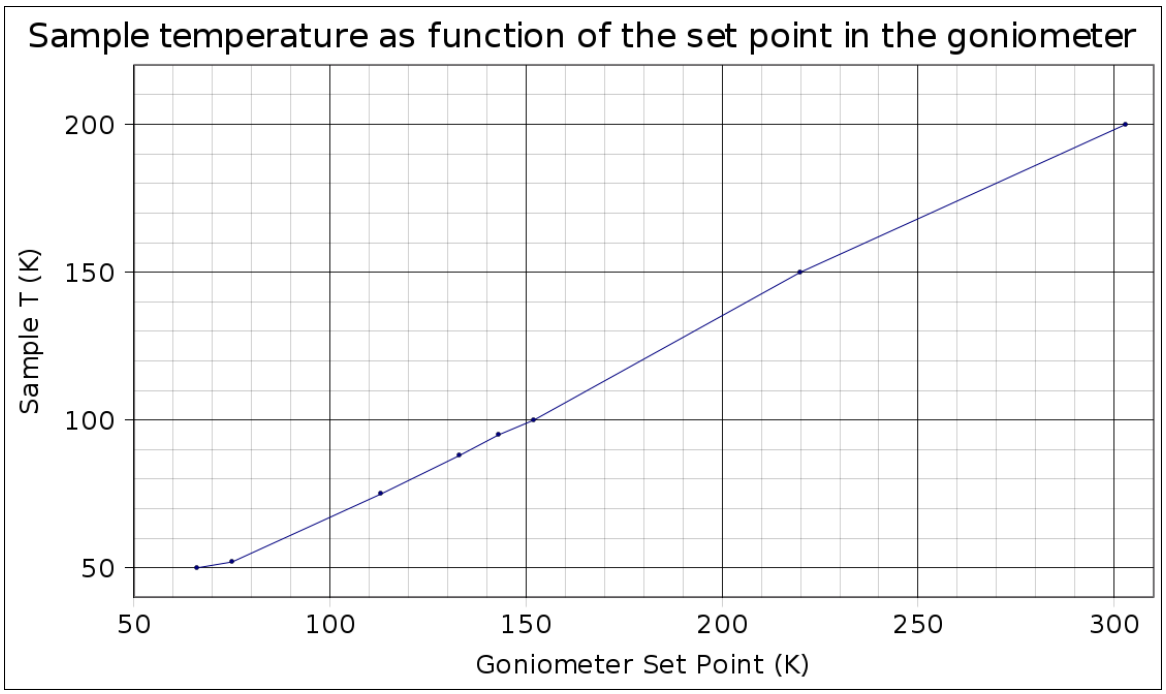

Figure 3.16: Temperature curve for the sample as function of the set point in the goniometer annealing heater controller

4 Results

Measurements

- dates: 09/09/2008 to 21/09/2008
- local: in-line with ISOLDE beam line
- orientations: $< 100 >$, $< 110 >$, $< 111 >$ and $< 211 >$
- time collecting: from 4 hours to 2 days per axis, increased due to the reducing activity of the sample
- pressure: 10^{-6} to 10^{-7} mbar The measurements were taken by the order shown in the table 4.1.

Beginning time of each measurement			
Experiment id	T (K)	Start time (dd-mm-yy hh:mm)	orientation
vat0275.dat	RT	09-9-08 16:19	$< 100 >$
vat0281.dat	RT	10-9-08 08:28	$< 110 >$
vat0280.dat	RT	10-9-08 04:20	$< 111 >$
vat0279.dat	RT	10-9-08 00:20	$< 211 >$
vat0310.dat	200	15-9-08 13:13	$< 100 >$
vat0311.dat	200	16-9-08 08:38	$< 110 >$
vat0312.dat	200	17-9-08 10:32	$< 111 >$
vat0313.dat	200	19-9-08 09:52	$< 211 >$
vat0307.dat	150	13-9-08 23:29	$< 100 >$
vat0305.dat	150	13-9-08 09:17	$< 110 >$
vat0309.dat	150	14-9-08 21:39	$< 111 >$
vat0308.dat	150	14-9-08 08:42	$< 211 >$
vat0298_0	100	11-9-08 18:53	$< 100 >$
vat0303_0	100	12-9-08 21:19	$< 110 >$
vat0300_0	100	12-9-08 04:39	$< 111 >$
vat0302_0	100	12-9-08 13:12	$< 211 >$
vat0297.dat	50	11-9-08 12:51	$< 100 >$
vat0287.dat	50	10-9-08 17:30	$< 110 >$
vat0289.dat	50	10-9-08 21:27	$< 111 >$
vat0294.dat	50	11-9-08 05:10	$< 211 >$

Table 4.1: Experiments done in time

Integral energy spectrum

After the implantation of 111In isotopes into an InP single crystal, the sample was annealed at 300C. The decay $^{111}In \rightarrow {}^{111}Cd$ conversion electrons were collected with a position sensitive detector, in 4 directions ($< 100 >, < 110 >, < 111 > and < 211 >$), from room temperature (300^{o}K) down to 50K.

The energy spectrum of electrons detected was integrated for each energy, calibrated and is shown in the figure 4.1.

As one can see there are 4 distinct peaks, in the energies expected (calculated earlier in table 3.8). The

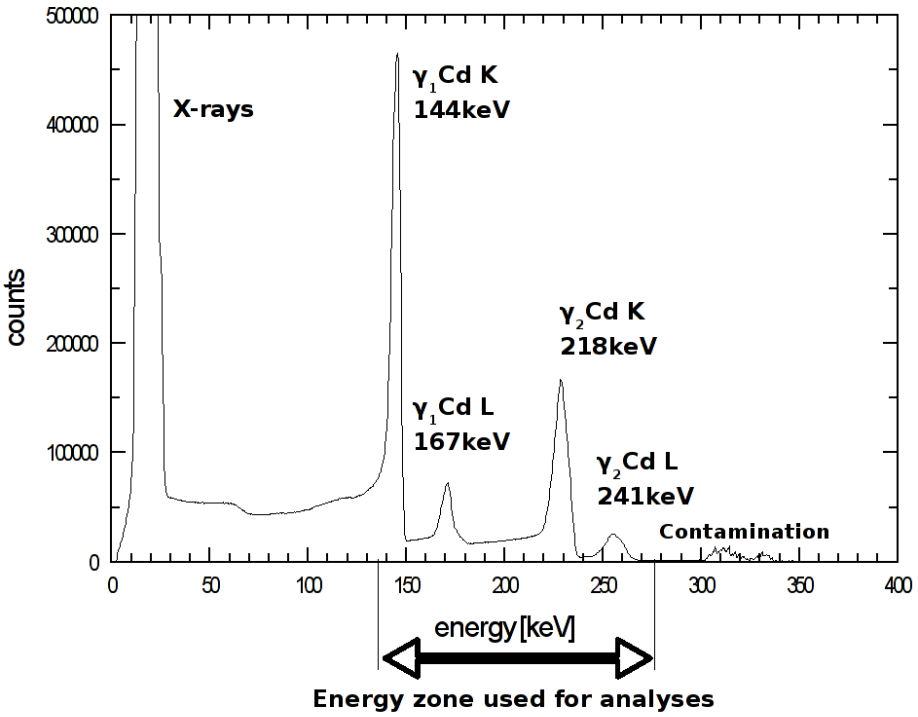

Figure 4.1: The spectrum of electrons.

conversion electrons of the K and L shell are represented in the two bands, since the difference of energies between L shell electrons is small, on the $\gamma_1 K$ it is $144.6keV$, on $\gamma_1 L1$ it is $167.3keV$, on $\gamma_1 L2$ it is $167.6keV$, on $\gamma_2 K$ it is $218.7keV$, on $\gamma_2 L1$ it is $241.4keV$ and on $\gamma_2 L2$ it is $241.7keV$. The value of $\gamma_1 K$, was used for the calibration of the spectrum. Note that the preamplified chips of the detector saturate around 300-340 keV, so that all electrons which deposit a higher energy in the detector appear in the spectrum in this region. In this sample, they are the result of a slight contamination with another isotope as will be shown latter.

4.1 Experimental patterns

The data, either the collected or the simulated patterns, are plotted in two dimensions with a color code. The two dimensions are relative to the position in degrees, and the colors give the yield.

Obtained two dimensional anisotropy intensity electron spectrum

The data obtained in the experiments measurements is illustrated in the plots of the figure 4.2. These patterns are the results of the measurements in an energy window between 135keV and 275keV, so the background is mostly lost. The obtained total counts of a spectrum per axis measured may be very different depending on the statistics of the measurement and in order to compare them one has to normalize the experimental values. As a first approach the patterns were fitted with the theoretically expected simulated patterns for $^{111}In/^{111}Cd$ in In sites of the lattice. Hence the simulations are created normalized, the ratio between the simulations and experimental mean values is multiplied to the experimental values, and in a way these get normalized.

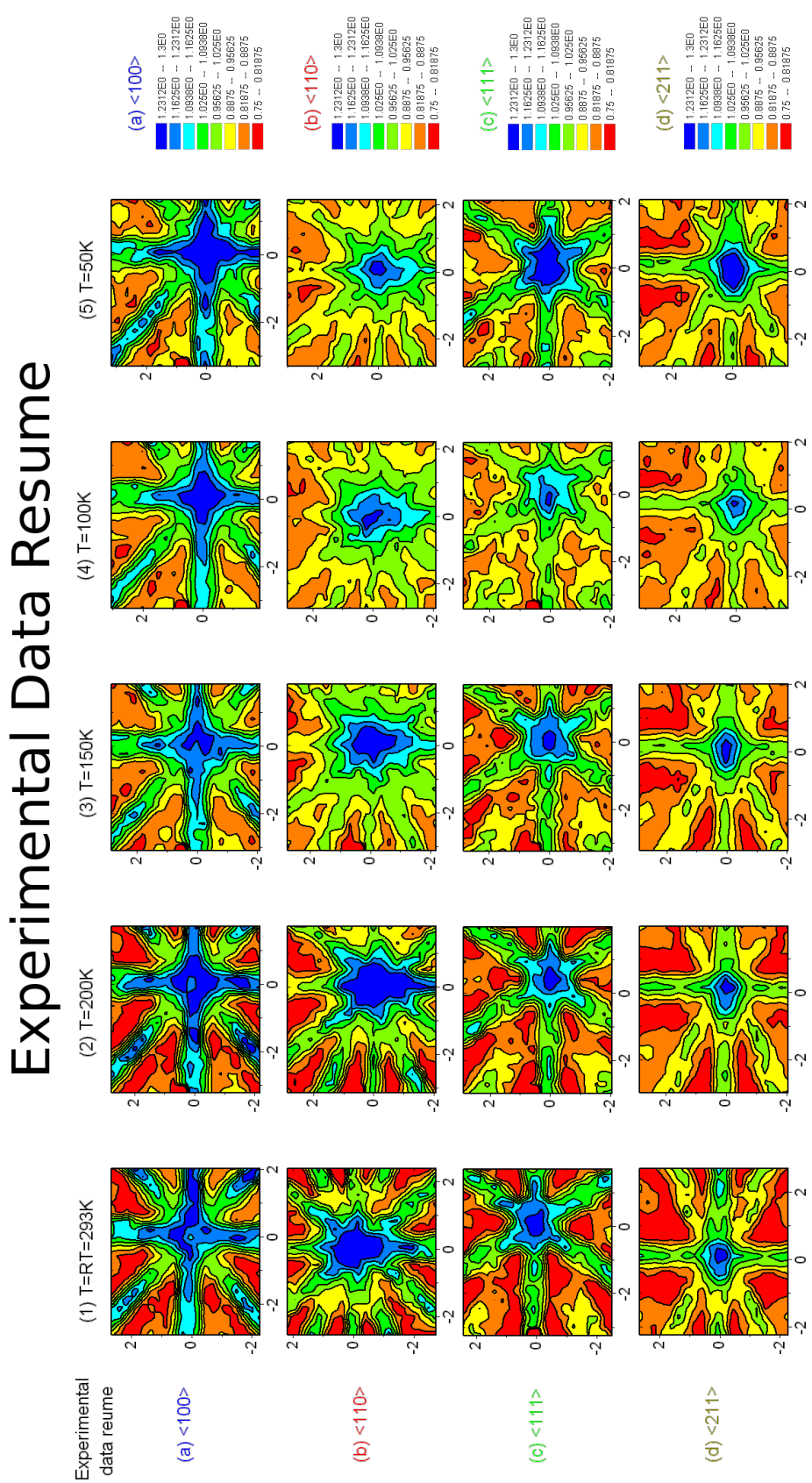

Figure 4.2: Electron intensity two-dimensional anisotropy patterns. The Blue color means high intensity and red low intensity of c.e. electrons, the values for the color code are in the legend of each pattern row.

4.2 simulations

Simulation sets were done for:

- each orientation: $< 100 >$, $< 110 >$, $< 111 >$ and $< 211 >$
- for each temperatures: Room temperature (RT) as 293K and from 200K to 50K in steps of 50K
- Each set included the sites and displacements between sites[1] (figure 4.3), for the theoretically expected vibration:

  S_{In}/S_V or S_P/S_{III} substitutional - in the place of an original element of the crystal, with u_1 from 0.04 to 0.4 Å in steps of 0.01 Å

  T_{In}/T_V or T_P/T_{III} tetrahedral interstitial - in the major interstitial sites between the lattice atoms.

  BC bond-center -in the center of the bond between the two elements of the crystal

  H hexagonal

  Q_{In}/Q_V or Q_P/Q_{III} anti-bonding sites.

  C_{In}/C_V or C_P/C_{III}

  S_{In}/S_V or S_P/S_{III} - the so called $< 100 >$ split sites split

  Y_{In}/Y_V or Y_P/Y_{III} - the so called ytterbium sites

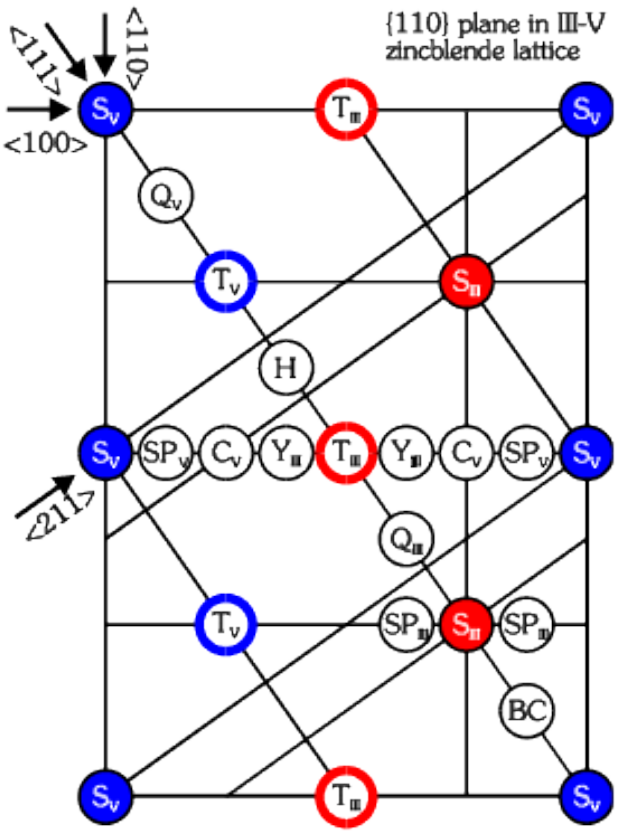

Figure 4.3: The used mapping for lattice sites[1].

[1]These displacements are identified by the factor of displacement. Only the substitutions sites with different u_1 were simulated without exception, due to computing time limitations.

Fitting the experimental data

Sites

For each experimental pattern, many simulations were tested. The results of the fitting are plotted in the figures 4.4, 4.5, 4.6, 4.7 and 4.8. The minimums of the curves plotted in figure are not very explicit, but should determine the factor and u_1 of the best fit. Also one can compare the χ^2 variation as a function of either the displacement or the u_1. For example the $< 110 >$ orientation at room temperature the displacement seems to influence more than the vibration u_1, so it points to the conclusion that the factor is indeed null. The theoretically expected simulations can be compared to the obtained data along with the theoretically simulations that best fitted in the figure 4.9. However the most theoretical best fitted patterns are slightly different from the expected ones, especially for the higher temperatures. The difference in u_1 of the expected and best fit are compiled in the plot 4.10. Also considering the variation of u_1 associated with a 5% variation of χ^2 one can estimate an error for the r.m.s. obtained, these values are included in the figure 4.10 in the ofrm of erro bars.

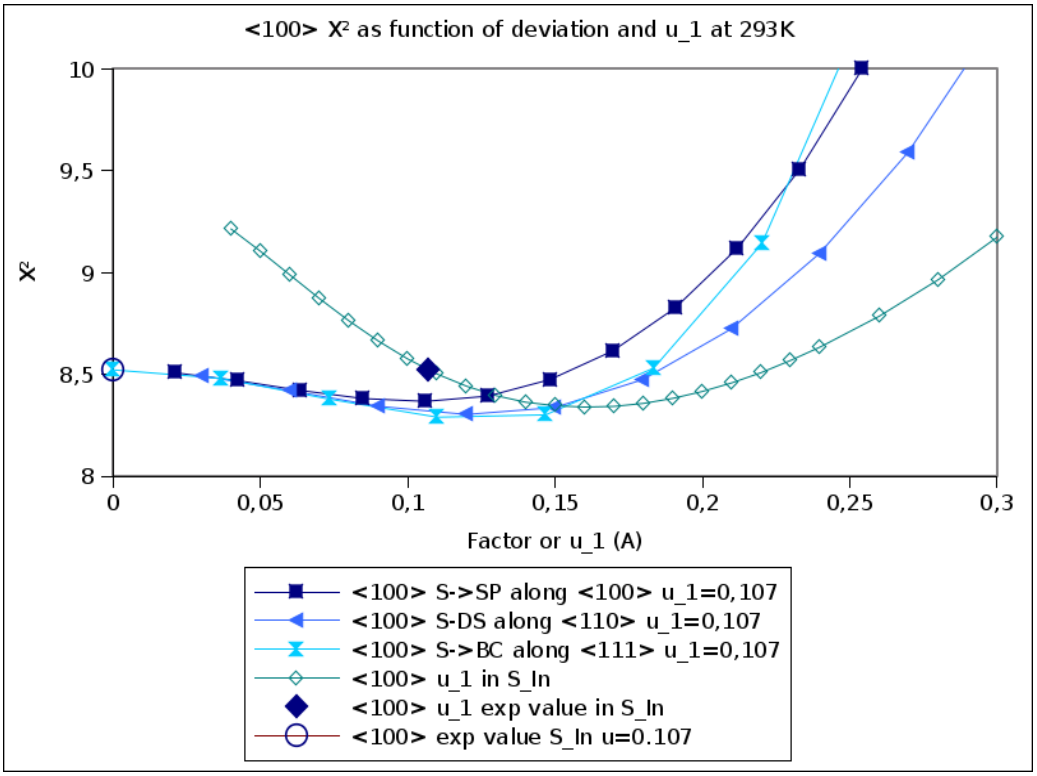

(a) At room temperature, for the orientation $< 100 >$, the χ^2 as a function of the u_1 and as a function of the displacement both in Å

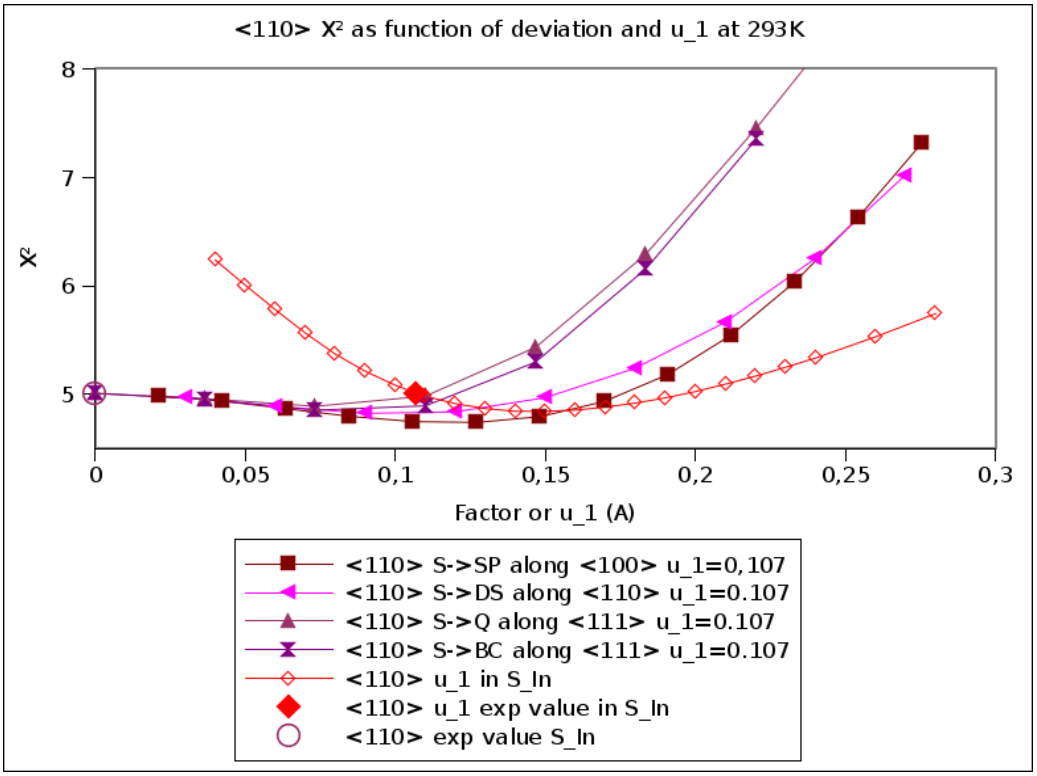

(a) At room temperature, for the orientation $< 110 >$, the χ^2 as a function of the u_1 and as a function of the displacement both in Å

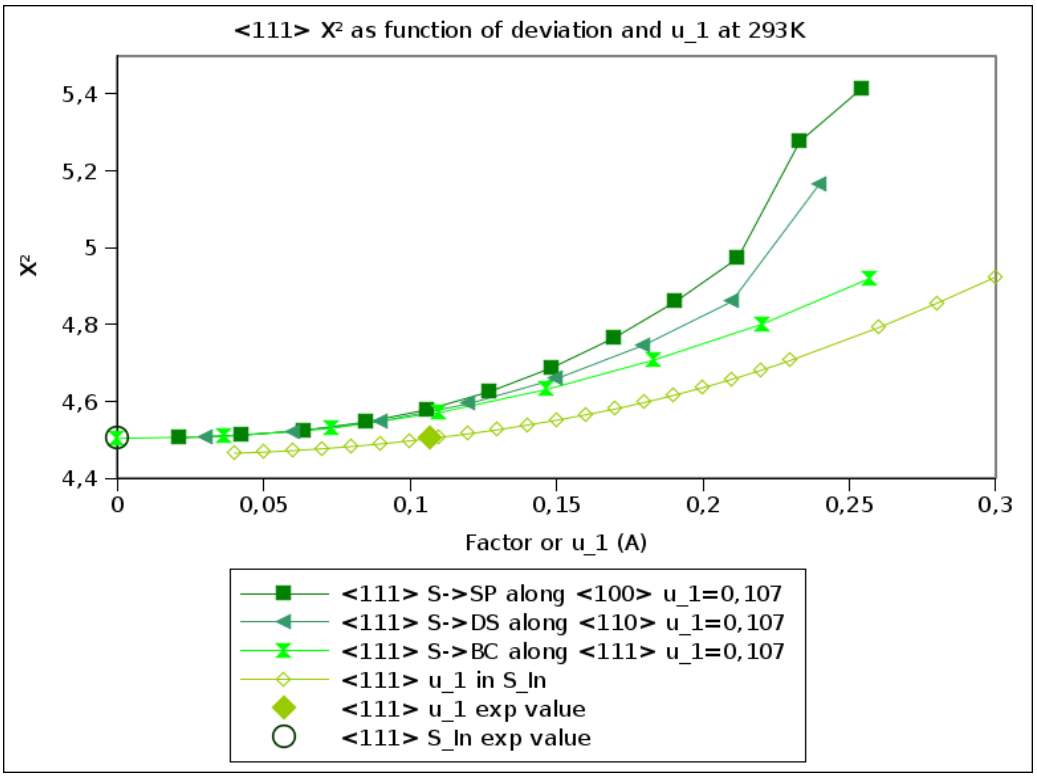

(a) At room temperature, for the orientation $< 111 >$, the χ^2 as a function of the u_1 and as a function of the displacement both in Å

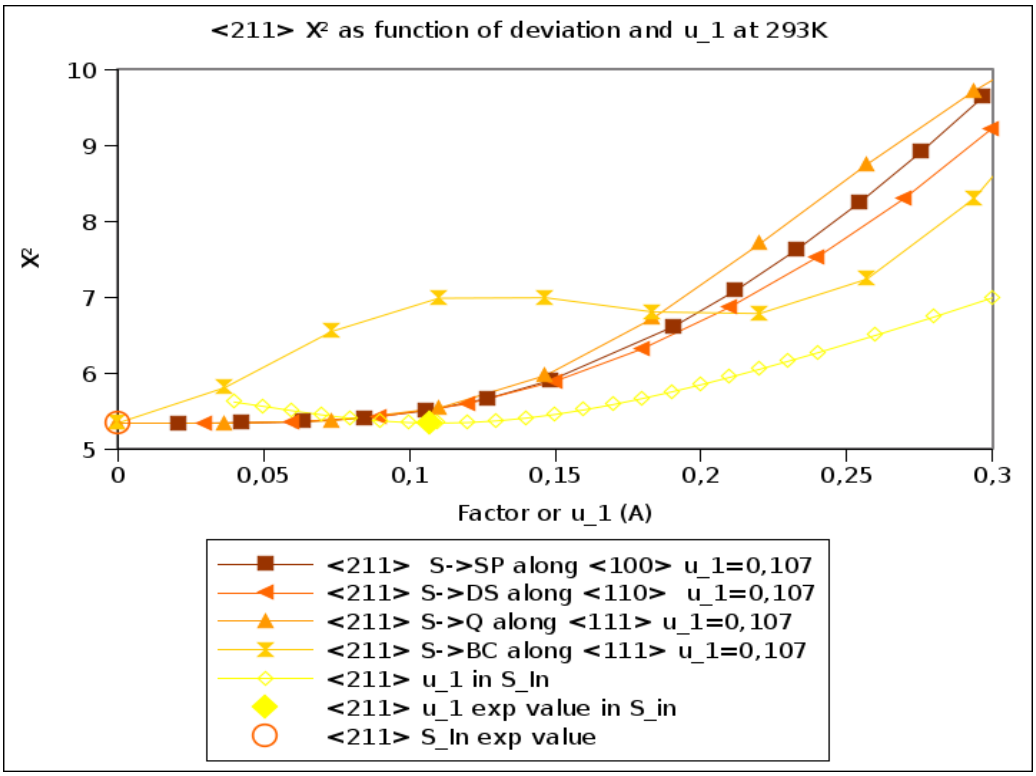

(a) At room temperature, for the orientation $< 211 >$, the χ^2 as a function of the u_1 and as a function of the displacement both in Å

Figure 4.4: These plots resume the χ^2 obtained as a result of fitting the patterns obtained at room temperature, for the four orientations ($< 100 >$, $< 110 >$, $< 111 >$, 211). In each plot the χ^2 is plotted as a function of the static displacement, from the substitutional lattice site, along different directions, for the u_1 values specified in the legend. Also the χ^2 are plotted as a function of the u_1, in the substitutional site.

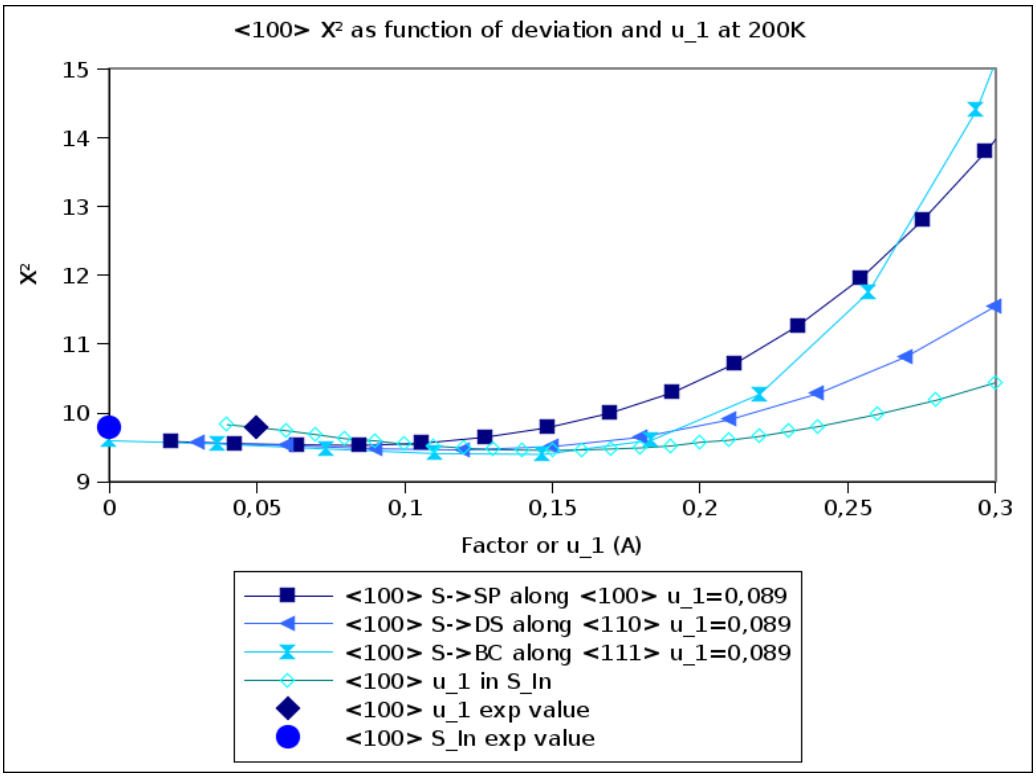

(a) At 200K the χ^2, for the orientation $< 100 >$, as a function of the u_1 and as a function of the displacement

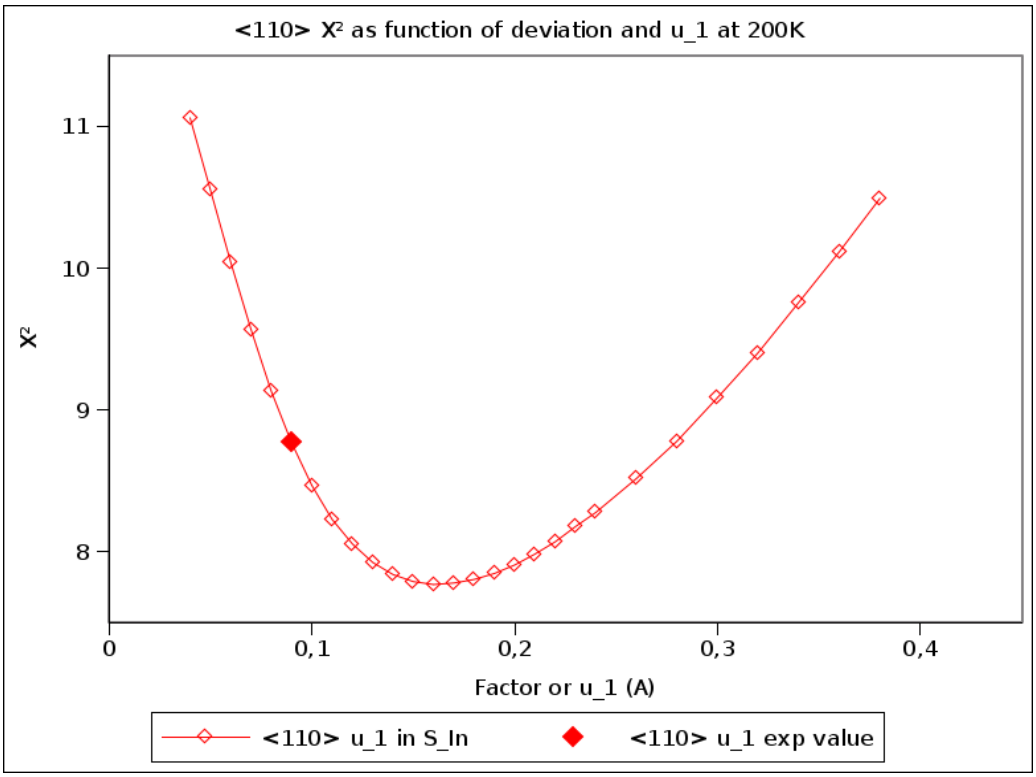

(b) At 200K the χ^2, for the orientation $< 110 >$, as a function of the u_1 and as a function of the displacement

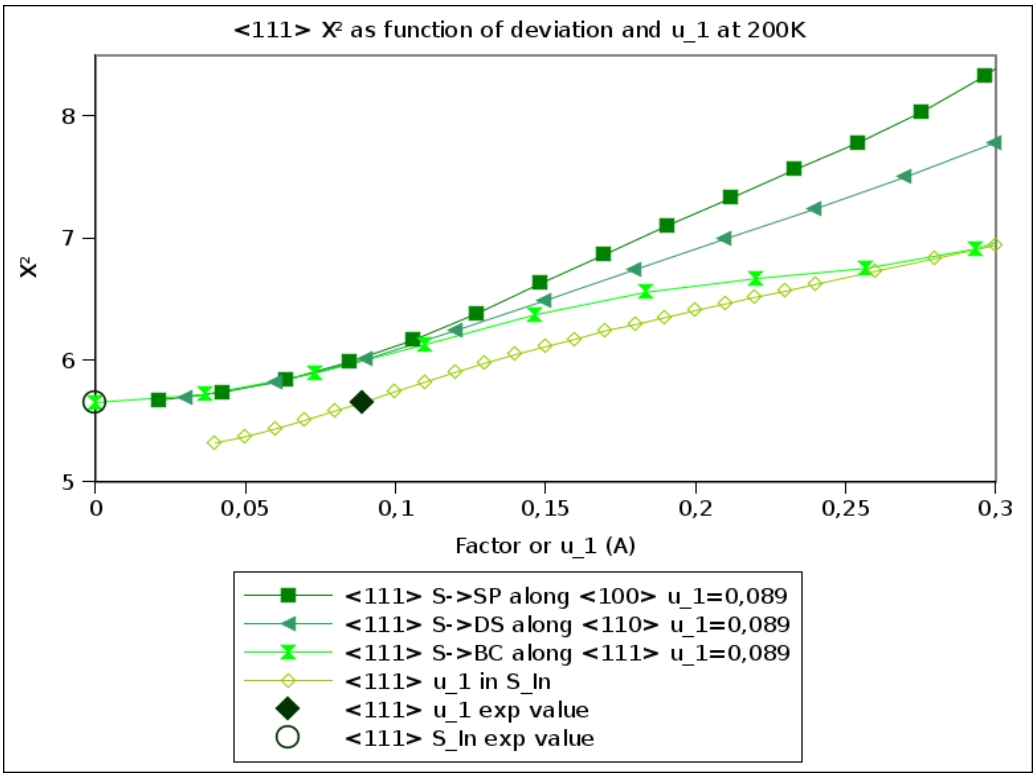

(c) At 200K the χ^2, for the orientation $< 111 >$, as a function of the u_1 and as a function of the displacement

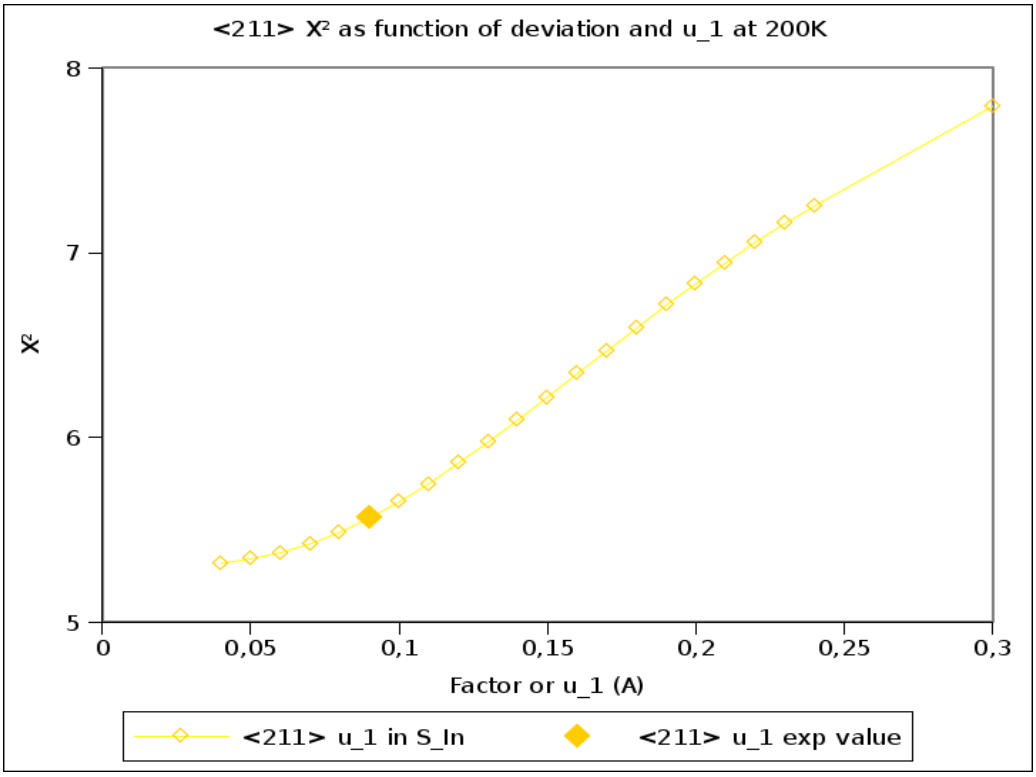

(d) At 200K the χ^2, for the orientation $< 211 >$, as a function of the u_1 and as a function of the displacement

Figure 4.5: These plots resume the χ^2 obtained as a result of fitting the patterns obtained at 200K, for the four orientations ($< 100 >$, $< 110 >$, $< 111 >$, 211). In each plot the χ^2 is plotted as a function of the static displacement, from the substitutional lattice site, along different directions, for the u_1 values specified in the legend. Also the χ^2 are plotted as a function of the u_1, in the substitutional site.

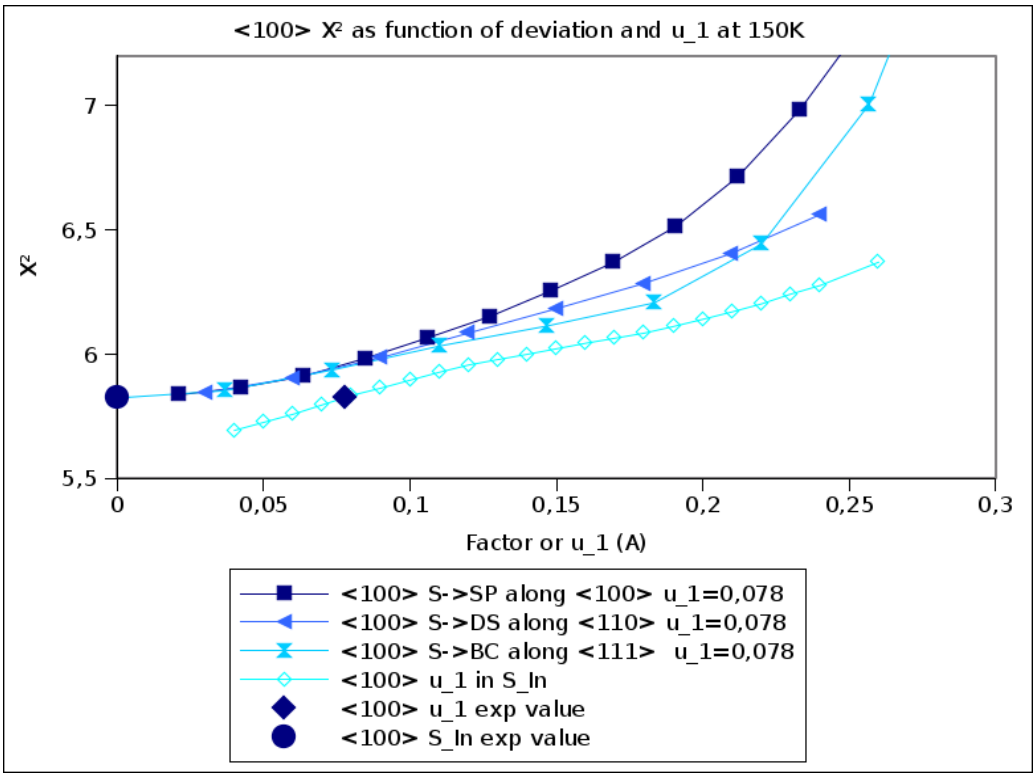

(a) At 150K the χ^2, for the orientation $< 100 >$, as a function of the u_1 and as a function of the displacement

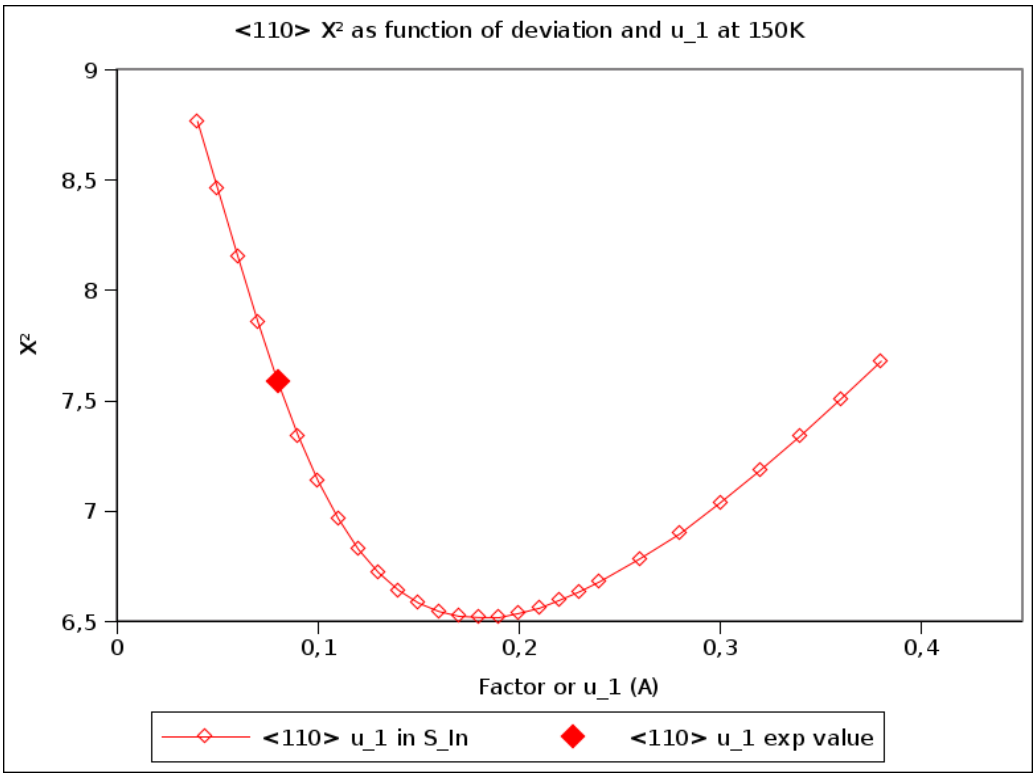

(b) At 150K the χ^2, for the orientation $< 110 >$, as a function of the u_1 and as a function of the displacement

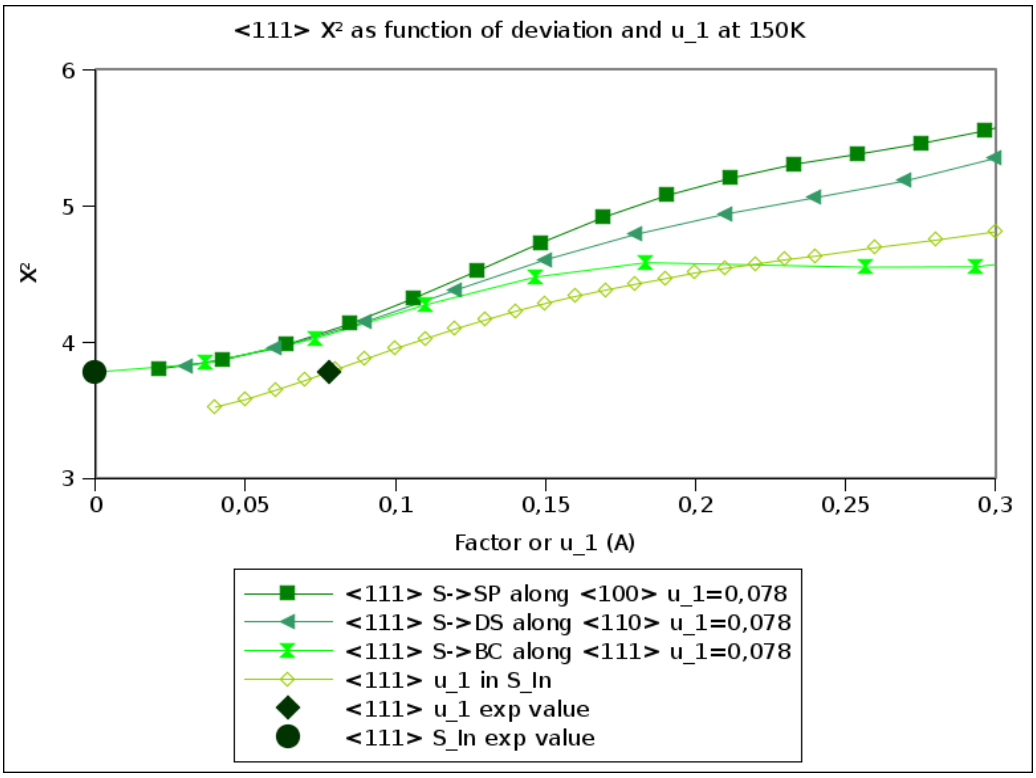

(c) At 150K the χ^2, for the orientation $< 111 >$, as a function of the u_1 and as a function of the displacement

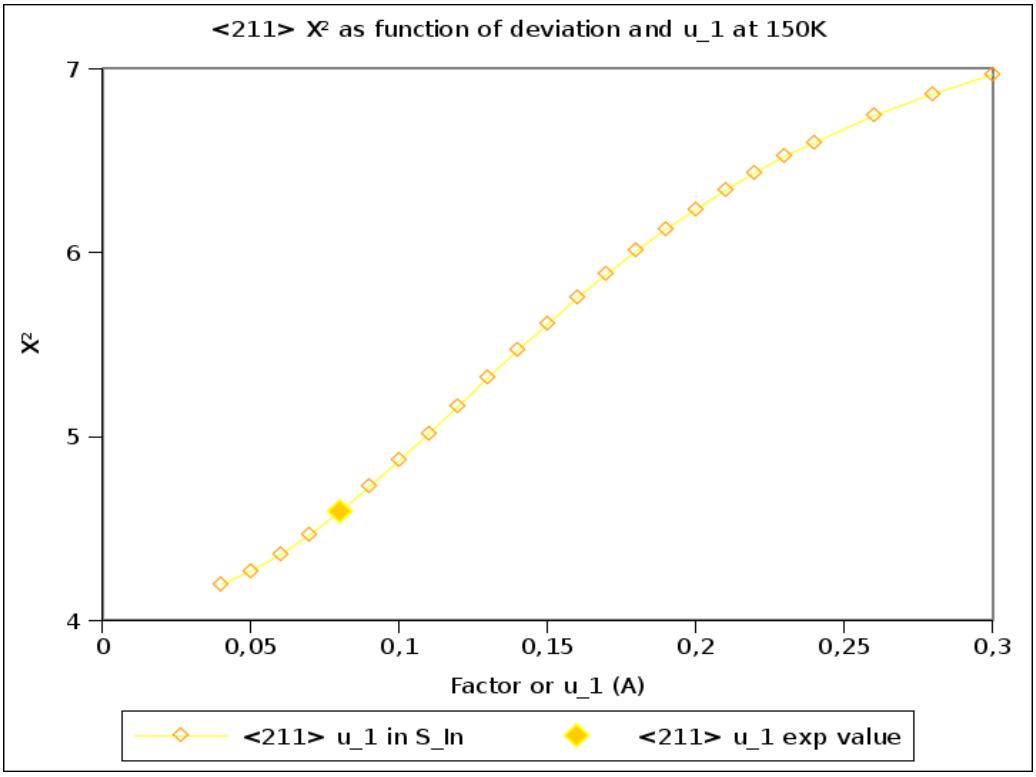

(d) At 150K the χ^2, for the orientation $< 211 >$, as a function of the u_1 and as a function of the displacement

Figure 4.6: These plots resume the χ^2 obtained as a result of fitting the patterns obtained at 150K, for the four orientations ($< 100 >$, $< 110 >$, $< 111 >$, 211). In each plot the χ^2 is plotted as a function of the static displacement, from the substitutional lattice site, along different directions, for the u_1 values specified in the legend. Also the χ^2 are plotted as a function of the u_1, in the substitutional site.

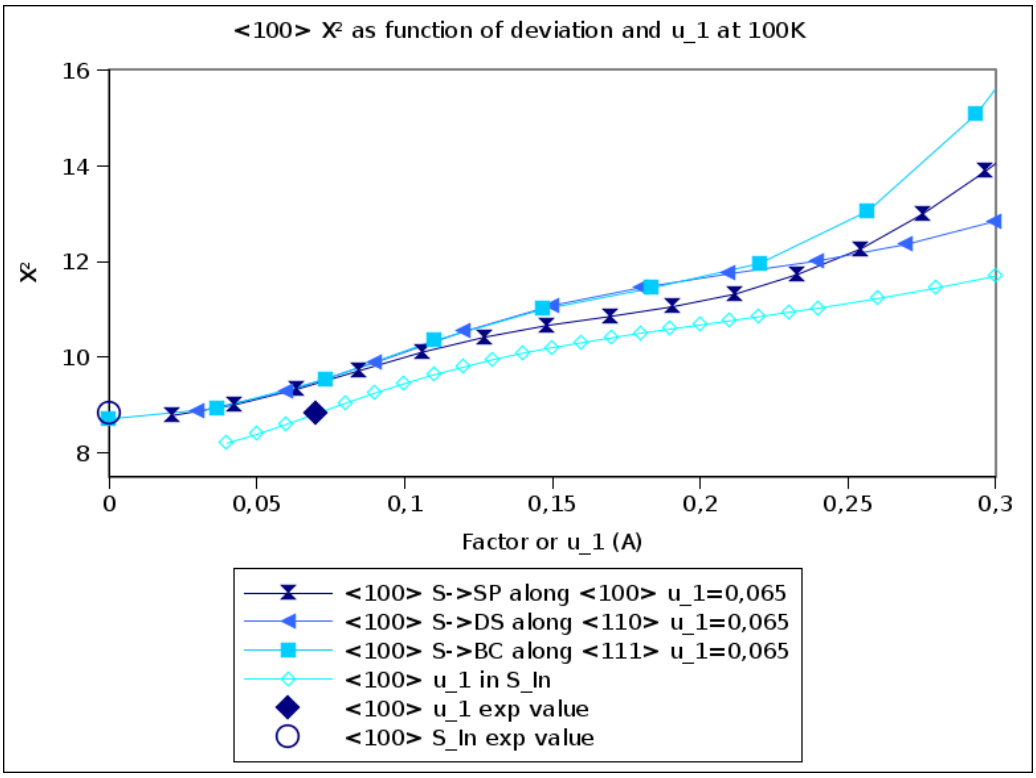

(a) At 100K the χ^2, for the orientation 100, as a function of the u_1 and as a function of the displacement

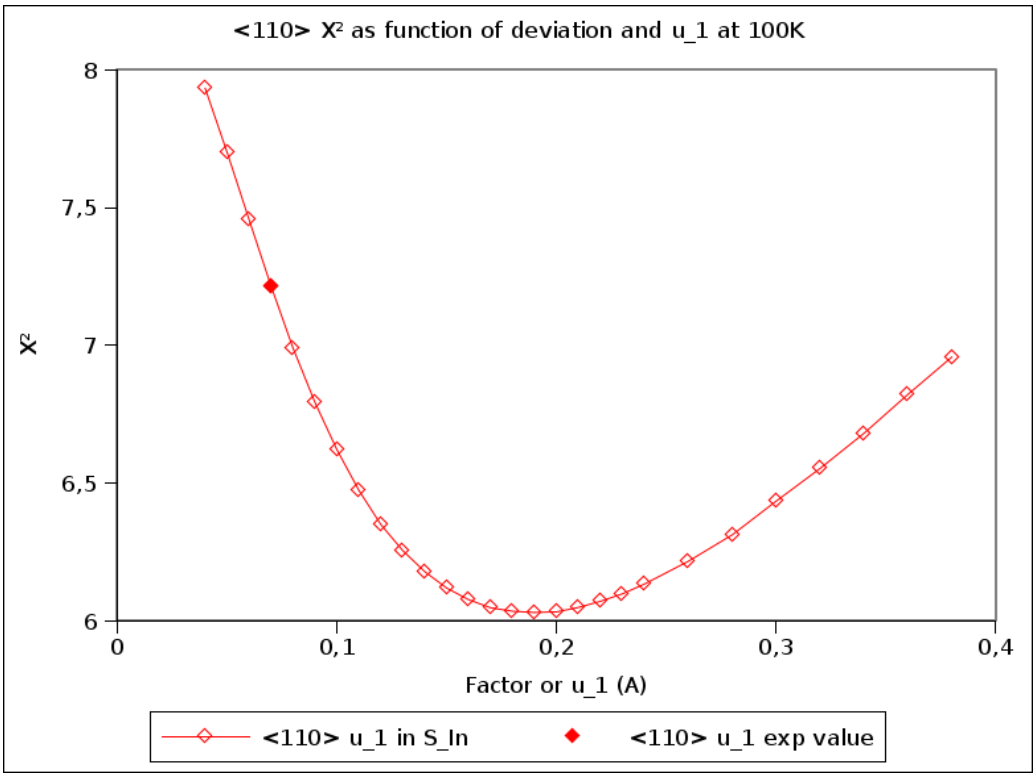

(b) At 100K the χ^2, for the orientation 110, as a function of the u_1 and as a function of the displacement

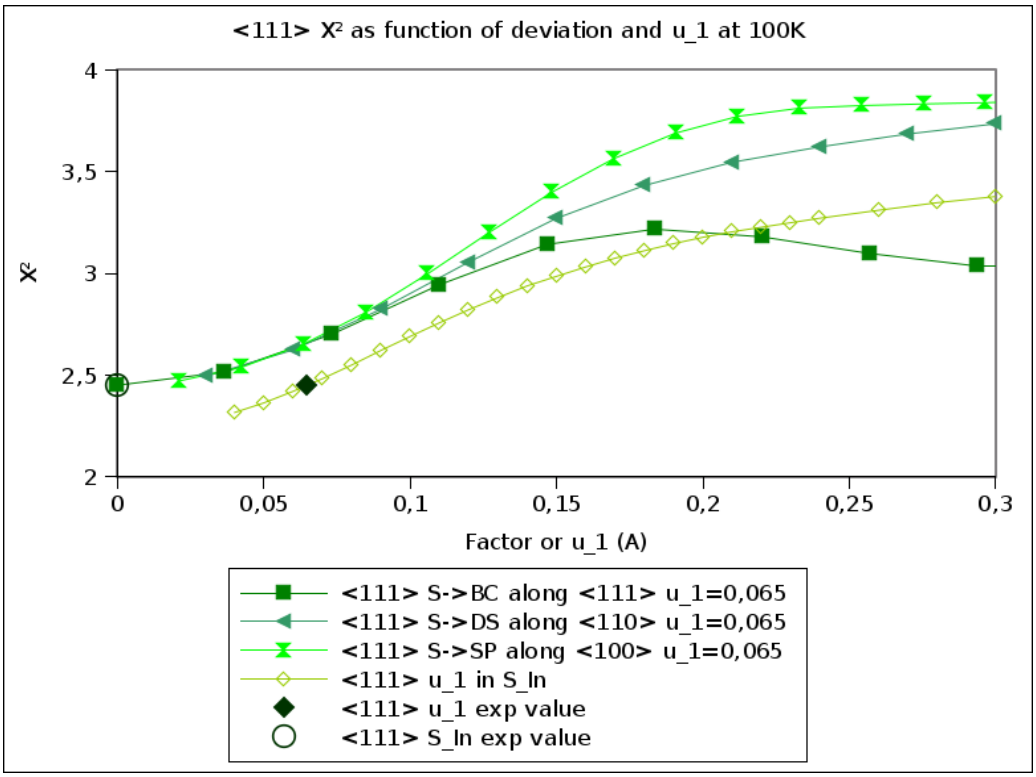

(c) At 100K the χ^2, for the orientation 111, as a function of the u_1 and as a function of the displacement

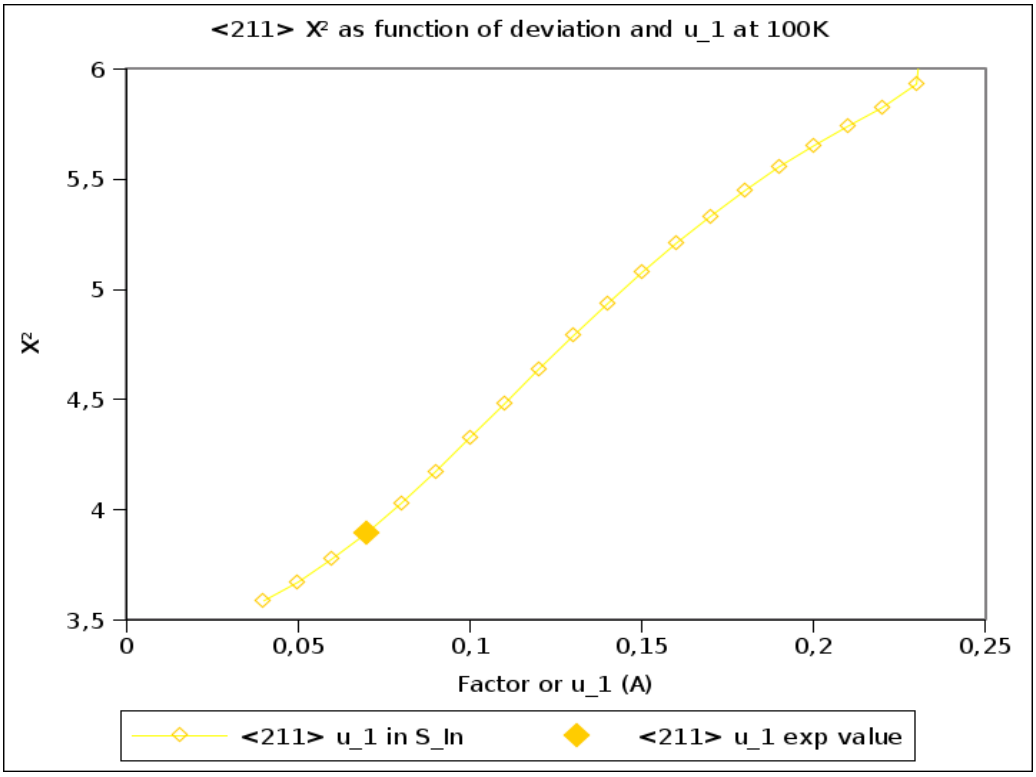

(d) At 100K the χ^2, for the orientation 211, as a function of the u_1 and as a function of the displacement

Figure 4.7: These plots resume the χ^2 obtained as a result of fitting the patterns obtained at 100K, for the four orientations ($< 100 >$, $< 110 >$, $< 111 >$, 211). In each plot the χ^2 is plotted as a function of the static displacement, from the substitutional lattice site, along different directions, for the u_1 values specified in the legend. Also the χ^2 are plotted as a function of the u_1, in the substitutional site.

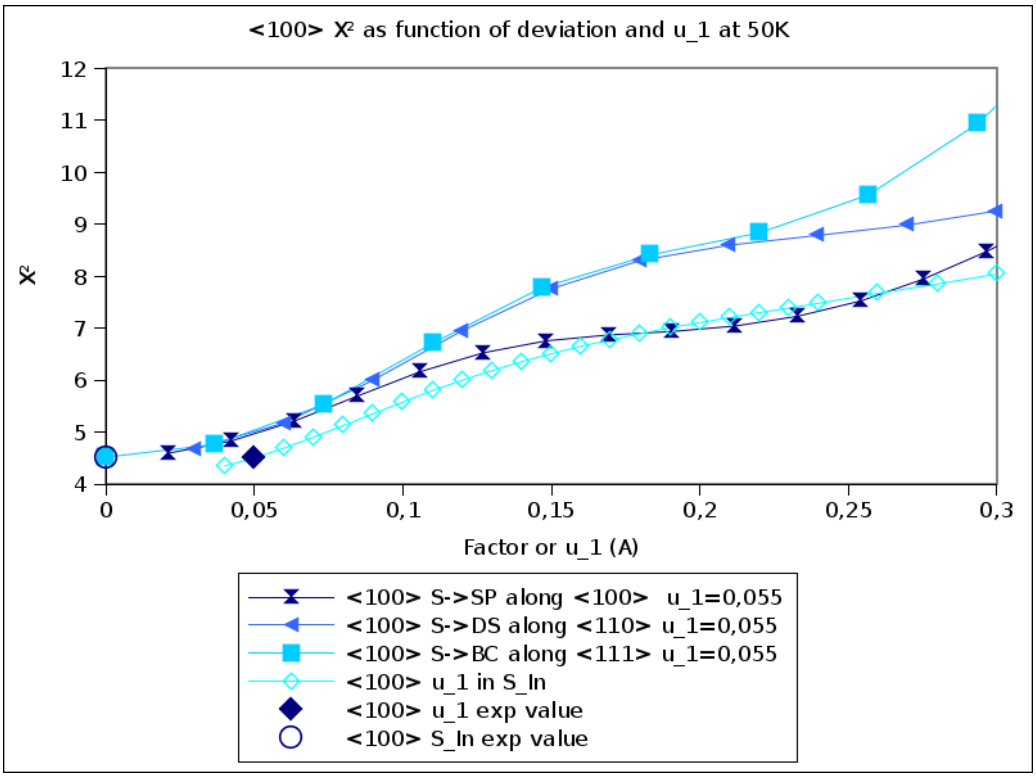

(a) At 100K the χ^2, for the orientation 100, as a function of the u_1 and as a function of the displacement

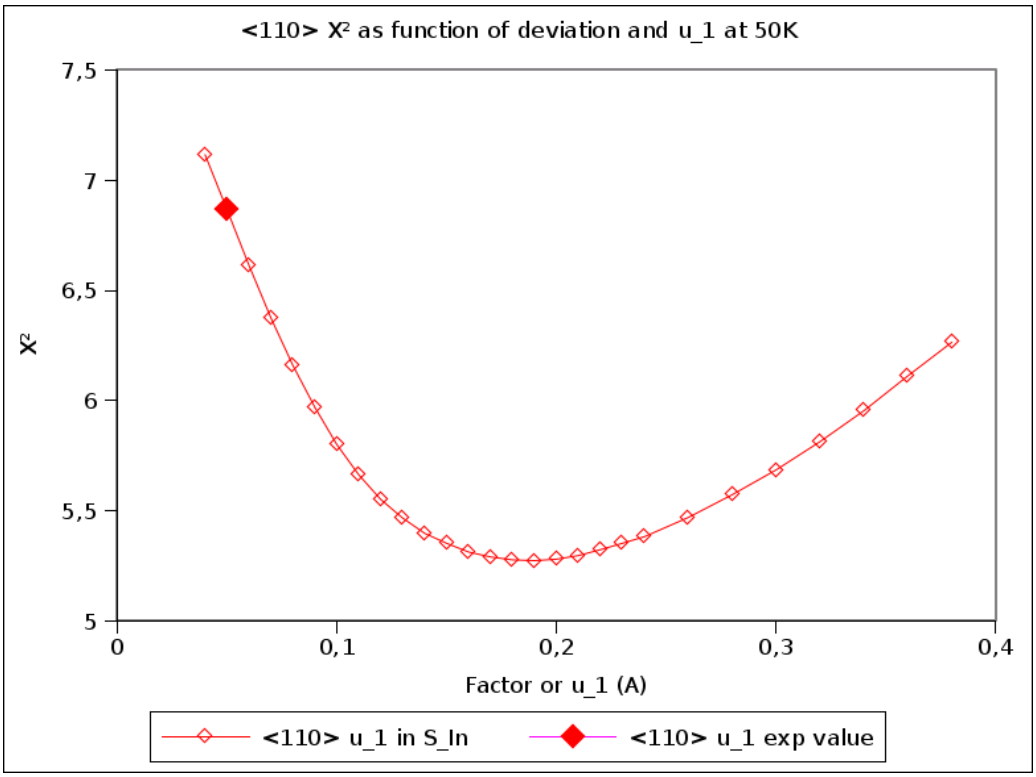

(b) At 100K the χ^2, for the orientation 110, as a function of the u_1 and as a function of the displacement

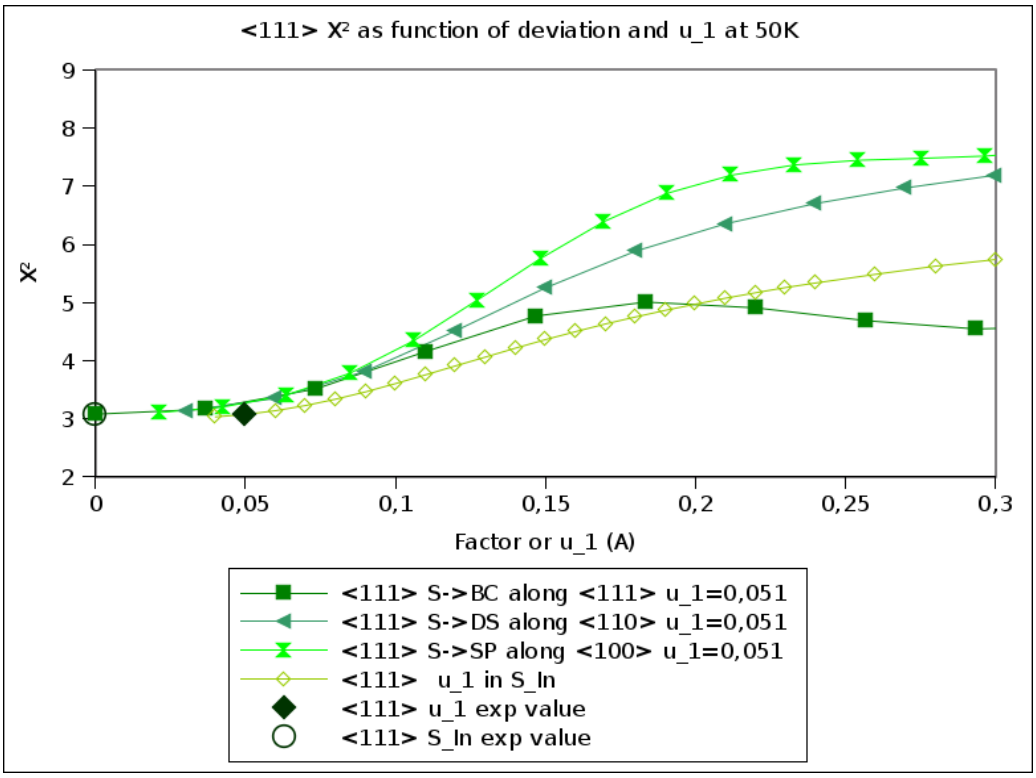

(c) At 100K the χ^2, for the orientation 111, as a function of the u_1 and as a function of the displacement

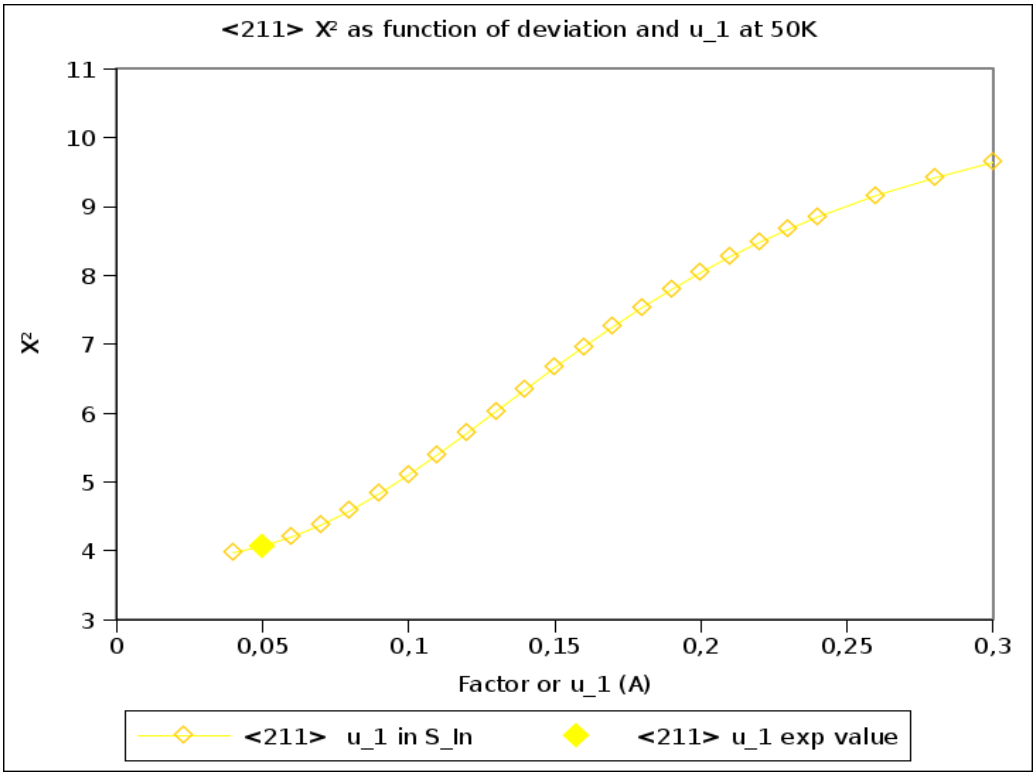

(d) At 100K the χ^2, for the orientation 211, as a function of the u_1 and as a function of the displacement

Figure 4.8: These plots resume the χ^2 obtained as a result of fitting the patterns obtained at 50K, for the four orientations ($< 100 >$, $< 110 >$, $< 111 >$, 211). In each plot the χ^2 is plotted as a function of the static displacement, from the substitutional lattice site, along different directions, for the u_1 values specified in the legend. Also the χ^2 are plotted as a function of the u_1, in the substitutional site.

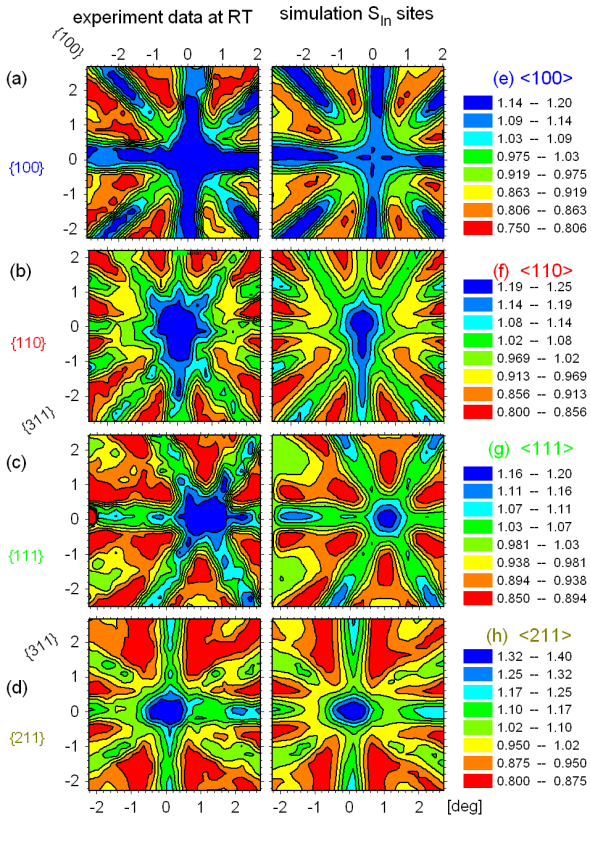

(a) At room temperature the experimental and expected patterns

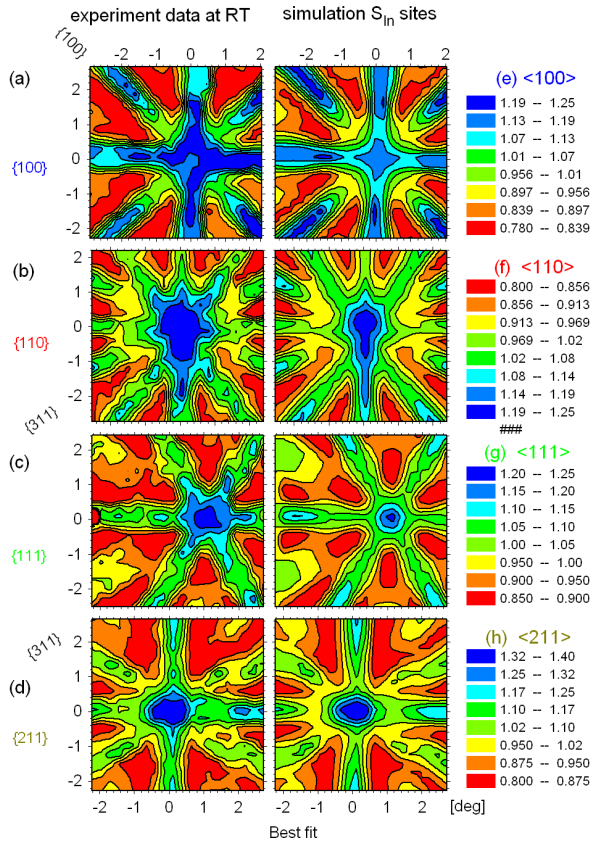

(b) At room temperature the experimental and best fit patterns

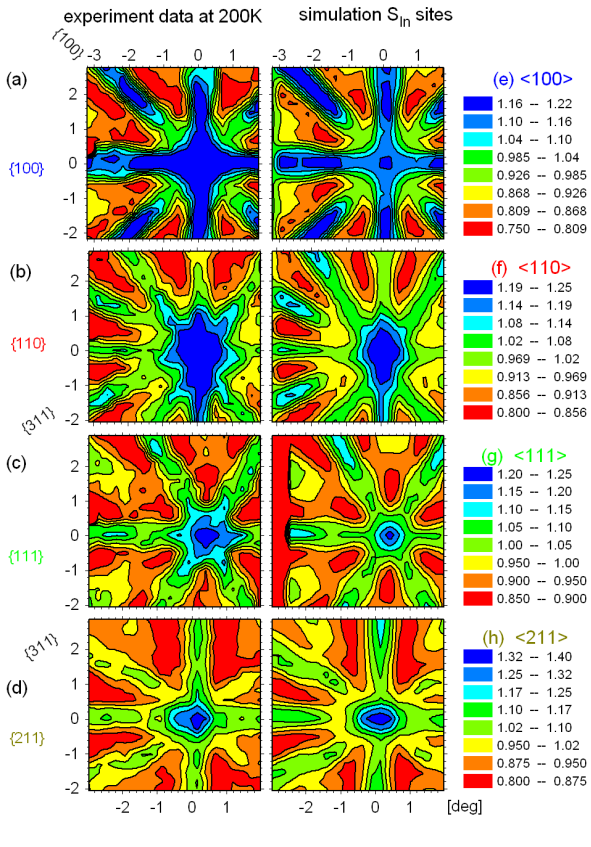

(c) At 200K the experimental and expected patterns

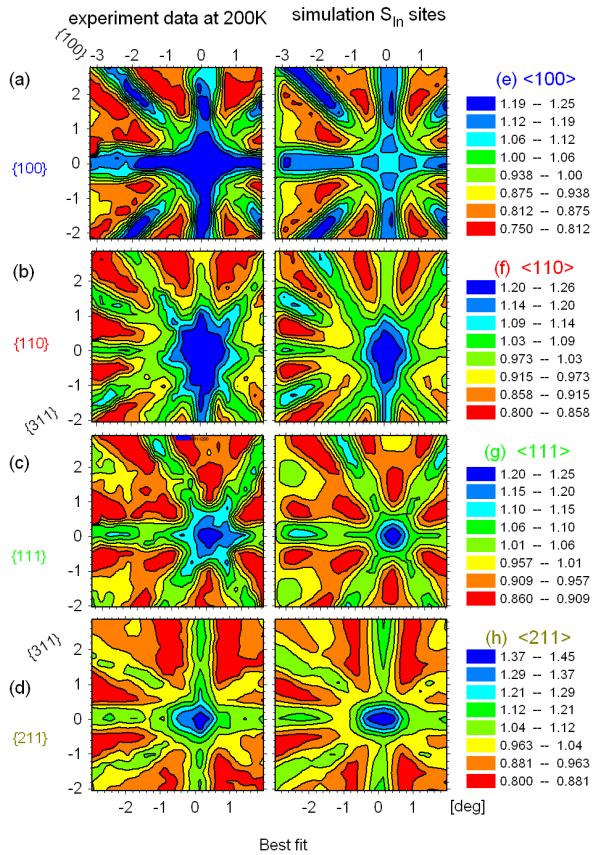

(d) At 200K the experimental and best fit patterns

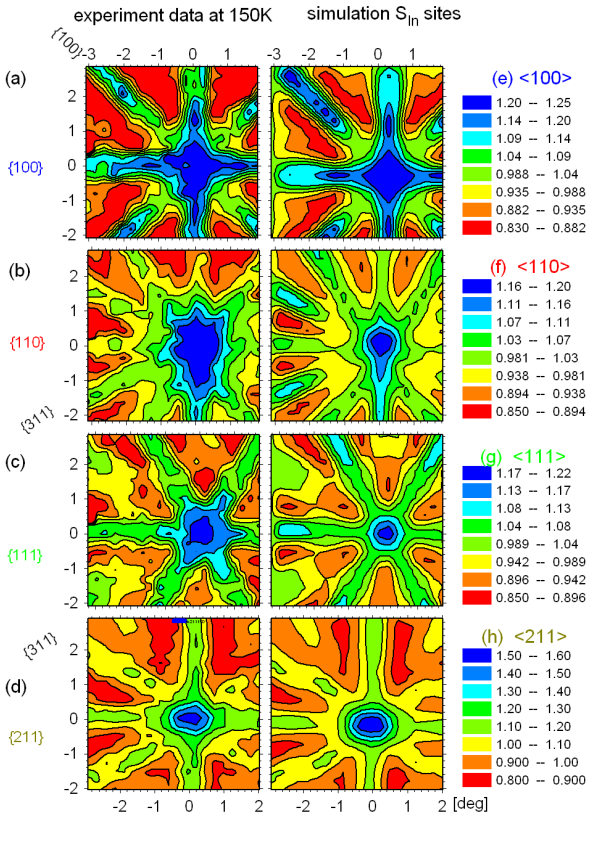

(e) At 150K the experimental and expected patterns

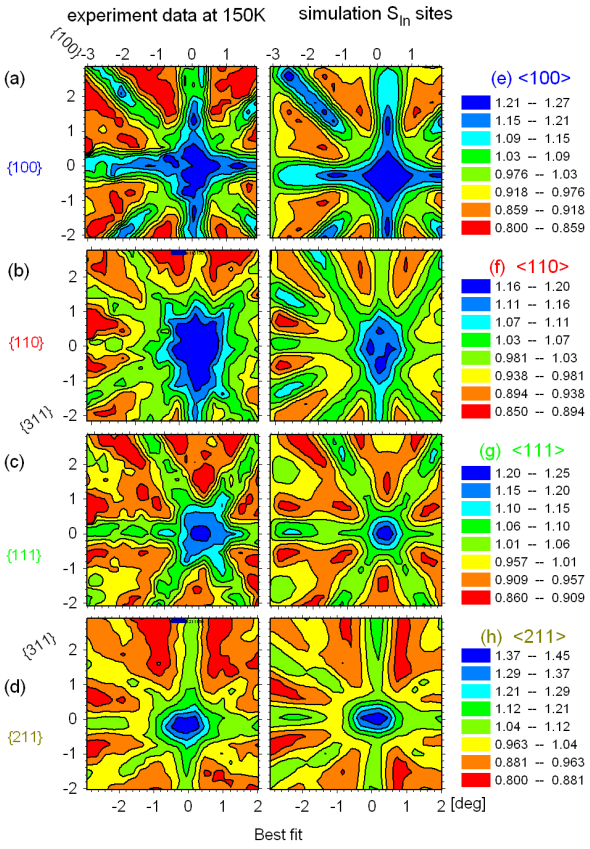

(f) At 150K the experimental and best fit patterns

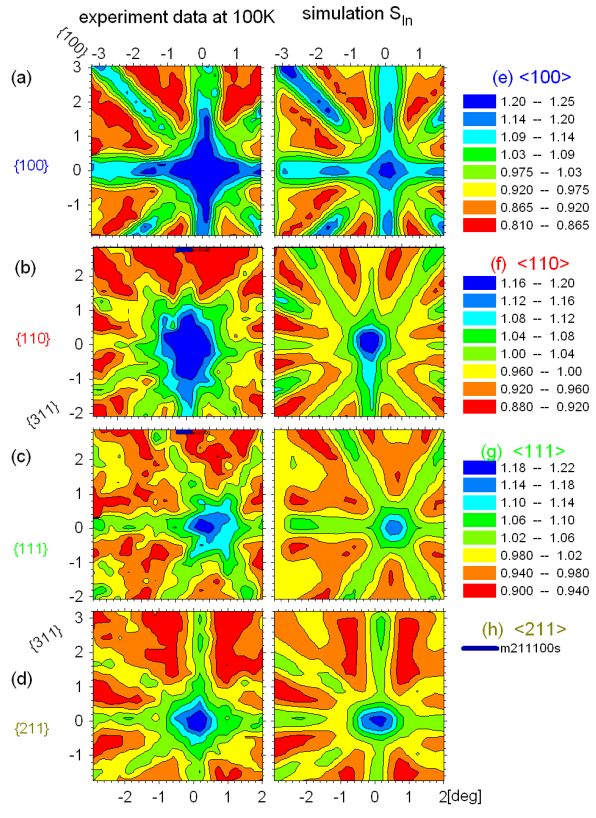

(g) At 100K the experimental and expected patterns

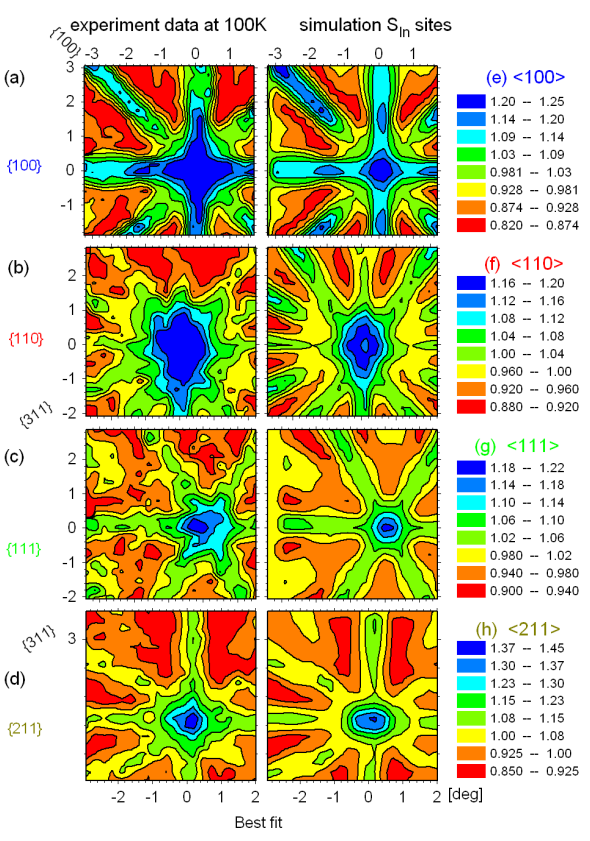

(h) At 100K the experimental and best fit patterns

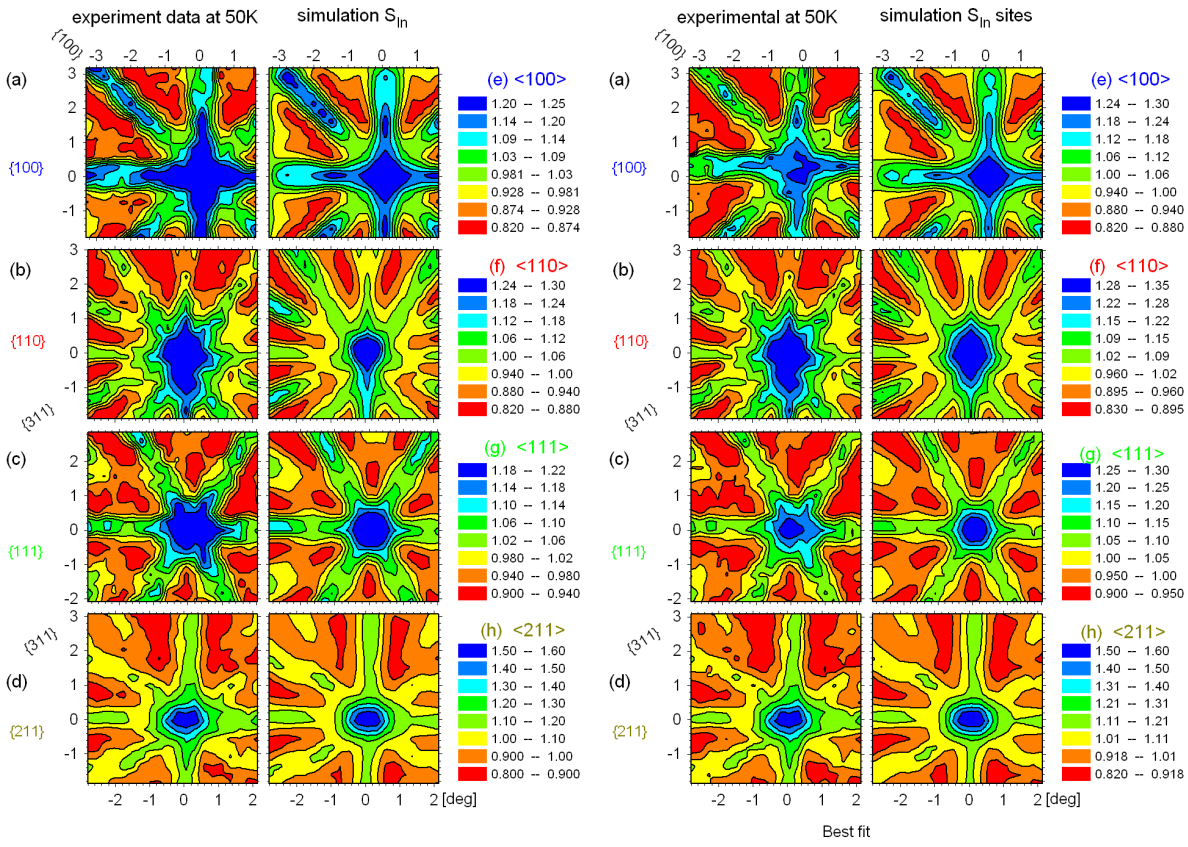

(i) At 50K the experimental and expected patterns

(j) At 50K the experimental and best fit patterns

Figure 4.9: The expected simulated and measured patterns for each orientation and temperature.

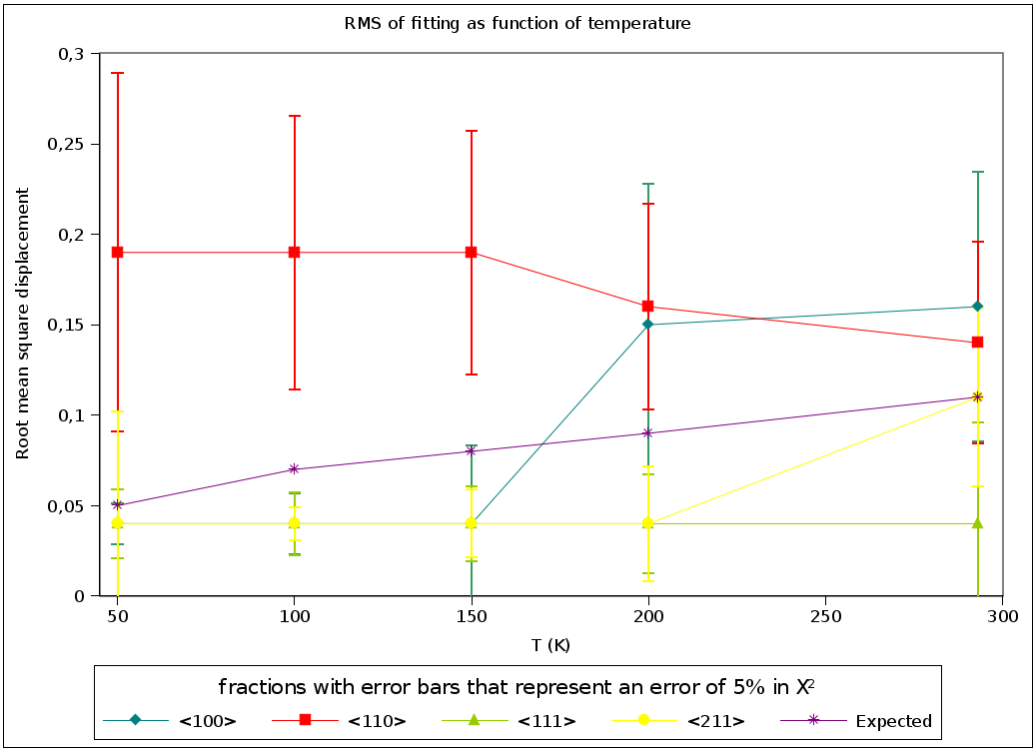

Figure 4.10: The rms as a function of temperature, obtained for all orientations and the expected values, with the error associated with a 5% χ^2 variation.

Fractions of fit

The emission channeling fits, as mentioned earlier, optimize the fraction between the simulated pattern and the random pattern. To the values of the fractions a factor is applied to account for the background correction. The factor is estimated by fitting the peaks as Gaussians in the energy spectrum, as shown in figure 4.11. The values then obtained, for each orientation, as a function of temperature are plotted in the figure 4.12.

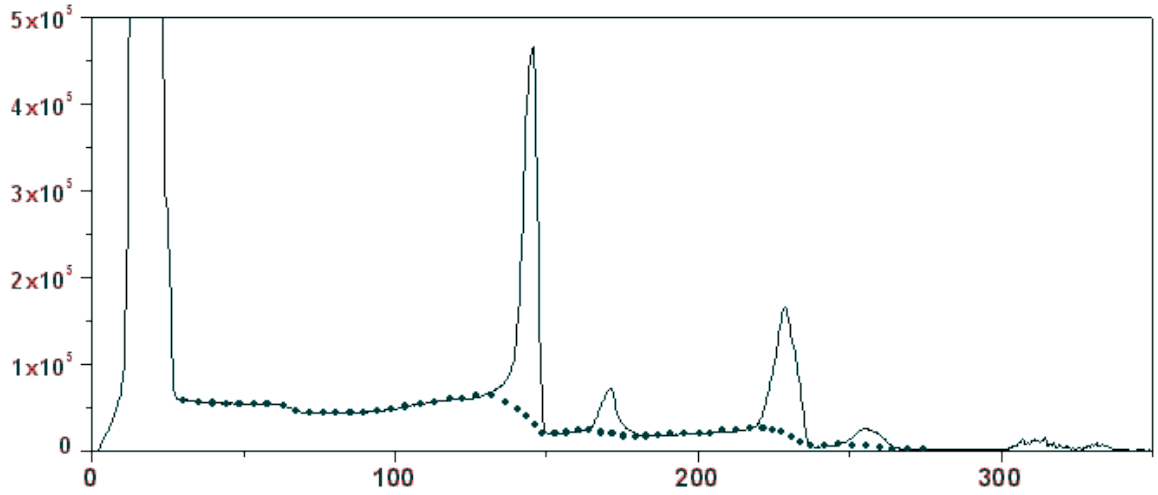

Figure 4.11: The background estimated for the energy spectrum is plotted with the blue dots.

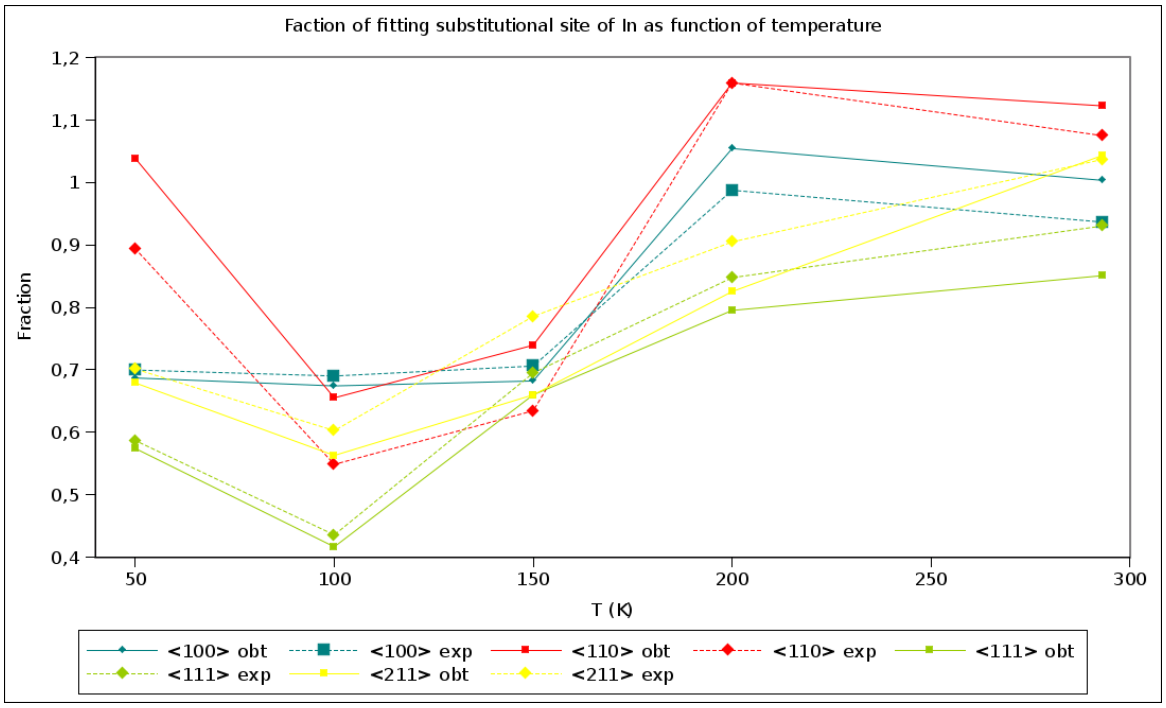

Figure 4.12: The fractions of the fits, with theoretically expected (exp) and the obtained best fit (obt).

There is a clear agreement between the fractions obtained for each orientation, either fitting with the best fit or the expected simulations. It was expected that the fractions would remain the same with the lowering of temperature. The sample had already had an aneealing of 300C and so there was no reason for a displacement of the isotope probes as a function of the measuring temperature (below room temperature). This should result in the same fitting fraction.

Anisotropy

As explained in section 2.3 the fitting procedure includes, the centering, orienting and normalizing of the pattern to optimize the "fit" results, i. e., to get the lowest χ^2. Since the simulation is by its construction process already normalized, the normalization factor is given by the ratio of the simulated and measured patterns. After normalized the difference between the highest and lowest values obtained in the pattern is used as a measure of the anisotropy. In the figure 4.13 the anisotropy values obtained are plotted, together with the anisotropy of the theoretically expected simulations, as a function of temperature.

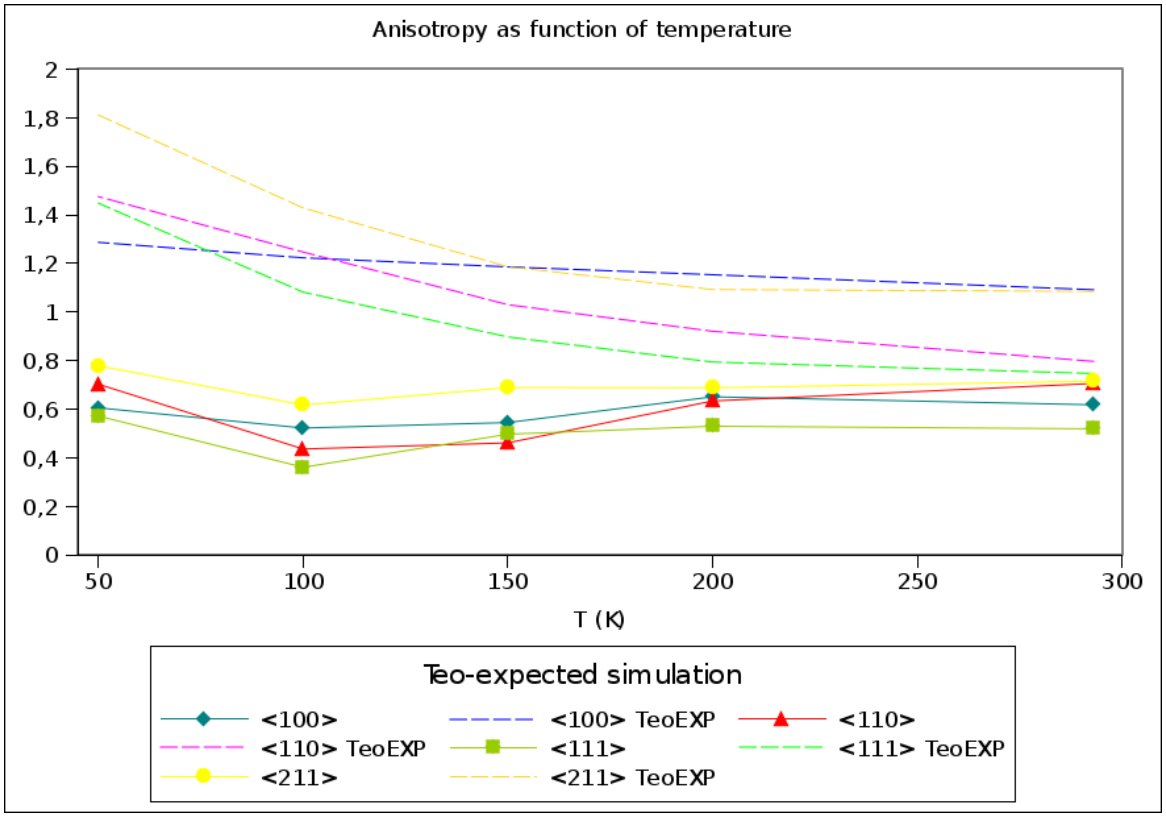

Figure 4.13: The anisotropy of each orientation, theoretically expected (teo.) and experimental. The theoretical data presented in the plot is calculated for different values expected of u_1 for each temperature ($u_1^{RT} = 0.11$, $u_1^{200} = 0.09$, $u_1^{150} = 0.08$, $u_1^{100} = 0.06$, $u_1^{50} = 0.05$Å) and null static displacement (from the substitutional site).

5 Discussion

In this work we have successfully implemented and tested a cooling system for emission channeling experiments to achieve a minimum temperature of $50K$ with stability of $\pm 1K$. For about a week the system worked continuously, from 50K to 200K in steps of 50K, without any problems.

5.1 Fitting results

Fractions

In what concerns the emission channeling results, we have successfully measured the lattice location of the ^{111}In in InP to be mostly located in the substitutional site of In with no static displacement, with a mean value between 58% and 101% fraction at the substitutional site (so between 42% and -1% random). The fitting with more than one lattice site for the same patter did not improve the χ^2, which means that the ^{111}In isotopes are mainly in the substitutional site of In and a small fraction are spread randomly in the lattice. The mean values of fraction are plotted in the figure 5.1. This was expected since the ^{111}In implanted is the same element of the lattice, and so the preferential location of the implanted isotope should only be the substitotional of In. The error of the fit's fractions, for each temperature, was estimated by the standart deviation of the obtained fitting fractions for each orientation and is represented in the figure 5.1 by means of error bars. The fraction values Veriee significantly, but considering the error of the fit's fractions, the variations are mostly within the error.

U_1 and static displacement

Looking at the plots of the fit's χ^2 as a function of u_1 and static displacement, from the figures 4.4, 4.5, 4.6, 4.7 and 4.8, one can see that the fits for lower temperatures are better than those for high temperatures, i.e., the fitting result pattern, a pattern with the difference between the simulation fitted fraction and the experimental pattern, has a higher homogeneity. This implies that the anisotropy of the experimental pattern was better fitted with the simulations. This aspect is strenghned by the fact that the variation curves of χ^2 as a function of the static displacement and vibration u_1 are better defined and smoother, showing more coherent results. Although the χ^2 values obtained are better (closer to 1) this fact could be due to better statistics and so better values of χ^2 can not alone represent a better fitting. Still if one considers the χ^2 relactive error in u_1, which was estimated by the variation of u_1 associated with a 5% variation of the χ^2 (as it was plotted in the figure 4.10), one can already conclude that the error obtained is extremely large and in general decreases with the lowering of temperature. This implies that for the system "compound + probe" studied in this case this method gives a low resolution, in terms of deviation either static or vibration. This could be due to probabilistic, if the statistics are not enough the experimental data is build into a less defined pattern and so the fitting can not be as accurate. Still it is of our conviction that the low resolution obtained is due to the large vibrations of the matrix lattices which result in higher dechanneling. Furthermore the results obtained for the r.m.s. displacement in the $< 110 >$ orientation are clearly of higher disagreement with what was expected than the results obtained for the other orientations. Due to the crystal's configuration and the orientation of the surface,

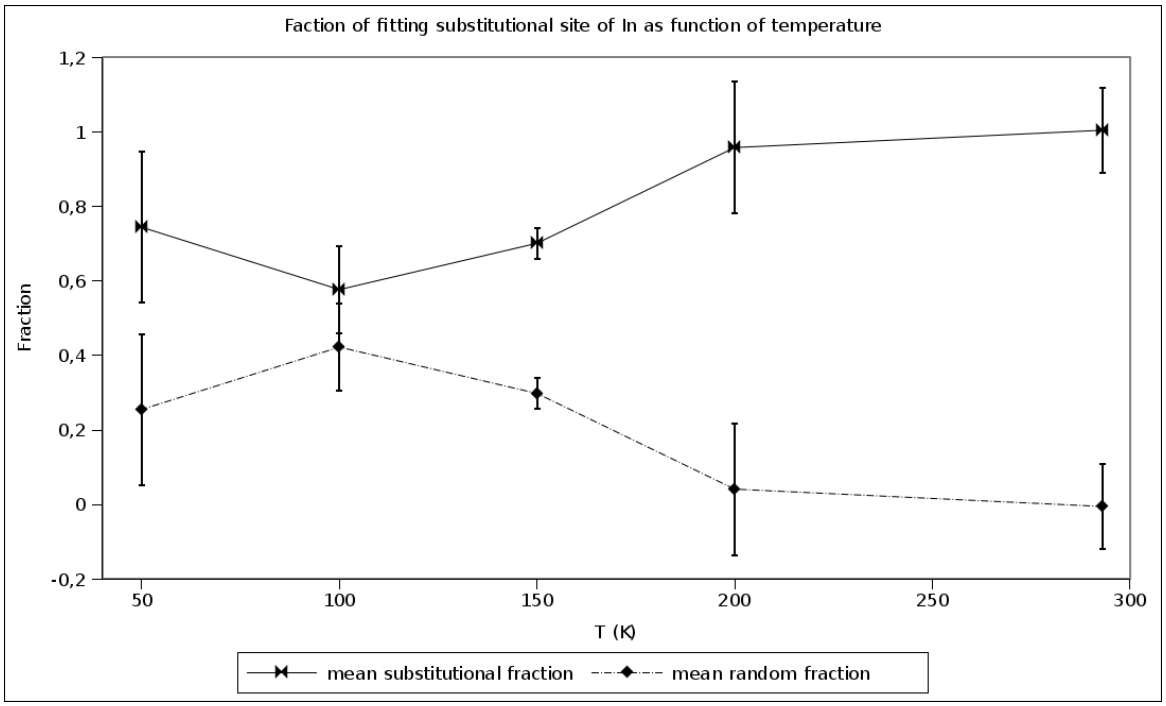

Figure 5.1: The mean fractions of the fits, obtained with the theoretically expected simulation patterns. The error bars represented are estimate from the standart deviation of the obtained fractions for each orientation.

the measurements for this orientation are particularly sensitive to the dechanneling effect and so this can be a sign that in fact the dechanneling calculations did not provide sufficiently accurate predictions for the system in study.

Anisotropy

Looking at the anisotropy values plotted in the figure 4.13, the values of the experimental patterns did not grow with the lowering of temperature, as expected according to the anisotropy of the simulated patterns (also plotted in the figure). The relatively worst results obtained for higher temperatures, as it was mentioned earlier, are a possible reason for the discrepancies between the behavior of the experiemntal and theoretical anisotropies as a function of temperature.

Dechanneling

Alltogether there was insufficient knowledge of the compound's r.m.s. displacement for temperatures bellow the room temperature. In high temperatures the study suggest that there is some misscalculation in the simulations, so it was tried to fit the room temperature (293K) experimental patterns with the 50k simulation's library and these fits gave better results, than when using the room temperature simulation library. The differences between simulations for room temperature and 50K are mostly due to the decrease in dechanneling which is caused by the decrease of the r.m.s. displacement of the lattice at 50K, to a lesser extent the change in r.m.s. displacement also influences the thermally average continuum potential. For this reason, and since the results obtained for the $< 110 >$ orientation are the most severely influenced, it is thought that we might have reached a limit of the dechanneling model. In order to test the influence of dechanneling one must repeat the experiments using a lower implantation energy. This would decrease the depth at which the probes are implanted, thus reducing the traveling distance of the EC electrons in the crystal and consequently decreasing the dechanneling effect.

The implantation is estimated to cause a high density of defects, being the recovery of channeling effect with the annealing temperature still unknown with precision. The measurements of ^{111}In in InP EC as a function of the annealing temperature have already been taken, but the analysis waits to be done. Once this study is finished for an element that is a lattice constituent, the study of impurities implanted in InP can start in a more consistent way. The recovery of the lattice with annealing regarding impurities can then be studied along with the influence of the annealing temperature by study of emission channeling patterns.

5.2 contamination

In the analysis of the patterns obtained (figure 4.2) the fact that the first showed higher electron intensity on the right side, than on the left side, of the pattern came to light. As was previously mentioned, the events registered in the spectral range 300-400 keV (figure 4.1) result from electrons that have deposited energies at or above these values in the detector, but where the pulses height of the signals is saturated by the preamplifiers

The detector's signal comes from four chips, located in the four edges of the detector. Each chip collects the information regarding a triangular part of the detector's surface, with the base of the isosceles triangle facing the chip and pointing the center.

The figure 5.2 shows the pattern created for the energy window of $[275, 1000]\, eV$. The pattern is divided

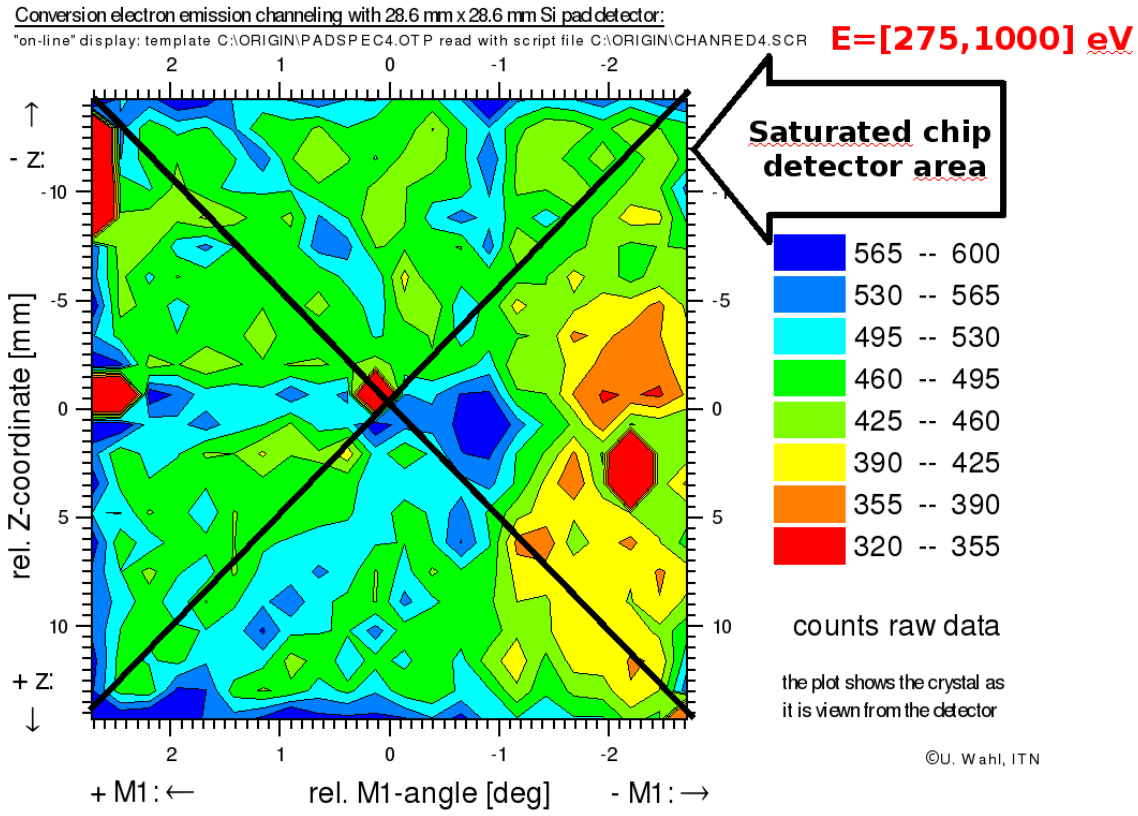

Figure 5.2: The detected electron intensity in the energy window of $[275, 1000]\, eV$ for the first measurement shows lack of symmetry. This pattern is representative of the saturation heterogeneity.

to illustrate the surface of the detector connected to each chip. As it is easy to see the right side of the pattern has about 15% lower intensity of counts than the others. The fact that there is a channeling effect measured shows that the events in this region of the spectrum result from electrons emitted by a radio isotope which was implanted together with ^{111}In into the sample.

Finally we studied the origin of the high energy electron contamination considering that for the neutron rich side of the decay chain of mass 111 (figure 5.3) all the isotopes decay by β^-. Looking at the spectrum of energies for β^- decays is shown in figure 5.4 and considering the mean energy of the ^{111}Ag, β^- of $355keV$, ^{111}Ag was considerably a good candidate for the contamination.

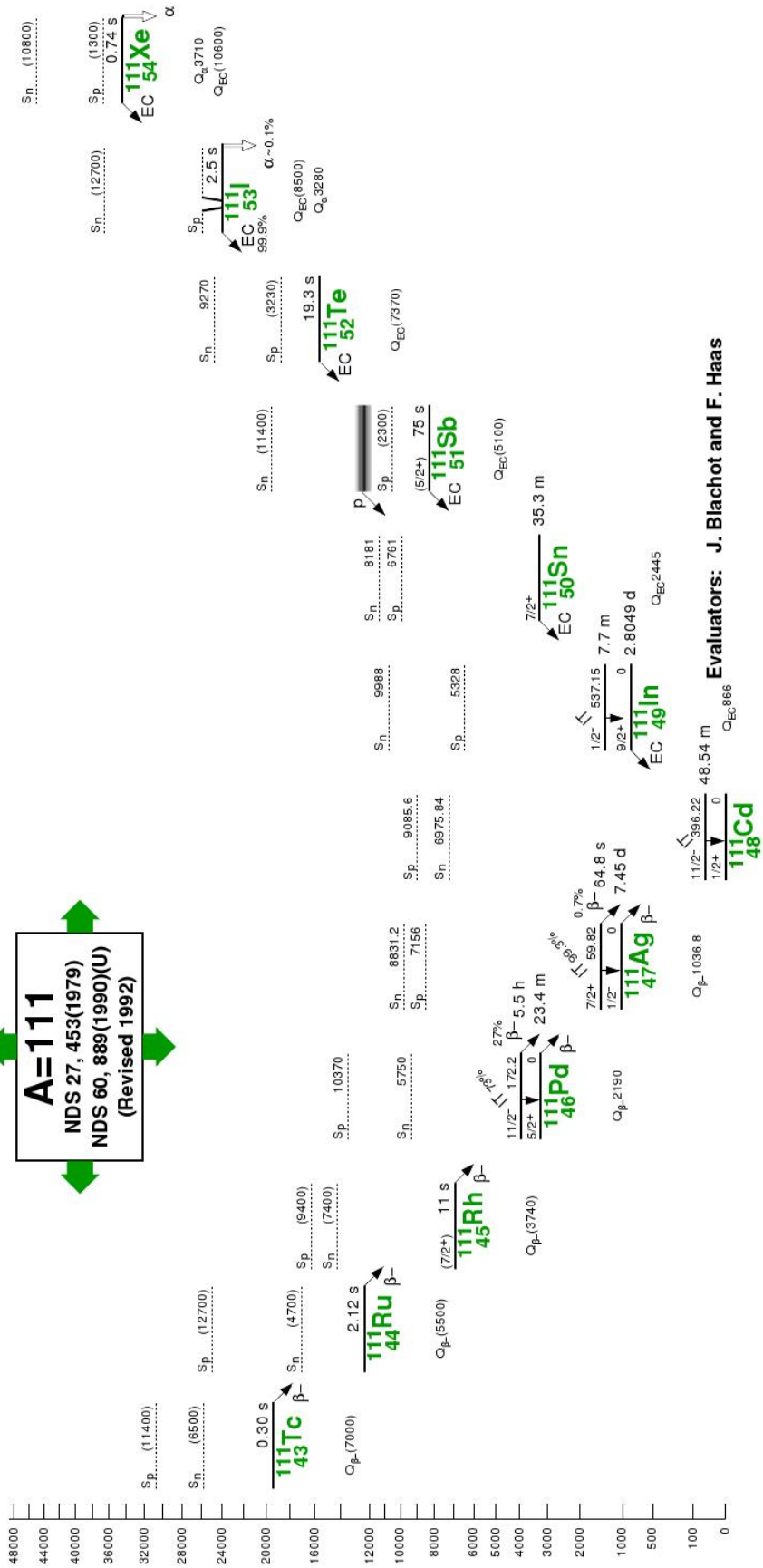

Figure 5.3: The $^{111}Isotopes$ decay to ^{111}Cd [39]

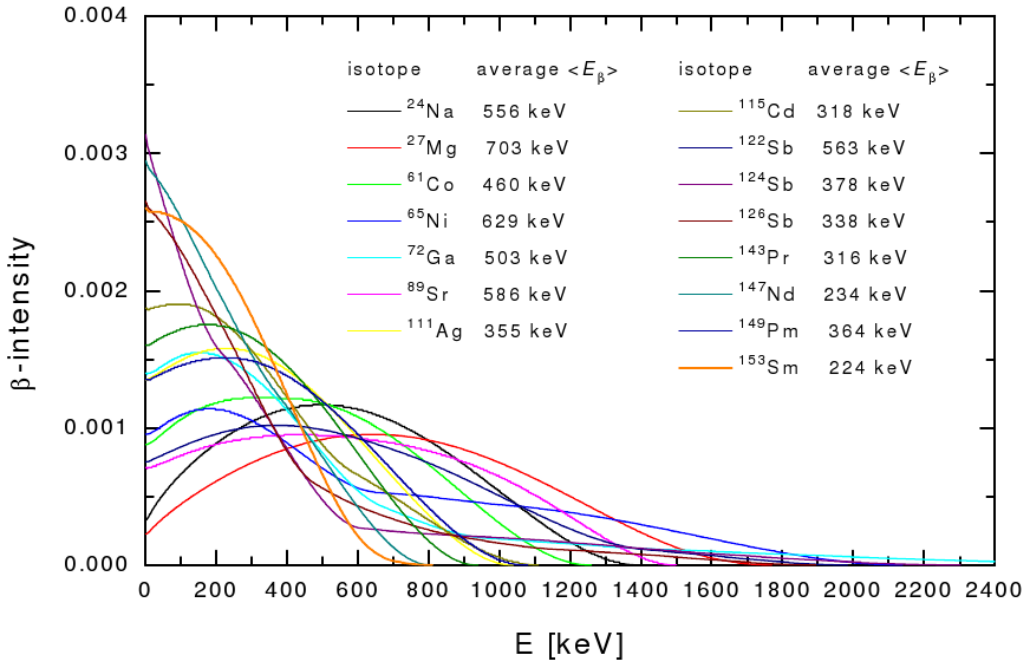

Figure 5.4: Beta decay energy spectra [1].

The half-life of the contaminating isotope was estimated by comparing the electron intensity, for energies around the $314.4keV$ peak, in the energy spectrum β^- in the four first measurement patterns and for the next four measurement patterns and found to be ~ 3.3 hours.

However the half-life of ^{111}Ag, shown in the figure 5.3, is $7.45days$ which is much larger than the ^{111}In half-life, and since this contamination has a very low intensity these decays would not be relevant in the measurements of the ^{111}In patterns.

Comparing this value to the half lives of possible contaminants in the isobaric chain shown in figure 5.3, we conclude that there is a good match to $^{111m}Pd(5.4h)$. This isometric state has 27% branching ratio for β^- decay to $^{111}Ag(7.45d)$, while 73% de-excite by gamma emission into the ground state $^{111}Pd(23.4h)$, which then also decays by β^- emission into ^{111}Ag. The resulting electron spectrum consists of a superposition of 27% β^- from ^{111m}Pd and 73% of ^{111}Pd and is shown in figure 5.6.

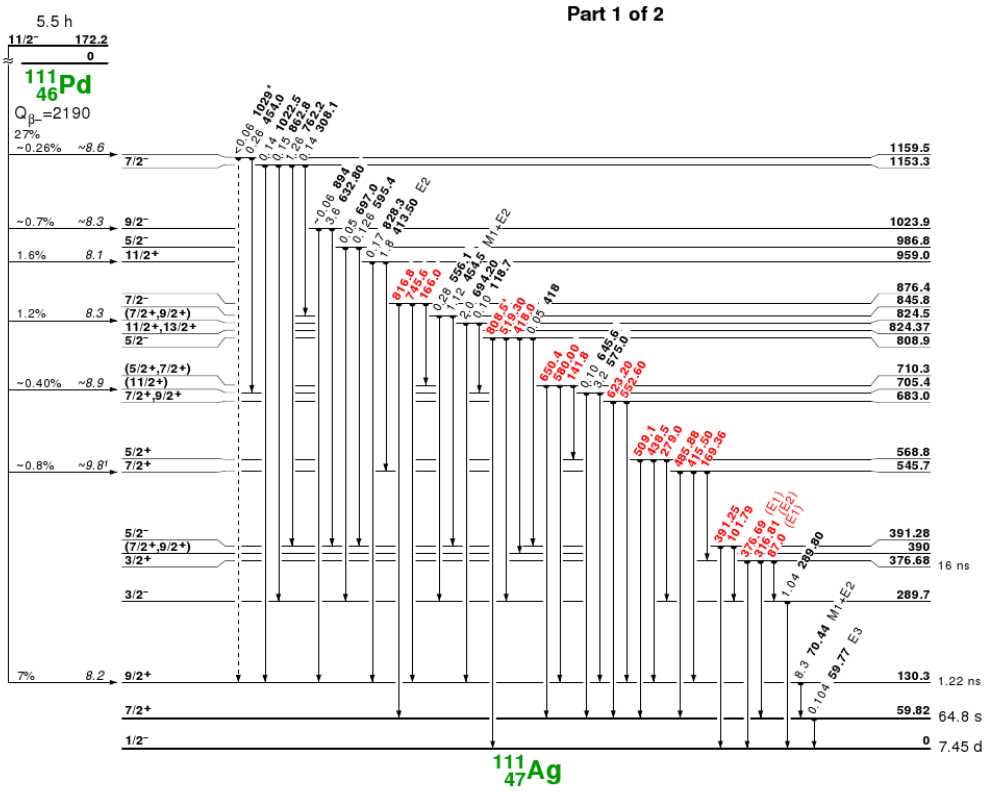

(a)

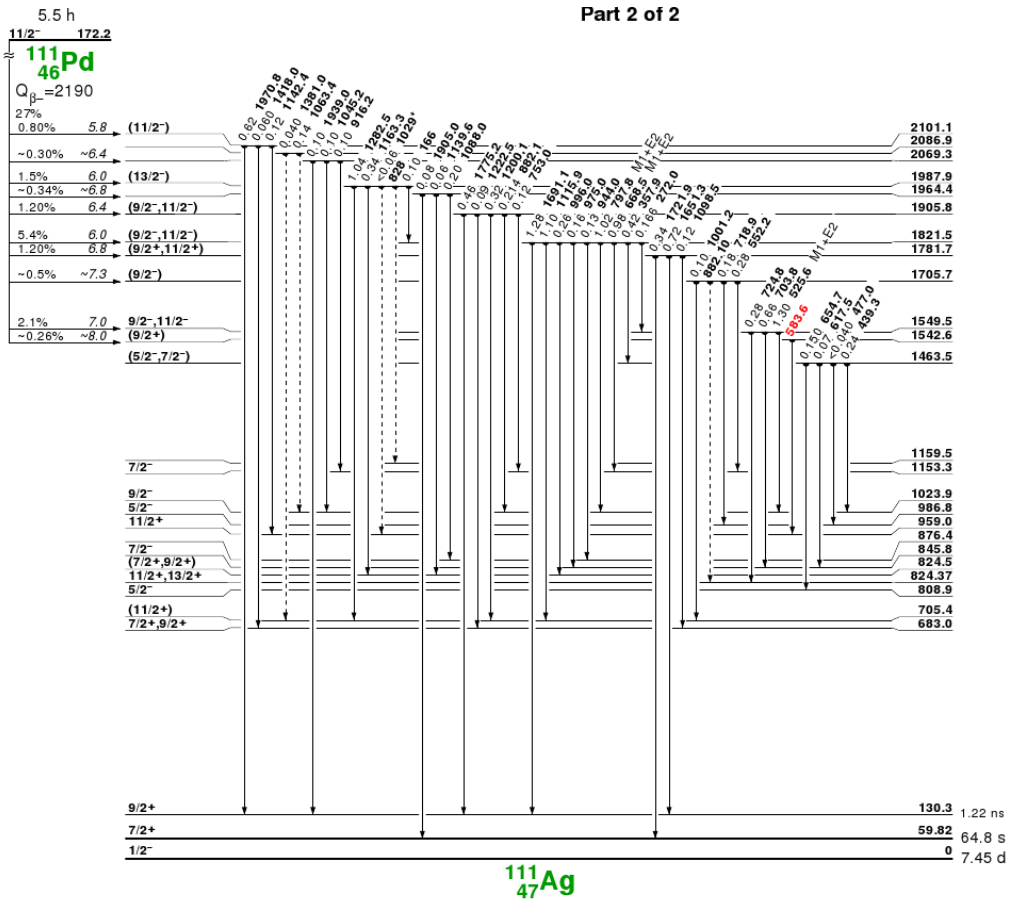

(b)

Figure 5.5: The decay of ^{111}Pd and ^{111}Ag[39].

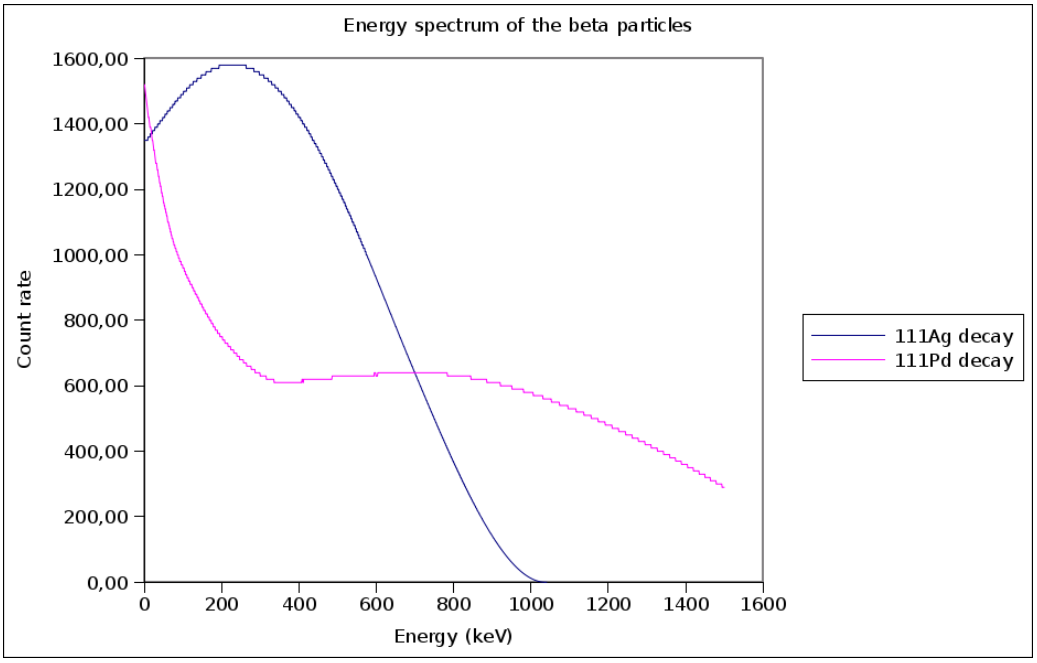

Figure 5.6: The decay of ^{111}Pd[39] and ^{111}Ag[1] energy spectrum.

This contamination is roughly estimated to be 1% of the implanted ions. Considering an activity of $15.7Hz$ at the time of implantation. Although the identification of the contamination as ^{111}Pd is quite clear from the measured half life, in discussions with the ISOLDE beam engineers it was assured that Pd is not

ionized by the surface ionization (method used), which is rather puzzling.

The contamination should influence mostly the first measurements taken. In table 4.1 the measurements start time is shown, the first measurements being the room temperature ones. This may help explain some difficulties in fitting those patterns, but it is not considered to be significant enough to justify.

5.3 Simulations

The potential calculated is shown in figure 2.4. The most populated states are illustrated in the figures 5.7a and 5.7b. In the table 5.1 the potential states population and mean free path from the figures are summarized.

Considering the electron flux density of states and the depth profile of the implantation, as shown in the

Potential States			
T (K)	state	population	free mean path ($\dot{A}$)
293	1	17.7%	64
	2	49.2%	595
	5	32.7%	493
50	1	13.3%	95
	2	48.2%	758
	5	38.2%	695

Table 5.1: Potential states

lower right plot of the figures 5.7a and 5.7b, one can see that the most populated states for the room temperature measurements have relatively low flux densities at S_{In} sites already at a depth of only $150\mathring{A}$. On the other hand as a consequence of the less pronounced dechanneling and the associated longer mean free paths at 50K the flux densities for the $50K$ are much higher. This means that at room temperature it is harder to obtain clear emission channeling patterns. This may help justify the fact that the $50K$ patterns were better fitted than those at high temperature.

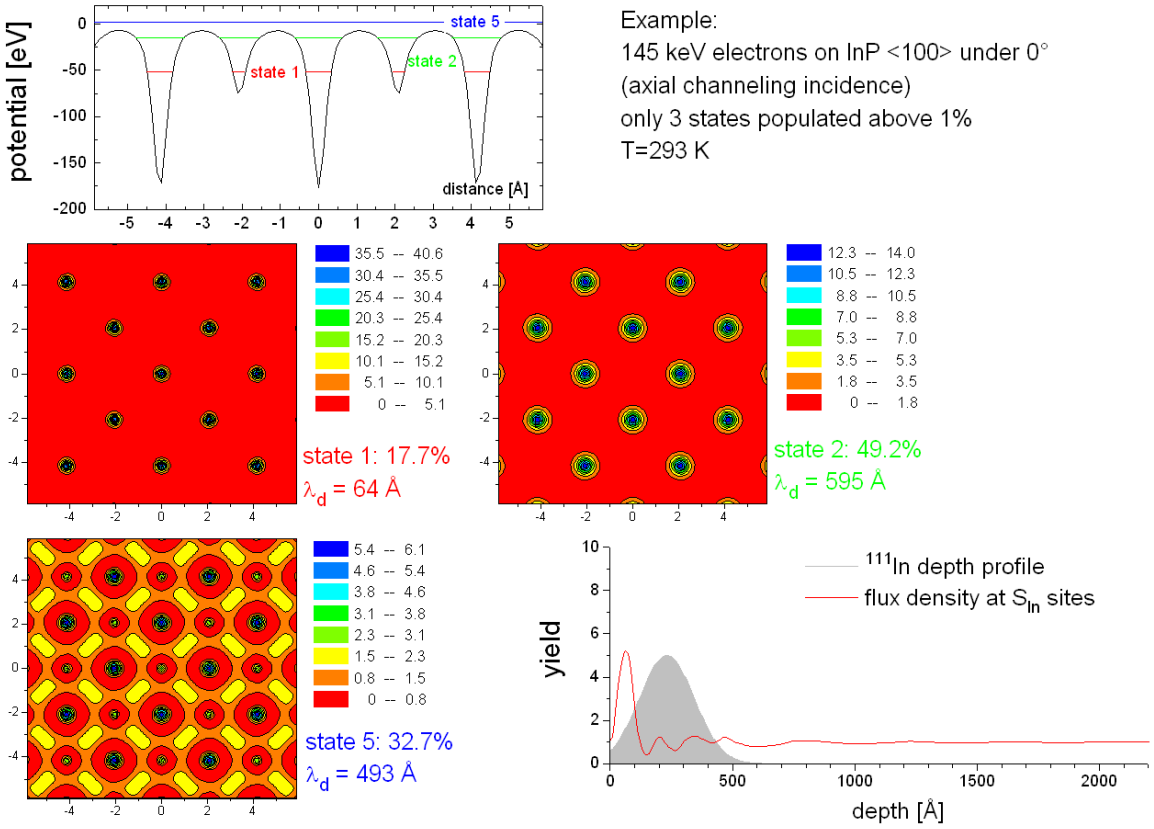

(a) At room T

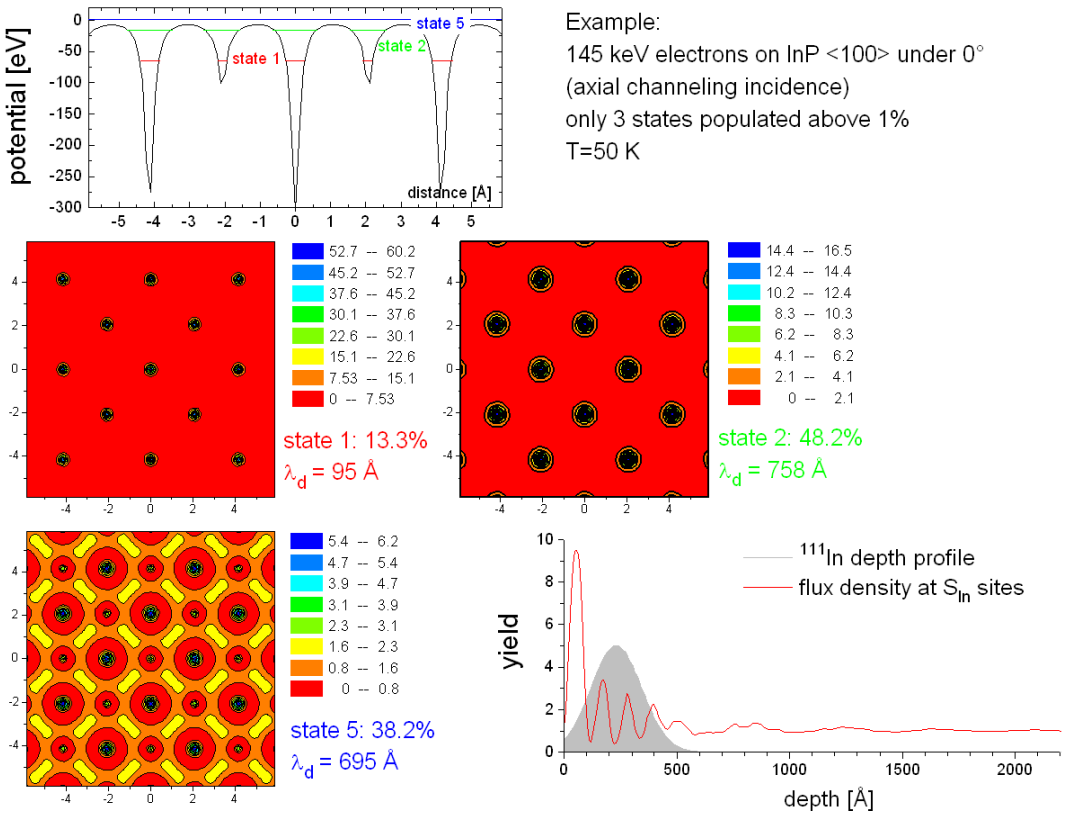

(b) At 50K

Figure 5.7: The most populated states in the $< 100 >$ orientation are represented in the potential plot. Underneath the probability density of each state in the (100) plane is plotted, with the respective population percentage in the right. On the bottom right the plot shows the depth profile of the flux density and of the implantation distribution.

5.4 Conclusions

The conclusions of this work can be summarized as follows:

- The cooling station developed and implemented by us worked as expected down to 50K and provided a relatively good temperature stabilization.
- Following implantion of ^{111}In in InP, the ^{111}In tends to go to the substitutional site of In, as expected.
- The lower the temperature the measurements are made the better the fitting results are, hence revealing a better matching of the theoretical models.
- During the fitting we faced some difficulties that seem to be associated with limitations for simulating dechanneling in such lattice with heavy elements.
- There are no r.m.s. displacement measured values for the available for InP at low temperatures and the extrapolation according to the Debye model does not seem to give good results for this technique, although the r.m.s. displacement variations as a function of temperature expected are small.
- There was a small problem of contamination during the first measurements and the energy and half-life pointed to 1% ^{111}Pd, we were left with an unknown contamination, fortunately not relevant enough to invalidate the results obtained.

As a complementary study to this work there are the following propositions:

- To test the dechanneling model, we can proceed with the ^{111}In EC study in InP using a lower implantation energy.
- To finalize analysis of the ^{111}In implant in InP as a function of the annealing temperature. It is expected to provide further background for latter studies of implantion in InP.
- To proceed with emission channeling studies of low temperatures, either by implanting at low temperatures and the follow of the lattice sites when raising the temperature up to RT.

Appendices

Appendix A
Data found in the literature for the r.m.s. vibration amplitudes in InP

The masses used were: M(In)=114.82 amu; M(P)=30.9738 amu; Average mass: 72.8969 amu. And since some of the data were in B the formula used was:

$$B = 8\pi^2 U = 8\pi^2 u_1^2 \tag{A.1}$$

Method:	neutron diffraction	
TM=RT=295 K	U(In)=0.0116(6) $\dot{A}^2$	u_1(In) = 0.1077(30) $\dot{A}$
TM=RT=295 K	U(P)=0.0099(5) $\dot{A}^2$	u_1(P) = 0.0995(30) $\dot{A}$
Derived Debye temperatures :	TD(In)	180.5 K
	TD(P)	382.7K
	TD(InP)	238(11) K

Table A.1: Literature data on rms displacement by [28]

Method:	X-ray single crystal diffraction	
Remark:	Ref. 27+28 in [28]	
TM=RT	U(In)=0.0098 $\dot{A}^2$	u_1(In) = 0.0990 $\dot{A}$
TM=RT	U(P)=0.0137 $\dot{A}^2$	u_1(P) = 0.117 $\dot{A}$
Derived Debye temperatures :	TD(In)	196.5 K
	TD(P)	323.4K
	TD(InP)	229(18) K

Table A.2: Literature data on rms displacement by [27]

Method:	X-ray powder diffraction	
Remark:	Ref. 31 in [28]	
TM=RT	U(In)=0.0164 $\dot{A}^2$	u_1(In) = 0.1281 $\dot{A}$
TM=RT	U(P)=0.0190 $\dot{A}^2$	u_1(P) = 0.1378 $\dot{A}$
Derived Debye temperatures :	TD(In)	151.5 K
	TD(P)	273.3K
	TD(InP)	184(6) K

Table A.3: Literature data on rms displacement by [26]

Method:	X-ray spherical single crystal diffraction	
TM=RT=300 K	B(In) = 0.903(4) $\dot{A}^2$	u_1(In) = 0.1069(3) $\dot{A}$
TM=RT=300 K	B(P) = 1.147(80) $\dot{A}^2$	u_1(P) = 0.1205(40) $\dot{A}$
Derived Debye temperatures :	TD(In)	183.4 K
	TD(P)	316.3K
	TD(InP)	218(12) K

Table A.4: Literature data on rms displacement by [25]

Method:	calculation of limiting value of TD from phonon density of states	
Debye temperatures :	TD(InP)	456 K
	TD(In)	363.3 K
	TD(P)	699.6 K
Derived u_1:	T=RT=295 K	u_1(In) = 0.0543 $\dot{A}$
	T=RT=295 K	u_1(P) = 0.0570 $\dot{A}$

Table A.5: Literature data on rms displacement by [24]

Method:	calculation of TD from elastic constants	
Debye temperatures :	TD(InP)	320.5 K
	TD(In)	255.4 K
	TD(P)	491.7 K
Derived u_1:	T=RT=295 K	u_1(In) = 0.0765 $\dot{A}$
	T=RT=295 K	u_1(P) = 0.0785 $\dot{A}$

Table A.6: Literature data on rms displacement by [23]

Method:	lattice dynamical calculations of u_1(T)	
T=250 K	u_1(In) = 0.126 $\dot{A}$	u_1(P) = 0.128 $\dot{A}$
T=300 K	u_1(In) = 0.138 $\dot{A}$	u_1(P) = 0.139 $\dot{A}$
T=380 K	u_1(In) = 0.156 $\dot{A}$	u_1(P) = 0.157 $\dot{A}$
T=450 K	u_1(In) = 0.170 $\dot{A}$	u_1(P) = 0.172 $\dot{A}$
T=800 K	u_1(In) = 0.183 $\dot{A}$	u_1(P) = 0.185 $\dot{A}$
T=250 K	u_1(In) = 0.226 $\dot{A}$	u_1(P) = 0.227 $\dot{A}$
T=1058 K	u_1(In) = 0.259 $\dot{A}$	u_1(P) = 0.260 $\dot{A}$

Table A.7: Literature data on rms displacement by [22]

Method:	calculations of u_1(T) from eight-parameter bond-bending force model	
T=50 K	u_1(In) = 0.0626 $\dot{A}$	u_1(P) = 0.0627 $\dot{A}$
T=100 K	u_1(In) = 0.0843 $\dot{A}$	u_1(P) = 0.0844 $\dot{A}$
T=200 K	u_1(In) = 0.1174 $\dot{A}$	u_1(P) = 0.1175 $\dot{A}$
T=300 K	u_1(In) = 0.1433 $\dot{A}$	u_1(P) = 0.1434 $\dot{A}$
T=400 K	u_1(In) = 0.1653 $\dot{A}$	u_1(P) = 0.1656 $\dot{A}$
T=500 K	u_1(In) = 0.1847 $\dot{A}$	u_1(P) = 0.1849 $\dot{A}$
T=600 K	u_1(In) = 0.2023 $\dot{A}$	u_1(P) = 0.2024 $\dot{A}$
T=700 K	u_1(In) = 0.2185 $\dot{A}$	u_1(P) = 0.2187 $\dot{A}$
T=800 K	u_1(In) = 0.2335 $\dot{A}$	u_1(P) = 0.2337 $\dot{A}$
T=900 K	u_1(In) = 0.2447 $\dot{A}$	u_1(P) = 0.2479 $\dot{A}$
T=1232 K	u_1(In) = 0.2899 $\dot{A}$	u_1(P) = 0.2900 $\dot{A}$

Table A.8: Literature data on rms displacement by [21]

Method:	calculations of u_1(T) from eigenfrequencies and eigenvectors of modified rigid ion model	
T=10 K	u_1(In) = 0.0632 $\dot{A}$	u_1(P) = 0.0819 $\dot{A}$
T=30 K	u_1(In) = 0.0648 $\dot{A}$	u_1(P) = 0.0831 $\dot{A}$
T=50 K	u_1(In) = 0.0693 $\dot{A}$	u_1(P) = 0.0860 $\dot{A}$
T=70 K	u_1(In) = 0.0755 $\dot{A}$	u_1(P) = 0.0900 $\dot{A}$
T=100 K	u_1(In) = 0.0849 $\dot{A}$	u_1(P) = 0.0964 $\dot{A}$
T=150 K	u_1(In) = 0.1005 $\dot{A}$	u_1(P) = 0.1082 $\dot{A}$
T=200 K	u_1(In) = 0.1140 $\dot{A}$	u_1(P) = 0.1196 $\dot{A}$
T=250 K	u_1(In) = 0.1265 $\dot{A}$	u_1(P) = 0.1308 $\dot{A}$
T=300 K	u_1(In) = 0.1382 $\dot{A}$	u_1(P) = 0.1414 $\dot{A}$
T=600 K	u_1(In) = 0.1942 $\dot{A}$	u_1(P) = 0.1952 $\dot{A}$
T=1343 K	u_1(In) = 0.2898 $\dot{A}$	u_1(P) = 0.2902 $\dot{A}$

Table A.9: Literature data on rms displacement by [20]

Appendix B
Procedure for RBS/C InP characterization

B.1 Experiment

- date: 05/03/2008
- beam: Van der Graaff - ITN
- sample: 213
- composition: InP semi-insulating Fe-doped
- structure: zinc blende
- sample size: about $1 \times 1cm^2$ thickness $0.3mm$
- beamspot size$\approx 1mm \times 1mm$

B.2 Procedure

To orient the sample once mounted into the goniometer, one must collect data as function of the θ and ϕ angles. Afterwards one searches for the minima of count rate of the backscattered particles, with energies at a region of the energy spectrum that corresponds to the scattering of one of the heaviest elements constituent of the material, in this case indium. By finding clear intensity minimums for various values of θ and ϕ, the planar location is identified, and from their interception the axis is found.

This way, the first data collected was:

1. - while keeping the polar angle θ at a fixed value a big number of ϕ was scanned to find any lattice plane. A minimum was found in $\phi = 216$.
2. - through scans of different θ for the found ϕ (216). - search for the plane.
3. - for different ϕ , we search for other existing planes.
4. - looking for further encounters with the same planes so we could draw the lines of them, predicting the center of the scattering planes (figure 3.7a).

The results were plotted in 3.7a. Since the distance (difference of θ) between the minima found was small, whitch implies small accuracy to find the axis, measures in the opposite direction (opposite values of ϕ) were taken.
The new values were added and corrected lines were now drawn, to represent two planes, in figure B.1.

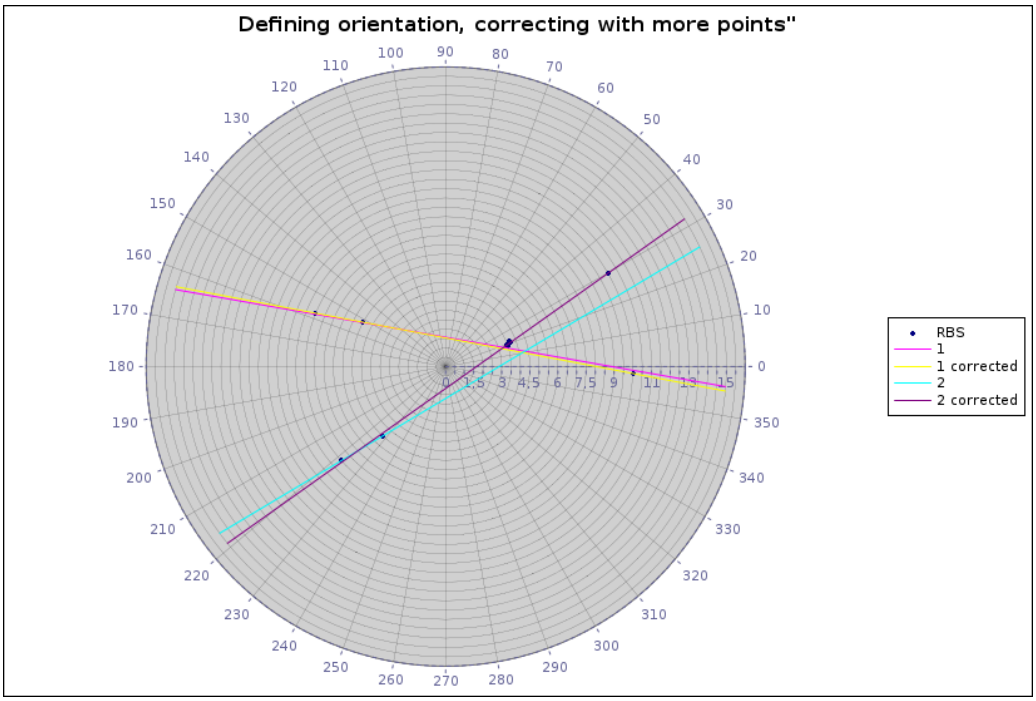

Figure B.1: Stereographic projection of θ and ϕ used to search for the planes, to orient the sample. The θ angle is plotted as the radial distance to the center and the ϕ angle is plotted as the angle done between the point radial line and horizontal. Both angles are plot in degrees.

The angle measured between the two corrected plane lines is calculated as 56.2^{o}, which suggests that the first axis found was the $< 111 >$.

Then the spectrum data was taken, in random directions and along the $< 111 >$. Although due to the high intensity of the data taken for the random angular measurement, before the $< 111 >$ one, a slight redefinition of the $< 111 >$ orientation was needed (table B.1).

Figure B.2 shows the spectrum obtained for the $< 111 >$ axis direction.

Id	θi	θf	$\Delta\theta$	ϕi	ϕf	$\Delta\phi$	minimum θ	minimum ϕ	minimum h	minimum %	normal h
10	3.7	3.7	0	18	26	1	3.7	22	585	15.2	3865

Table B.1:

Comparing detectors

The difference of sensitivity between detectors is obvious in the comparison of the random plots in figure B.3. It is clear that the counting rate is higher in the ring detector, which was to expect, since it has a bigger solid angle. The sharpness is due to the resolution, the higher the resolution the sharper the drop of counting rate, when the energy reaches the backscattering maximum energy. So it is clear that the standard detector has higher resolution.

$< 100 >$ Orientation

To find the next axis ($< 100 >$ orientation), it was expected to be found at 45° of the first axis, so it was necessary to look for it in an angular back scattering scan, searching in the continuity of the sketched line on the ϕ, and then on the θ, as shown in table B.2. The result is plotted in the figure B.4.

The value of the depth is much lower than the minima of the previous center, this is consistent with the definition of this plan as $< 100 >$ and the other as $< 111 >$.

New random and oriented to $< 100 >$ spectra are gathered (figure 3.8).

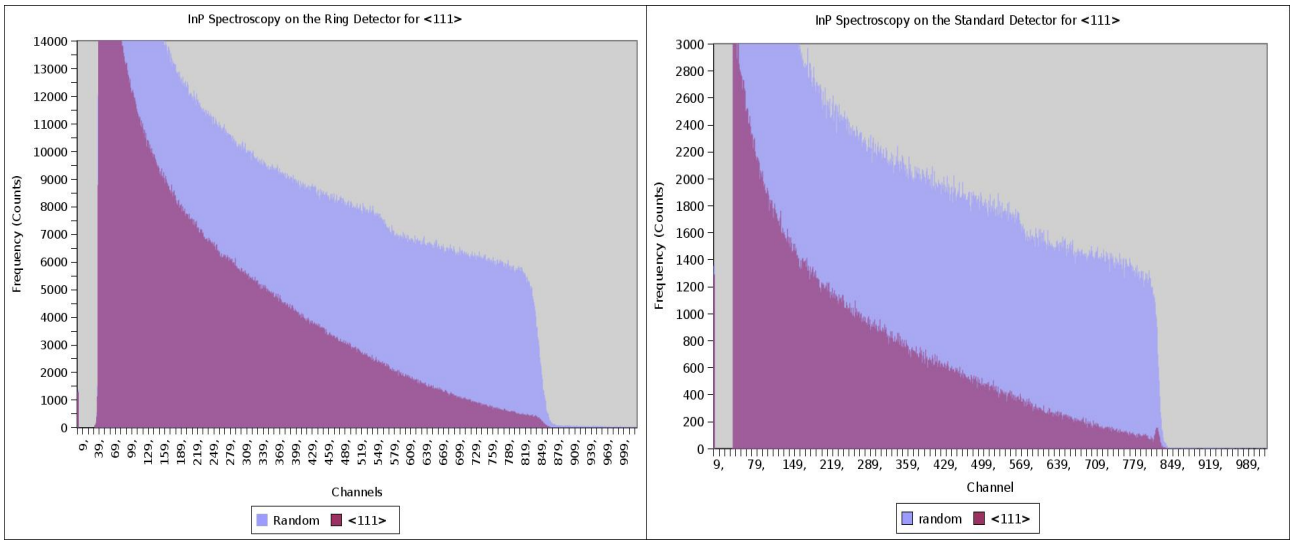

(a) Ring detector (b) Standard detector

Figure B.2: The spectrum of $< 111 >$ orientation

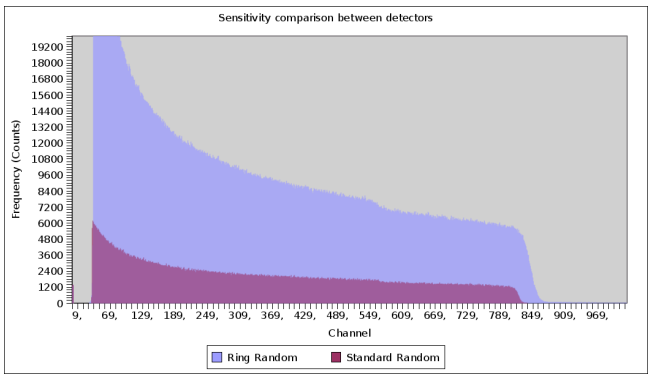

Figure B.3: The random spectrum comparison, between detectors

Id	θi	θf	$\Delta\theta$	ϕi	ϕf	$\Delta\phi$	minimum θ	minimum ϕ	minimum h	minimum %	normal h
11	48	48	0	-18	4	0.4	48	351.2	354	9.2	3890
12	46	52	0.2	-8.8	-8.8	0	48.2	351.2	420	10.9	3899

Table B.2:

Comparing the spectra of both orientations:

Comparison of both orientation results in each detector is shown in figure B.5.

On the ring detector the $< 100 >$ surface peak is more relevant and the counting is allover lower indicating a higher channeling and best crystallization. On the other hand on the standard detector the peak is equal and the counting are slightly different and exclusively on the deeper regions.

Spectrum calibration

The calibration of the Backscattering Spectrometry data aims to correspond an energy to each channel.

The maximum energy, that can result from the elastic collision of α particles with some energy with the known existing atoms of the crystal, back to the detector is calculated.

Considering that a α particle, with mass $m_{He^{2+}}$ and energy E_i, traveling with orientation $\theta_i = 0$ collides with an indium or phosphorus atom of the lattice, with mass m_{In} or m_P respectively. The α particle is redirected in a symmetric direction (θ_α) to that of the atom and equal momentum module. In the direction of the detector the α particles collected must have final energy E_f. The energy loss ratio, in order to get the

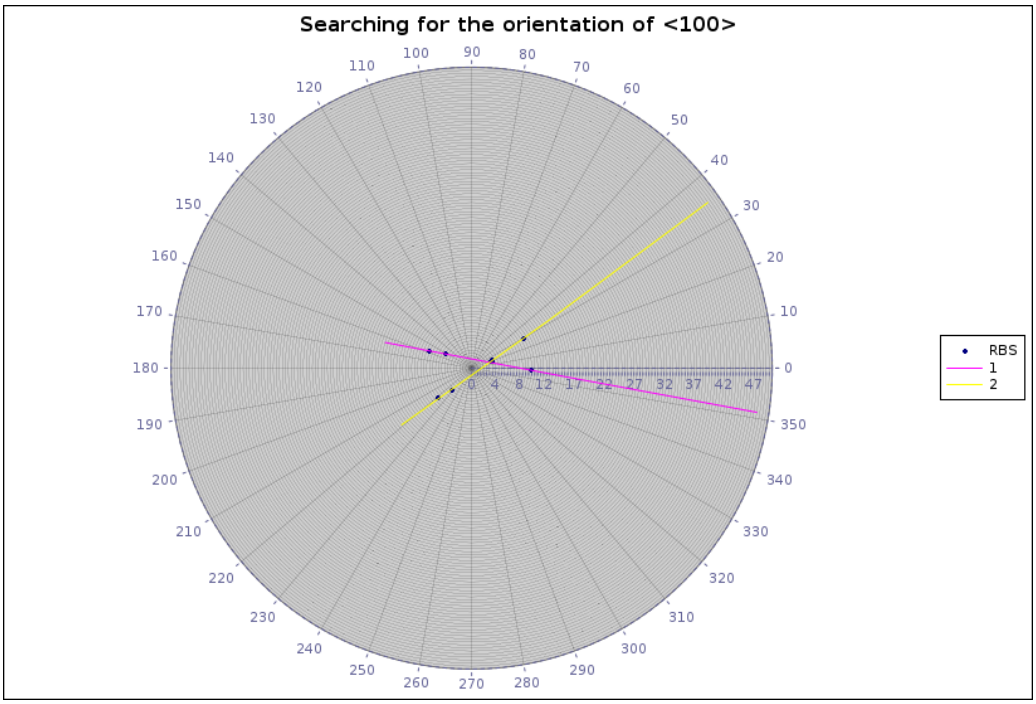

Figure B.4: Plot of the $< 100 >$ orientation

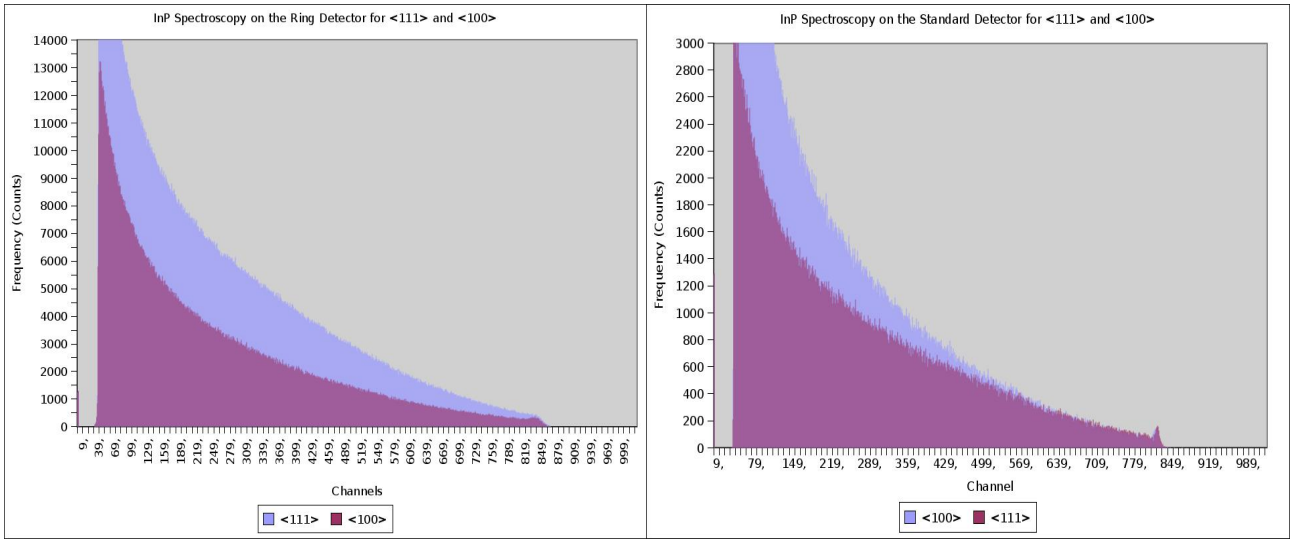

(a) Ring detector

(b) Standard detector

Figure B.5: The spectra of $< 100 >$ and $< 111 >$ orientations

α particle in the detector direction, is given by:

$$k = \frac{E_f}{E_i} = \frac{\sqrt{1 - x^2 \sin^2(\theta)} + x\cos(\theta)}{1 + x} \text{ or } k = \frac{\sqrt{1 - x'^2 \sin^2(\theta)} + x'\cos(\theta)}{1 + x'}, \tag{B.1}$$

in which θ is the angle between the beam and the detector

$$(\theta = \theta_\alpha - \theta_i)$$

and

$$x = \frac{m_{He^2}}{m_{In}} \text{ or } x' = \frac{m_{He^2}}{m_P}$$

is the fraction of masses. The values of maximum energy of the alfa particles collected, for incoming energy of $2MeV$ and for the detectors used are in table B.3.

The calibration on the ring detector, in the form of $E = m \times number\,of\,channels + b$, is in the table

Value	m	x	θ (º)	θ (rad)	K	E_i (MeV)	E_f (MeV)
In det. Ring	114.818	0.03484	180	2.4435	0.8842	2.0000	1.7396
P det. Ring	30.9738	0.12914	180	2.4435	0.6320	2.0000	1.1893
In det standard	114.818	0.03484	140	3.1416	0.8699	2.0000	1.7682
P det standard	30.9738	0.12914	140	3.1416	0.5948	2.0000	1.2635

Table B.3: Maximum ion energy for collisions with In and P

B.4.

The calibration on the standard detector is in the tableB.5.

E (MeV)	channel	m (MeV/channel)	b (MeV)
1.7396	843	0.001955	0.092
1.7396	841		
1.1893	556		
1.1893	565		

Table B.4: Callibration of the ring detector

The calibrations result in the spectrum plots of the figure B.6.

E (MeV)	channel	m (MeV/channel)	b (MeV)
1.7682	824	0.001963	0.1503
1.7682	820		
1.2636	563		
1.2636	567		

Table B.5: Callibration of the standard detector

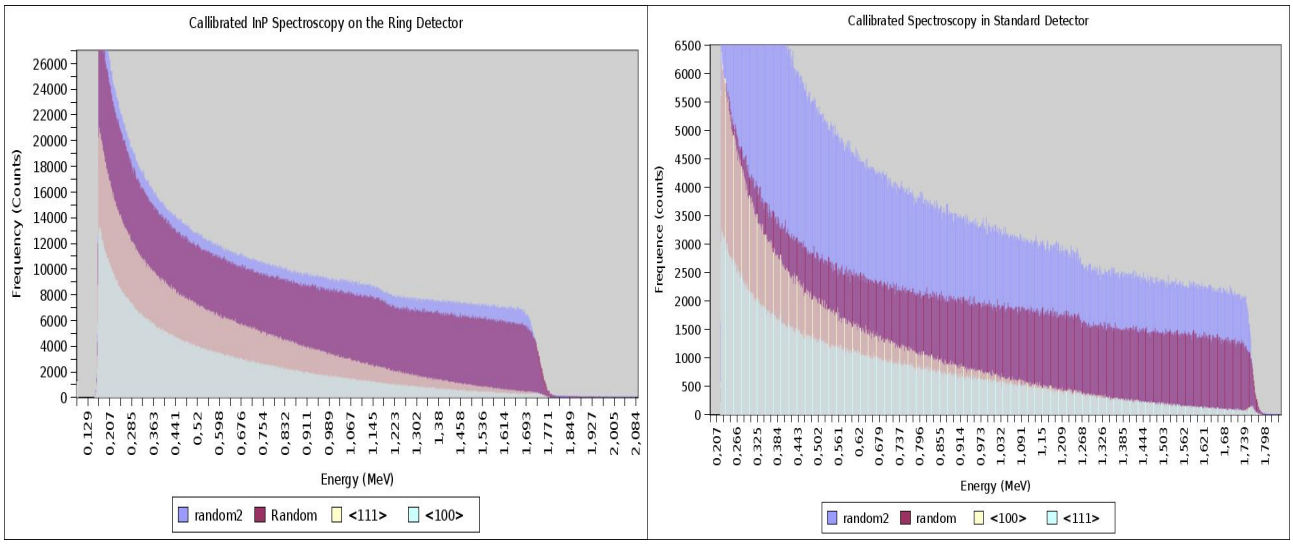

(a) Ring detector

(b) Standard detector

Figure B.6: The calibrated spectra

Depth as a function of energy

The alfa particles lose energy due to the interaction with the atoms along crystal, through their way until they collide,

$$\Delta E = \left(\frac{dE}{dx}\right)\Delta x \tag{B.2}$$

for :- the distance the beam travels within the crystal, Δx; - the atoms included in the stopping process, $S\rho\Delta x$; -an beam area cross- section, S; -density of atoms,

$$\rho = 4,81 g/cm^3 \times NA \times 2/(m_{In} + m_P) = 3.972 \times 10^{22} atoms/cm^3 \tag{B.3}$$

ε is the factor of Stopping Power $\varepsilon \equiv \frac{dE}{\rho dx}$: and is specific of the material used.

$$\varepsilon_{In} = 169.59 \times 10^{-15} eVg^{-1}cm^2; \varepsilon_P = 160.36 \times 10^{-15} eVg^{-1}cm^2; \tag{B.4}$$

The ε of a mixture is given by *the principle of additivity of stopping cross sections*, according to which the InP compound ε given by the weight sum of its elements.

$$\varepsilon_{In\,P} = 1\varepsilon_{In} + 1\varepsilon_P = 3.3 \times 10^{-13} eVg^{-1}cm^2 \tag{B.5}$$

; So the distance corresponding to a channel is given by

$$channel = \frac{m}{\varepsilon\rho} :, \tag{B.6}$$

where

$$m = \frac{\Delta E}{\Delta channel} \tag{B.7}$$

is the ratio used to calibrate. As determined earlier the calibrations are $m_{ring} = 1.955 \times 10^{-3} MeV/channel$ and $m_{standard} = 1.963 \times 10^{-3} MeV/channel$, which means that the depth profile calibrations are given by

$$d_{channel\,ring} = \frac{1.955x10^3}{3.30x10^{-13} \times 3.972 \times 10^{22}} = 1.4911 \times 10^{-7} cm/ch = 1.4911 nm/ch$$

and

$$d_{channel\,standard} = \frac{1.963 \times 10^3}{3.30 \times 10^{-13} \times 3.972 \times 10^{22}} = 1.4976 \times 10^{-7} cm/ch = 1.4976 nm/ch.$$

Surface peak

The surface peak is an evidence of the dechanneling caused by the surface structure disarrangement. The surface's composition is in principle, the same as the rest of the crystal being evidenced, at higher energy of the indium and phosphorus backscattering.

The particles backscattered by the light P atoms have less energy than those scattered by the heavier In. However, particles traveling in and out of the crystal for a longer distance, collided with the heavier In atoms will lose more energy and that makes their energy spectrum overlap with the one produced by particles that hit the P atoms. For this reason one can only analyze, by the "naked eye", the near-to-surface energy spectrum of the backscattered particles by In atoms, free of interference.

Using the depth as function of the energy loss, calculated earlier, the calculus of the peak's depth is reduced to the calculus of the energy interval.

The peaks' length was calculated from the half values of the beginning and the end of the peak.

direction	peak begin	peak end	channels	d (nm)
$< 100 >$	830	843	13	19.38

Table B.6: Surface peek width for the ring detector

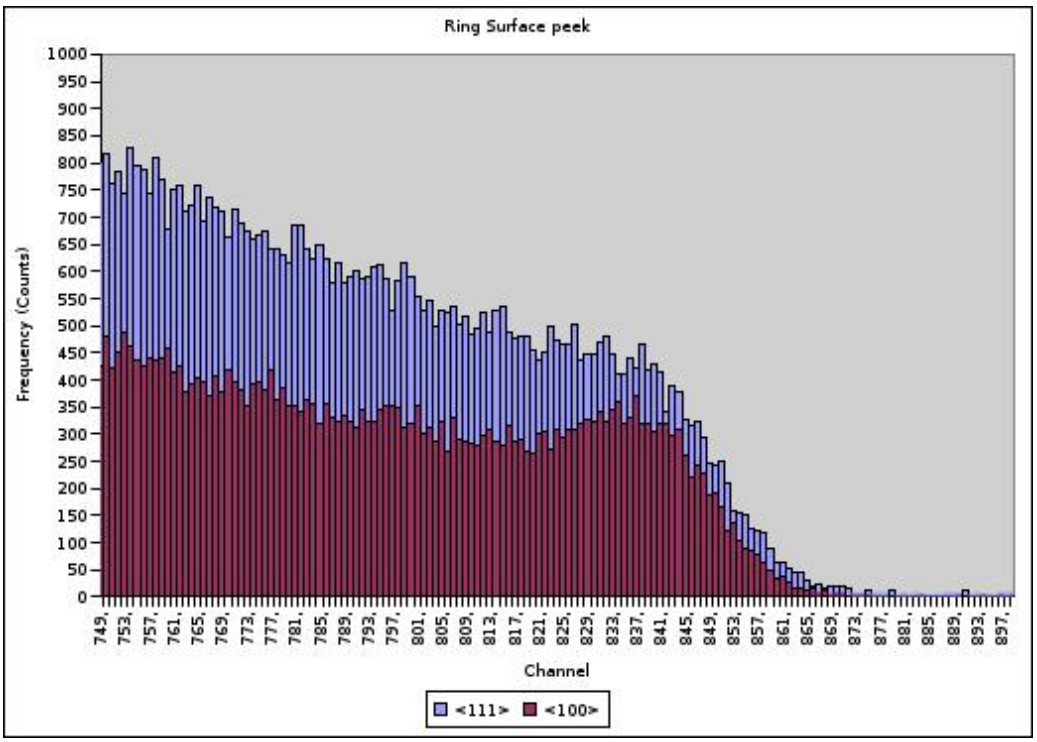

Figure B.7: Surface peek in the ring detector

Surface peek in the ring detector

In the plot of the figure B.7 it is explicit that the $< 100 >$ orientation being the best scattering direction has better evidences of the peak, as for the $< 111 >$ is nearly impossible to measure (table B.6).

The value of the surface peak is very high, corresponding to an energy window of about 25keV, although it must be a consequence of the detector resolution, which is of about 20keV, since the standard detector has a smaller peak and it is supposed to be a measurement of the same physical concept.

Surface peek in the standard detector

In the plot of the figure B.8 both peaks are very visible and their values are in the table B.7.

As the plots show both directions have the same value of surface peak.

direction	peak begin	peak end	channels	d (nm)
$< 100 >$	815	821	6	8.99
$< 111 >$	817	822	5	7.49

Table B.7: Surface peek width for the standard detector

For a better differentiation between the peaks of the standard detector for both directions are plotted in the figure B.9.

The peak is slightly larger for the $< 100 >$ direction, which can be a result of the higher scattering for this direction and so higher manifestation of the defects. The detector's resolution is of 15keV and the peaks correspond to energies of 12keV for the $< 100 >$ orientation and 10keV for the $< 111 >$ orientation, both lower than the detector's resolution.

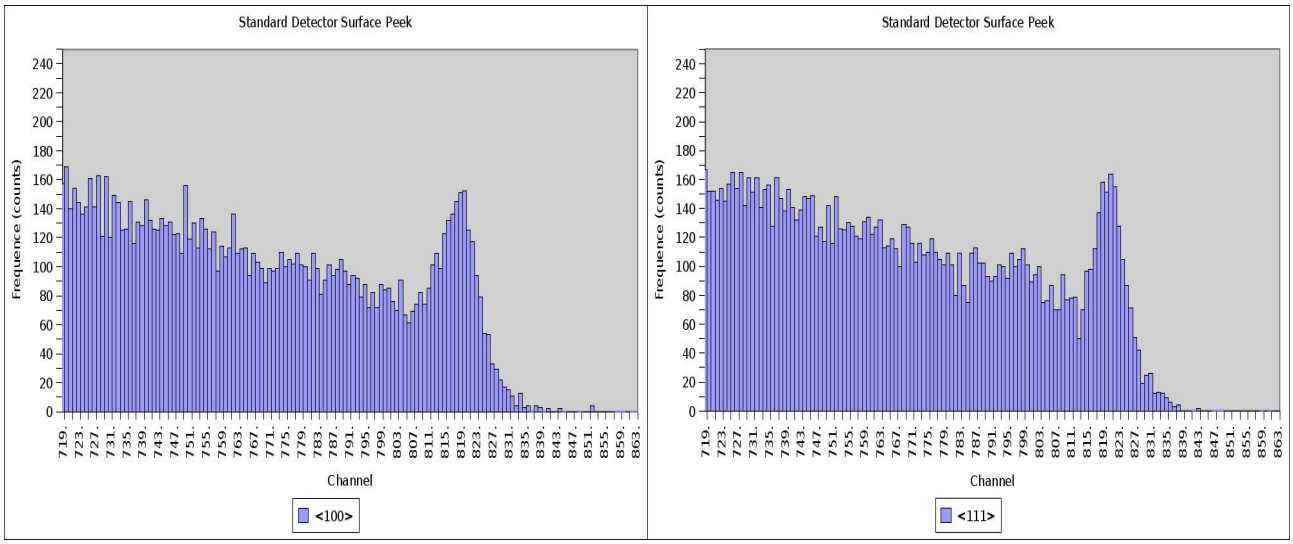

(a) $< 100 >$ orientation (b) $< 111 >$ orientation

Figure B.8: Surface peeks in the standard detector

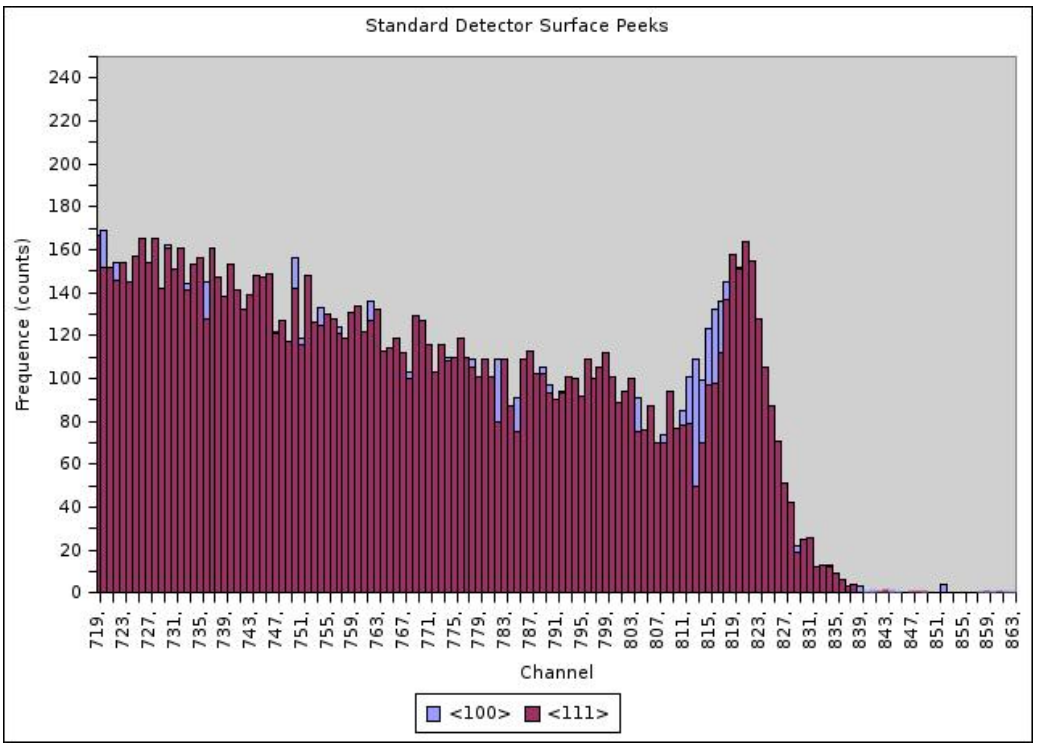

Figure B.9: Surface peeks comparison of the $< 100 >$ and $< 111 >$ directions, for the standard detector

Simulation

For the study of the elements existent in the sample, the comparison of the theoretical simulated data with the obtained spectrum can provide very relevant information. For the simulation the proportion between compounds, the energy of the beam, the existence of any impurity can be taken account, and so the fit of the samples spectroscopy will pronounce any change on these parameters.

Simulating the spectrum for the ring detector, with the values of the table B.8.

The theoretical data was the result of a simulation, with the xrump program [14][1], the parameters used to describe the detection, in table B.8, and the parameters used to describe the geometry of the experience, in

[1], XRUMP is a simulation software, that simulates the backscattering of defined energy ions in samples, as function of the elements in each depth layer.

Detector	θ	ω	Resolution (keV)	Conversion (MeV)	Beam (MeV)
ring	180	25	40	1.63 + 373	2
standard	140	4.5	25	2.17 – 47	2

Table B.8: Detectors parameters

table B.9.

Resulting in the plots of figure B.10.

Theory	Theta	Phi	Charge (uC)	In	P	I (nA)
Ring-< 111 >	5	0	1.8	31	30	1
Standard-< 111 >	-19	0	1.8	31	30	1
Ring-< 100 >	-32	40	2.1	31	30	1
Standard-< 100 >	-55	40	2.1	31	30	1

Table B.9: Experience parameters

The simulation does not take into account the channeling effect, so the comparison is done with the

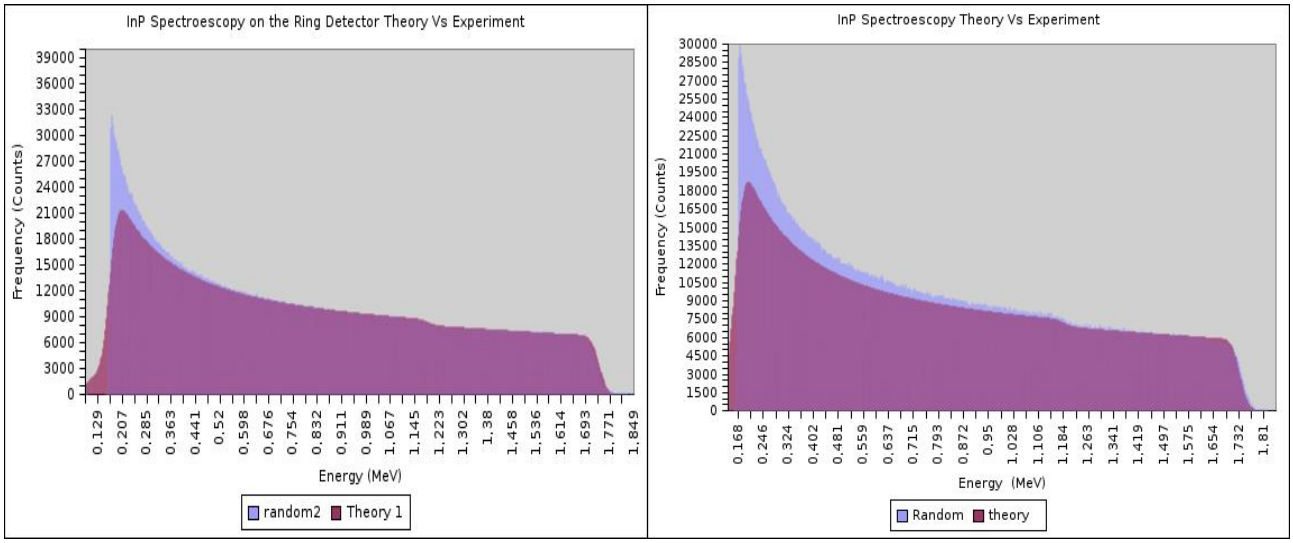

(a) < 100 > orientation in ring detector

(b) < 111 > orientation in ring detector

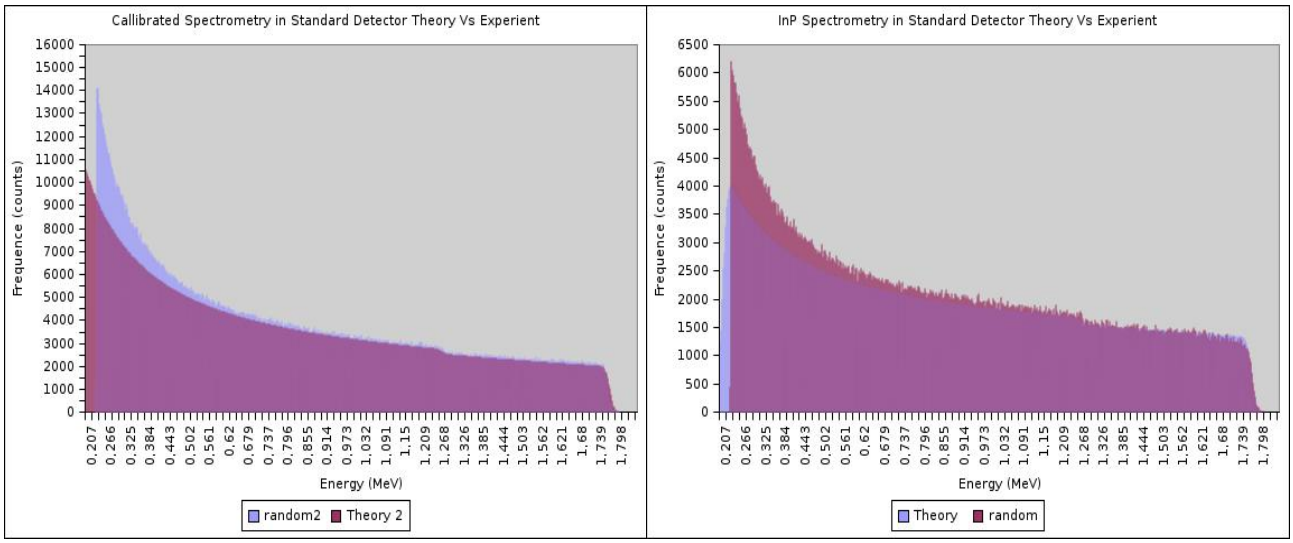

(c) < 100 > orientation in ring detector

(d) < 111 > orientation in ring detector

Figure B.10: Random spectra and respective simulations for each measurement.

random spectra.

As shown in the figure B.10, for the ring detector, the simulation fits perfectly along most energies, corroborating the purity of the sample and the proportionality 1:1 of the InP. Although so, the heavy-side function in the indium higher scattering energy is not as strong, normally it is a consequence of the resolution. The smoothness of the In peek is expected because of resolution loss in the process. The higher count rates for low energy are due to background, since this represent very low energies, those can be from various sources as multi-scatterings and electronics noise.

On the standard detector the simulation approximates better to the data obtained and the resolution discrepancy is lower almost undetectable through all statistical fluctuations.

Crystallization

The crystal structure implies the channeling effect when the beam collides in the orientation of the crystal. Different crystal orientations mean different channeling effects. For the $< 100 >$ direction the channeling should reduce the backscattering even more than the $< 111 >$, as found beneath. A window of 50 channels was used as reagion of interest, ROI, which is the reagion used to calculate the random and the oriented spectra. The values calculated for the reduction of the random to the oriented spectra, which means the fraction between the integral of the random and oriented spectrum, are not that different for the ring detector (figure B.10).

These are very good values of crystallization.

sum random	sum $< 111 >$	crist. $< 111 >$	sum random2	sum $< 100 >$	crist. $< 100 >$	
ring	294150	28741	0.10	350120	16534	0.047
standard	66516	5133	0.08	109541	4726	0.043

Table B.10: Crystallization

The conclusions of the study are described in 3.2

Appendix C
Data about the In isotopes available

Table C.1: The In isotopes available at ISOLDE.-by http://isolde.web.cern.ch/ISOLDE/ in 2008

Yield (atoms/uC)	Nucleus	Half Life	Target	Target density (g/cm2)	Ion Source
1.80E+04	105m	48 s	Ta Metal foil	122	Hot plasma
1.20E+02	105m	48 s	Ta Metal foil	122	Hot plasma
1.30E+04	106m	5.2 min	Ta Metal foil	122	Hot plasma
1.40E+05	106m	5.2 min	Ta Metal foil	122	Hot plasma
1.10E+05	106m	5.2 min	Ta Metal foil	122	Hot plasma
9.90E+05	107m	50.4 s	Ta Metal foil	122	Hot plasma
4.40E+03	107m	50.4 s	Ta Metal foil	122	Hot plasma
2.40E+06	108m	39.6 min	Ta Metal foil	122	Hot plasma
2.70E+06	108m	39.6 min	Ta Metal foil	122	Hot plasma
5.30E+05	108m	39.6 min	Ta Metal foil	122	Hot plasma
8.00E+06	109m	1.34 min	Ta Metal foil	122	Hot plasma
5.80E+06	110m	69.1 min	Ta Metal foil	122	Hot plasma
1.60E+06	110m	69.1 min	Ta Metal foil	122	Hot plasma
1.20E+04	111m	7.7 min	Ta Metal foil	122	Hot plasma
4.20E+08	112m	20.56 min	Ta Metal foil	122	Hot plasma
1.10E+08	116m1		Th/Ta Metal foil/powder	5.5g Th /cm2	Hot plasma
1.50E+05	116m1		Th/Ta Metal foil/powder	5.5g Th /cm2	Hot plasma
5.00E+06	108g	58 min	U Carbide	9.7g U /cm2	Hot plasma at 1950°C
1.70E+07	109g	4.2 hrs	U Carbide	9.7g U /cm2	Hot plasma at 1950°C
4.00E+08	110g	4.9 hrs	U Carbide	9.7g U /cm2	Hot plasma at 1950°C
3.50E+05	111g	2.8049 days	U Carbide	13	W surface
7.20E+08	113g	stable	U Carbide	9.7g U /cm2	Hot plasma at 1950°C
6.30E+06	114g	71.9 s	U Carbide	13	W surface
8.00E+08	114g	71.9 s	U Carbide	9.7g U /cm2	Hot plasma at 1950°C
1.00E+07	116m1		U Carbide	13	W surface
1.60E+08	116g	14.1 s	U Carbide	13	W surface
3.50E+08	117g	43.2 min	U Carbide	13	W surface
4.00E+07	118m1		U Carbide	13	W surface

Continued on Next Page...

Table C.1 – Continued

Yield (atoms/uC)	Nucleus	Half Life	Target	Target density (g/cm2)	Ion Source
7.90E+08	118g	5 s	U Carbide	13	W surface
5.00E+08	119m	18 min	U Carbide	13	W surface
1.00E+09	119g	2.4 min	U Carbide	13	W surface
8.50E+08	119g	2.4 min	U Carbide	65	W surface
6.30E+08	120m1		U Carbide	13	W surface
1.80E+07	120g	3.08 s	U Carbide	13	W surface
4.00E+07	121m	3.88 min	U Carbide	13	W surface
7.00E+08	121g	23.1 s	U Carbide	9.7g U /cm2	Hot plasma at 1950°C
5.60E+08	121g	23.1 s	U Carbide	13	W surface
1.60E+07	122m	10.3	U Carbide	13	W surface
2.50E+08	122g	1.5	U Carbide	13	W surface
5.00E+08	123g	5.98	U Carbide	9.7g U /cm2	Hot plasma at 1950°C
1.40E+08	124g	3.17	U Carbide	13	W surface
7.00E+07	125g	2.36	U Carbide	9.7g U /cm2	Hot plasma at 1950°C
3.20E+07	126g	1.6	U Carbide	13	W surface
2.00E+07	127g	1.15	U Carbide	9.7g U /cm2	Hot plasma at 1950°C
2.50E+06	130g	320	U Carbide	13	W surface
5.00E+05	131g	280	U Carbide	13	W surface
1.00E+05	132g	201	U Carbide	13	W surface
1.10E+03	133g	180	U Carbide	13	W surface

Table C.2: In isotopes' properties -by http://ie.lbl.gov/toi/ in 2008. Where IT means isometric transition, EC means electron conversion, ECx/β^-x means electron capture/beta emission delayed emission of x=p,n.

Nuclide	N	Decay mode	Half life	Ex (keV)	Jp
105In	56	EC	5.07 m ± 0.07	0	(9/2)+
105mIn	56	IT	48 s ± 6	674.1 ± 0.3	(1/2)-
106In	57	EC	6.2 m ± 0.1	0	7+
106mIn	57	EC	5.2 m ± 0.1	28.6 ± 0.3	(3+)
107In	58	EC	32.4 m ± 0.3	0	9/2+
107mIn	58	IT	50.4 s ± 0.6	678.5 ± 0.3	1/2-
108In	59	EC	58.0 m ± 1.2	0	7+
108mIn	59	EC	39.6 m ± 0.7	29.75 ± 0.05	2+
109In	60	EC	4.2 h ± 0.1	0	9/2+
109mIn	60	IT	1.34 m ± 0.07	650.1 ± 0.3	1/2-
109m2In	60	IT	0.209 s ± 0.006	2101.8 ± 0.2	(19/2+)
110In	61	EC	4.9 h ± 0.1	0	7+
110mIn	61	EC	69.1 m ± 0.5	62.09 ± 0.04	2+
111In	62	EC	2.8047 d ± 0.0005	0	9/2+
111mIn	62	IT	7.7 m ± 0.2	536.95 ± 0.06	1/2-
112In	63	β^-,EC	14.97 m ± 0.10	0	1+
112mIn	63	IT	20.56 m ± 0.06	156.59 ± 0.05	4+
116In	67	β^-,e	14.10 s ± 0.03	0	1+
116mIn	67	β^-	54.29 m ± 0.17	127.267 ± 0.006	5+
116m2In	67	IT	2.18 s ± 0.04	289.660 ± 0.006	8-
118In	69	β^-	5.0 s ± 0.5	0	1+
118mIn	69	β^-	4.45 m ± 0.05	60	5+
119In	70	β^-	2.4 m ± 0.1	0	9/2+
119mIn	70	β^-,IT	18.0 m ± 0.3	311.37 ± 0.03	1/2-

Continued on Next Page...

Table C.2 – Continued

Nuclide	N	Decay mode	Half life	Ex (keV)	Jp
120In	71	β^-	3.08 s ± 0.08	0	1+
120mIn	71	β^-	46.2 s ± 0.8	0+x	(3,4,5)+
120m2In	71	β^-	47.3 s ± 0.5	0+y	(8-)
121In	72	β^-	23.1 s ± 0.6	0	9/2+
121mIn	72	β^-,IT	3.88 m ± 0.10	313.69 ± 0.10	1/2-
122In	73	β^-	1.5 s ± 0.3	0	1+
122mIn	73	β^-	10.3 s ± 0.6	0+x	5+
122m2In	73	β^-	10.8 s ± 0.4	200	8-
123In	74	β^-	5.98 s ± 0.06	0	9/2+
123mIn	74	β^-	47.8 s ± 0.5	327.21 ± 0.04	1/2-
124In	75	β^-	3.11 s ± 0.10	0	3+
124mIn	75	β^-	3.7 s ± 0.2	50	(8-)
125In	76	β^-	2.36 s ± 0.04	0	9/2(+)
125mIn	76	β^-	12.2 s ± 0.2	360.12 ± 0.09	1/2(-)
126In	77	β^-	1.60 s ± 0.10	0	3(+)
126mIn	77	β^-	1.64 s ± 0.5	102 ± 64	7-,8-,9-
127In	78	β^-,β^-n	1.09 s ± 0.01	0	(9/2+)
127mIn	78	β^-,β^-n	3.67 s ± 0.04	462 ± 71	(1/2-)
130In	81	β^-,β^-n	0.32 s ± 0.02	0	1(-)
130mIn	81	β^-,β^-n	0.55 s ± 0.01	50 ± 50	(10-)
130m2In	81	β^-,β^-n	0.55 s ± 0.01	400 ± 60	(5+)
131In	82	β^-,β^-n	0.282 s ± 0.005	0	(9/2+)
131mIn	82	β^-,β^-n,IT	0.35 s ± 0.05	363 ± 37	(1/2-)
131m2In	82	β^-,β^-n	0.32 s ± 0.06	4.27E+3 ± 1.7E2	(21/2+)
132In	83	β^-,β^-n	0.201 s ± 0.013	0	(7-)
133In	84	β^-,β^-n	180 ms ± 1.5	0	(9/2+)

Appendix D
Atomic-Electron Binding Energies

Table D.1: Atomic-Electron Binding Energies.-by LBNL Isotopes Project - LUNDS Universitet Nuclear Data [1] Dissemination Home Page (http://ie.lbl.gov/toi.html)

El	K	L1	L2	L3	M1	M2	M3	M4	M5	N1	N2	N3	N4	N5
1 H	0.0136													
2 He	0.0246													
3 Li	0.0548	0.0053												
4 Be	0.1121	0.0080												
5 B	0.1880	0.0126	0.0047	0.0047										
6 C	0.2838	0.0180	0.0064	0.0064										
7 N	0.4016	0.0244	0.0092	0.0092										
8 O	0.5320	0.0285	0.0071	0.0071										
9 F	0.6854	0.0340	0.0086	0.0086										
10 Ne	0.8701	0.0485	0.0217	0.0216										
11 Na	1.0721	0.0633	0.0311	0.0311	0.0007									
12 Mg	1.3050	0.0894	0.0514	0.0514	0.0021									
13 Al	1.5596	0.1177	0.0732	0.0727	0.0007	0.0055	0.0055							
14 Si	1.8389	0.1487	0.0995	0.0989	0.0076	0.0030	0.0030							
15 P	2.1455	0.1893	0.1362	0.1353	0.0162	0.0099	0.0099							
16 S	2.4720	0.2292	0.1654	0.1642	0.0158	0.0080	0.0080							
17 Cl	2.8224	0.2702	0.2016	0.2000	0.0175	0.0068	0.0068							
18 Ar	3.2060	0.3263	0.2507	0.2486	0.0292	0.0159	0.0158							
19 K	3.6074	0.3771	0.2963	0.2936	0.0339	0.0178	0.0178							
20 Ca	4.0381	0.4378	0.3500	0.3464	0.0437	0.0254	0.0254							
21 Sc	4.4928	0.5004	0.4067	0.4022	0.0538	0.0323	0.0323	0.0066	0.0066					
22 Ti	4.9664	0.5637	0.4615	0.4555	0.0603	0.0346	0.0346	0.0037	0.0037					
23 V	5.4651	0.6282	0.5205	0.5129	0.0665	0.0378	0.0378	0.0022	0.0022					
24 Cr	5.9892	0.6946	0.5837	0.5745	0.0741	0.0425	0.0425	0.0023	0.0023					
25 Mn	6.5390	0.7690	0.6514	0.6403	0.0839	0.0486	0.0486	0.0033	0.0033					
26 Fe	7.1120	0.8461	0.7211	0.7081	0.0929	0.0540	0.0540	0.0036	0.0036					
27 Co	7.7089	0.9256	0.7936	0.7786	0.1007	0.0595	0.0595	0.0029	0.0029					
28 Ni	8.3328	1.0081	0.8719	0.8547	0.1118	0.0681	0.0681	0.0036	0.0036					
29 Cu	8.9789	1.0961	0.9510	0.9311	0.1198	0.0736	0.0736	0.0016	0.0016					
30 Zn	9.6586	1.1936	1.0428	1.0197	0.1359	0.0866	0.0866	0.0081	0.0081					
31 Ga	10.3671	1.2977	1.1423	1.1154	0.1581	0.1068	0.1029	0.0174	0.0174	0.0015	0.0008	0.0008		
32 Ge	11.1031	1.4143	1.2478	1.2167	0.1800	0.1279	0.1208	0.0287	0.0287	0.0050	0.0023	0.0023		
33 As	11.8667	1.5265	1.3586	1.3231	0.2035	0.1464	0.1405	0.0412	0.0412	0.0085	0.0025	0.0025		
34 Se	12.6578	1.6539	1.4762	1.4358	0.2315	0.1682	0.1619	0.0567	0.0567	0.0120	0.0056	0.0056		
35 Br	13.4737	1.7820	1.5960	1.5499	0.2565	0.1893	0.1815	0.0701	0.0690	0.0273	0.0052	0.0046		
36 Kr	14.3256	1.9210	1.7272	1.6749	0.2921	0.2218	0.2145	0.0950	0.0938	0.0275	0.0147	0.0140		
37 Rb	15.1997	2.0651	1.8639	1.8044	0.3221	0.2474	0.2385	0.1118	0.1103	0.0293	0.0148	0.0140		
38 Sr	16.1046	2.2163	2.0068	1.9396	0.3575	0.2798	0.2691	0.1350	0.1331	0.0377	0.0199	0.0199		
39 Y	17.0384	2.3725	2.1555	2.0800	0.3936	0.3124	0.3003	0.1596	0.1574	0.0454	0.0256	0.0256	0.0024	0.0024
40 Zr	17.9976	2.5316	2.3067	2.2223	0.4303	0.3442	0.3305	0.1824	0.1800	0.0513	0.0287	0.0287	0.0030	0.0030
41 Nb	18.9856	2.6977	2.4647	2.3705	0.4684	0.3784	0.3630	0.2074	0.2046	0.0581	0.0339	0.0339	0.0032	0.0032

Continued on Next Page...

Table D.1 – Continued

El	K	L1	L2	L3	M1	M2	M3	M4	M5	N1	N2	N3	N4	N5
42 Mo	19.9995	2.8655	2.6251	2.5202	0.5046	0.4097	0.3923	0.2303	0.2270	0.0618	0.0348	0.0348	0.0018	0.0018
43 Tc	21.0440	3.0425	2.7932	2.6769	0.5440	0.4449	0.4250	0.2564	0.2529	0.0680	0.0389	0.0389	0.0020	0.0020
44 Ru	22.1172	3.2240	2.9669	2.8379	0.5850	0.4828	0.4606	0.2836	0.2794	0.0749	0.0431	0.0431	0.0020	0.0020
45 Rh	23.2199	3.4119	3.1461	3.0038	0.6271	0.5210	0.4962	0.3117	0.3070	0.0810	0.0479	0.0479	0.0025	0.0025
46 Pd	24.3503	3.6043	3.3303	3.1733	0.6699	0.5591	0.5315	0.3400	0.3347	0.0864	0.0511	0.0511	0.0015	0.0015
47 Ag	25.5140	3.8058	3.5237	3.3511	0.7175	0.6024	0.5714	0.3728	0.3667	0.0952	0.0626	0.0559	0.0033	0.0033
48 Cd	26.7112	4.0180	3.7270	3.5375	0.7702	0.6507	0.6165	0.4105	0.4037	0.1076	0.0669	0.0669	0.0093	0.0093
49 In	27.9399	4.2375	3.9380	3.7301	0.8256	0.7022	0.6643	0.4508	0.4431	0.1219	0.0774	0.0774	0.0162	0.0162
50 Sn	29.2001	4.4647	4.1561	3.9288	0.8838	0.7564	0.7144	0.4933	0.4848	0.1365	0.0886	0.0886	0.0239	0.0239
51 Sb	30.4912	4.6983	4.3804	4.1322	0.9437	0.8119	0.7656	0.5369	0.5275	0.1520	0.0984	0.0984	0.0314	0.0314
52 Te	31.8138	4.9392	4.6120	4.3414	1.0060	0.8697	0.8187	0.5825	0.5721	0.1683	0.1102	0.1102	0.0398	0.0398
53 I	33.1694	5.1881	4.8521	4.5571	1.0721	0.9305	0.8746	0.6313	0.6194	0.1864	0.1227	0.1227	0.0496	0.0496
54 Xe	34.5644	5.4528	5.1037	4.7822	1.1487	1.0021	0.9406	0.6894	0.6767	0.2133	0.1455	0.1455	0.0695	0.0675
55 Cs	35.9846	5.7143	5.3594	5.0119	1.2171	1.0650	0.9976	0.7395	0.7255	0.2308	0.1723	0.1616	0.0788	0.0765
56 Ba	37.4406	5.9888	5.6236	5.2470	1.2928	1.1367	1.0622	0.7961	0.7807	0.2530	0.1918	0.1797	0.0925	0.0899
57 La	38.9246	6.2663	5.8906	5.4827	1.3613	1.2044	1.1234	0.8485	0.8317	0.2704	0.2058	0.1914	0.0989	0.0989
58 Ce	40.4430	6.5488	6.1642	5.7234	1.4346	1.2728	1.1854	0.9013	0.8833	0.2896	0.2233	0.2072	0.1100	0.1100
59 Pr	41.9906	6.8348	6.4404	5.9643	1.5110	1.3374	1.2422	0.9511	0.9310	0.3045	0.2363	0.2176	0.1132	0.1132
60 Nd	43.5689	7.1260	6.7215	6.2079	1.5753	1.4028	1.2974	0.9999	0.9777	0.3152	0.2433	0.2246	0.1175	0.1175
61 Pm	45.1840	7.4279	7.0128	6.4593	1.6500	1.4714	1.3569	1.0515	1.0269	0.3310	0.2420	0.2420	0.1204	0.1204
62 Sm	46.8342	7.7368	7.3118	6.7162	1.7228	1.5407	1.4198	1.1060	1.0802	0.3457	0.2656	0.2474	0.1290	0.1290
63 Eu	48.5190	8.0520	7.6171	6.9769	1.8000	1.6139	1.4806	1.1606	1.1309	0.3602	0.2839	0.2566	0.1332	0.1332
64 Gd	50.2391	8.3756	7.9303	7.2428	1.8808	1.6883	1.5440	1.2172	1.1852	0.3758	0.2885	0.2709	0.1405	0.1405
65 Tb	51.9957	8.7080	8.2516	7.5140	1.9675	1.7677	1.6113	1.2750	1.2412	0.3979	0.3102	0.2850	0.1470	0.1470
66 Dy	53.7885	9.0458	8.5806	7.7901	2.0468	1.8418	1.6756	1.3325	1.2949	0.4163	0.3318	0.2929	0.1542	0.1542
67 Ho	55.6177	9.3942	8.9178	8.0711	2.1283	1.9228	1.7412	1.3915	1.3514	0.4357	0.3435	0.3066	0.1610	0.1610
68 Er	57.4855	9.7513	9.2643	8.3579	2.2065	2.0058	1.8118	1.4533	1.4093	0.4491	0.3662	0.3200	0.1767	0.1676
69 Tm	59.3896	10.1157	9.6169	8.6480	2.3068	2.0898	1.8845	1.5146	1.4677	0.4717	0.3859	0.3366	0.1796	0.1796
70 Yb	61.3323	10.4864	9.9782	8.9436	2.3981	2.1730	1.9498	1.5763	1.5278	0.4872	0.3967	0.3435	0.1981	0.1849
71 Lu	63.3138	10.8704	10.3486	9.2441	2.4912	2.2635	2.0236	1.6394	1.5885	0.5062	0.4101	0.3593	0.2048	0.1950
72 Hf	65.3508	11.2707	10.7394	9.5607	2.6009	2.3654	2.1076	1.7164	1.6617	0.5381	0.4370	0.3804	0.2238	0.2137
73 Ta	67.4164	11.6815	11.1361	9.8811	2.7080	2.4687	2.1940	1.7932	1.7351	0.5655	0.4648	0.4045	0.2413	0.2293
74 W	69.5250	12.0998	11.5440	10.2068	2.8196	2.5749	2.2810	1.8716	1.8092	0.5950	0.4916	0.4253	0.2588	0.2454
75 Re	71.6764	12.5267	11.9587	10.5353	2.9317	2.6816	2.3673	1.9489	1.8829	0.6250	0.5179	0.4444	0.2737	0.2602
76 Os	73.8708	12.9680	12.3850	10.8709	3.0485	2.7922	2.4572	2.0308	1.9601	0.6543	0.5465	0.4682	0.2894	0.2728
77 Ir	76.1110	13.4185	12.8241	11.2152	3.1737	2.9087	2.5507	2.1161	2.0404	0.6901	0.5771	0.4943	0.3114	0.2949
78 Pt	78.3948	13.8805	13.2726	11.5638	3.2976	3.0270	2.6453	2.2015	2.1211	0.7240	0.6076	0.5191	0.3307	0.3138
79 Au	80.7249	14.3528	13.7336	11.9187	3.4249	3.1478	2.7430	2.2911	2.2057	0.7588	0.6437	0.5454	0.3520	0.3339
80 Hg	83.1023	14.8393	14.2087	12.2839	3.5616	3.2785	2.8471	2.3849	2.2949	0.8030	0.6810	0.5769	0.3785	0.3593
81 Tl	85.5304	15.3467	14.6979	12.6575	3.7041	3.4157	2.9566	2.4851	2.3893	0.8455	0.7213	0.6090	0.4066	0.3862
82 Pb	88.0045	15.8608	15.2000	13.0352	3.8507	3.5542	3.0664	2.5856	2.4840	0.8936	0.7639	0.6445	0.4352	0.4129
83 Bi	90.5259	16.3875	15.7111	13.4186	3.9991	3.6963	3.1769	2.6876	2.5796	0.9382	0.8053	0.6789	0.4636	0.4400
84 Po	93.1000	16.9280	16.2370	13.8100	4.1520	3.8440	3.2930	2.7940	2.6800	0.9870	0.8510	0.7150	0.4950	0.4690
85 At	95.7240	17.4820	16.7760	14.2070	4.3100	3.9940	3.4090	2.9010	2.7810	1.0380	0.8970	0.7510	0.5270	0.4990
86 Rn	98.3970	18.0480	17.3280	14.6100	4.4730	4.1500	3.5290	3.0120	2.8840	1.0900	0.9440	0.7900	0.5580	0.5300
87 Fr	101.130	18.6340	17.8990	15.0250	4.6440	4.3150	3.6560	3.1290	2.9940	1.1480	0.9990	0.8340	0.5970	0.5670
88 Ra	103.915	19.2320	18.4840	15.4440	4.8220	4.4830	3.7850	3.2480	3.1050	1.2080	1.0550	0.8790	0.6360	0.6030
89 Ac	106.756	19.8460	19.0810	15.8700	4.9990	4.6550	3.9150	3.3700	3.2190	1.2690	1.1120	0.9240	0.6760	0.6400
90 Th	109.650	20.4720	19.6930	16.3000	5.1820	4.8310	4.0460	3.4910	3.3320	1.3300	1.1680	0.9670	0.7130	0.6770
91 Pa	112.596	21.1050	20.3140	16.7330	5.3610	5.0010	4.1740	3.6060	3.4420	1.3830	1.2170	1.0040	0.7430	0.7080
92 U	115.602	21.7580	20.9480	17.1680	5.5480	5.1810	4.3040	3.7260	3.5500	1.4410	1.2710	1.0430	0.7790	0.7370
93 Np	118.669	22.4270	21.6000	17.6100	5.7390	5.3660	4.4350	3.8490	3.6640	1.5010	1.3280	1.0850	0.8160	0.7710
94 Pu	121.791	23.1040	22.2660	18.0570	5.9330	5.5470	4.5630	3.9700	3.7750	1.5590	1.3800	1.1230	0.8460	0.7980
95 Am	124.982	23.8080	22.9520	18.5100	6.1330	5.7390	4.6980	4.0960	3.8900	1.6200	1.4380	1.1650	0.8800	0.8290
96 Cm	128.241	24.5260	23.6510	18.9700	6.3370	5.9370	4.8380	4.2240	4.0090	1.6840	1.4980	1.2070	0.9160	0.8620
97 Bk	131.556	25.2560	24.3710	19.4350	6.5450	6.1380	4.9760	4.3530	4.1270	1.7480	1.5580	1.2490	0.9550	0.8980
98 Cf	134.939	26.0100	25.1080	19.9070	6.7610	6.3450	5.1160	4.4840	4.2470	1.8130	1.6200	1.2920	0.9910	0.9300
99 Es	138.396	26.7820	25.8650	20.3840	6.9810	6.5580	5.2590	4.6170	4.3680	1.8830	1.6830	1.3360	1.0290	0.9650
100 Fm	141.926	27.5740	26.6410	20.8680	7.2080	6.7760	5.4050	4.7520	4.4910	1.9520	1.7490	1.3790	1.0670	1.0000
101 Md	146.526	28.3870	27.4380	21.3560	7.4400	7.0010	5.5520	4.8890	4.6150	2.0240	1.8160	1.4240	1.1050	1.0340
102 No	149.208	29.2210	28.2550	21.8510	7.6780	7.2310	5.7020	5.0280	4.7410	2.0970	1.8850	1.4690	1.1450	1.0700
103 Lr	152.970	30.0830	29.1030	22.3590	7.9300	7.4740	5.8600	5.1760	4.8760	2.1800	1.9630	1.5230	1.1920	1.1120
104 Rf	156.288	30.8810	29.9860	22.9070	8.1610	7.7380	6.0090	5.3360	5.0140	2.2370	2.0350	1.5540	1.2330	1.1490

[1] The binding energies given in Table D.1 are those reported by Larkins[31] mainly from the compilations of Sevier[32] (for Z≤83) and of Porter and Freedman[33] (for Z≥84). All binding energies listed are for solid sys-tems referenced to the Fermi level, except those for Ne, Cl, Ar, Br, Kr, Xe, and Rn. These latter binding energies are for vapor-phase systems referenced to the vacuum level.

The binding energies are accurate to better than 1-2 eV for most of the subshells in the lighter ele-ments, and for the outer orbitals in the heavier elements. Uncertainties may be as large as 10 or 20 eV forthe inner orbitals in the high-Z elements, and changes

in chemical state can lead to substantial shifts in the binding energies of non-valence shells.[34] Bearden and Burr[35] reevaluated existing data on x-ray emission wavelengths and discussed binding energies determined from atomic energy-level differences.

Bibliography

General sources

[1] Ulrich Wahl, "Emission channeling:charged particle-solid interaction, detection and lattice location methods" , Instituto Tecnológico e Nuclear, Submitted to the University of Lisbon as part of the process of "Agregação".

[2] Ulrich Wahl, "Advances in electron emission channeling measurments in semi-conductors", 2000 Hyperfine Interactions, Volume 129, Numbers 1-4.

[3] Ulrich Wahl, "Position-sensitive Si pad detectors for electron emission channeling experiments",Nuclear Instruments and Methods in Physics Research Section A: Accelerators, Spectrometers, Detectors and Associated Equipment, Volume 524, Issues 1-3, 21 May 2004, Pages 245-256

[4] Sadao Adachi, "Properties of Group-IV, III-V and II-VI Semiconductors", Wiley Series in Materials for Electronic&Optoelectronic Applications, John Wiley & SonsS, 2005.

[5] N J Carron, "An Introduction to the Passage of Energetic Particles through Matter", ATK Mission Research Corporation, Santa Barbara, California, USA

[6] Ionizing Radiation Standards Group Institute for National Measurement Standards National Research Council Canada web page, http://www.irs.inms.nrc.ca/EGSnrc/pirs701/node43.html.

[7] "Principles of Charged Particle Acceleration", Stanley Humphries, Jr. Department of Electrical and Computer Engineering University of New Mexico, John Wiley & Sons, 1999

[8] "Fundamentals Of Surface And Thin Film Analysis", Leonard C. Feldman- AT&T Bell Laboratories, James W. Mayer-Department of Materials Sience and Engeneering Cornell University, North-Holland

[9] T. Bjørnstad, "Methods for production of intense beams of unstable nuclei:New developments at ISOLDE", Physica Scripta Vol. 34, 578-590, 1986.

[10] ISOLDE web page, "http://isolde.web.cern.ch/ISOLDE/".

[11] ISOLDE Yield database, "https://oraweb.cern.ch/els/isolde/query_tgt".

[12] Lígia Amorim , "Installation of a cryogenic station to perform Emission Channeling experiments at low temperature", Submited to the Faculty of Science University of Lisbon as Intern Report.

[13] H. Hofsaess, U. Wahl and S.G. Jahn, Hyperfine Interactions 84 (1994) 27.

[14] L.R. Doolittle, Nucl. Instrum. Methods, B 9 (1985), p. 344. XRUMP Rutherford Backscattering Spectroscopy analysis package, "http://www.genplot.com/RUMP/index.htm"

[15] SRIM, The *S*topping and *R*ange of *I*ons in *M*atter, "http://www.srim.org/"

[16] Ulrich Whal, "Emission channeling studies of Li in semiconductors", Physics Reports 280(3&4) 145-286 (1997)

Literature on the compound

[17] "CRC Handbook of Chemestry and Physics 2008", chapter 12 - L.I.Berger,"properties of semiconductors"

[18] Katsunori Yamaguchi, Yoshiyuki Chiba, Masakito Yoshizama and Kazuo Kameda, " Low temperature specific heat of GaP, InP, GaAs and InAs compounds", J. Japan Inst. Metals, Vol.60, N.12 (1996), pp. 1181-1186.

[19] Ulrich Piesbergen, " Die durchschnittischen atomwärmen der $A^{III} - B^{V}$ - halbleiter AlSb, GaAs, GaSb, InP, InAs, InSb und die atomiwärmen des elements germanum zwischen 12 und 273K", Physikalish-Chemischen Institut der Universität des elements, 1963.

[20] J.F. Vetelino, S.P. Gaur, and S.S. Mira: "Debye-Waller factor for zinc-blende type crystals", Physical Review B 5 (1972) 2360-2366.

[21] M.S Kushawa: "Compressibilities, Debye-Waller factors, and melting criteria for II-VI and III-V compound semiconductors", Physical Review B (1981) 2115-2120.

[22] D.N. Talwar: "On Debye-Waller factors and melting criteria of II-VI and III-V compounds", Journal of Physics C: Solid State Physics 7 (1974) 2981-2988.

[23] E.F Steigmeier: "The Debye temperatures of III-V compounds", Applied Physics Letters 3 (1963) 6-8.

[24] R. Pässler: "Basic moments of phonon density of states spectra and characteristic phonon temperatures of group IV, III-V, and II-VI materials", Journal of Applied Physics 101 (2007) 093513/1-12.

[25] R. Saravanan, S.K. Mohanlal, and K.S. Chandrasekaran: "An X-ray search for anharmonicity in indium phosphide", Zeitschrift fuer Kristallographie 200 (1992) 7-13

[26] N.N. Sirota: "...", Acta Cryst. A 25 (1969) 223.

[27] V.T. Bublik and S.S. Gorelik: "...", Krist. Tech. 12 (1977) 859. [Shumskii 71] M.G. Shumskii, V.T. Bublik, S.S. Gorelik, and M.A. Gorevich: "...", Sov. Phys. Crystallogr. 16 (1971) 674.

[28] O.H. Nielsen, F.K. Larsen, S. Damgaard, J.W. Petersen, and G. Weyer: "Systematic experimental and theoretical studies of the lattice vibrations of host atoms and substitutional Sn impurities in III-V semiconductors", Zeitschrift für Physik B 52 (1983) 99-109.

[29] P.A. Doyle and P.S. Turner: "Relativistic Hartree -Fock X-ray and electron scattering factors", Acta Crystollographica A 25 (1968) 390.

[30] Sadao Adachi, Department of Electronic Engineering Gunma University Japan, "Properties of Group-IV, III–V and II–VI Semiconductors", Wiley Series in Materials for Electronic and Optoelectronic Applications.

Literature for the ion binding energy

[31] F.B. Larkins, At. Data and Nucl. Data Tables 20, 313 (1977).

[32] K.D. Sevier, Low Energy Electron Spectrometry, Wiley-Interscience, New York (1972).

[33] F.T, Porter and M.S. Freedman, J. Phys. Chem. Ref. Data 7, 1267 (1978).

[34] D.A. Shirley, R.L. Martin, S.P. Kowalczyk, F.R. McFeely, and L. Ley, Phys. Rev. B15, 544 (1977).

[35] J.A. Bearden and A.F. Burr, Rev. Mod. Phys. 39, 125 (1967).

Images sources

[36] http://hyperphysics.phy-astr.gsu.edu/hbase/nuclear/imgnuc/ruthgeo.gif

[37] http://wlap.physics.lsa.umich.edu/cern/lectures/academ/2000/wilson/01/real/slides/img007.gif

[38] http://isolde.web.cern.ch/ISOLDE/normal/isoprodsc.html

[39] "Table of Isotopes", Version 1.0 March/1996, Richard B. Firestone, Virginia S. Shirley Editor, S.Y. Frank Chu CD-ROM Editor, Coral M. Baglin and Jean Zipkin Assistant Editors

[40] K. Haruna et al, J. Phys. C 20 (1987) 5275.

[41] http://guweb2.gonzaga.edu/faculty/cronk/chemistry/images/carnot-cycle.gif

[42] http://upload.wikimedia.org/wikipedia/commons/2/22/Sphalerite-unit-cell-depth-fade-3D-balls.png

Sources on table contents

[43] LBNL Isotopes Project Nuclear Data Dissemination Home Page. Retrieved March 11, 2002, from "http://ie.lbl.gov/toi.html".

[44] "http://www.ioffe.ru/SVA/NSM/Semicond/InP/basic.html"

[45] "http://www.ioffe.ru/SVA/NSM/Semicond/InP/thermal.html"

[46] "http://www.webelements.com/indium/bond_enthalpies.html"-(with references - J.A. Kerr in CRC Handbook of Chemistry and Physics 1999-2000 : A Ready-Reference Book of Chemical and Physical Data (CRC Handbook of Chemistry and Physics, D.R. Lide, (ed.), CRC Press, Boca Raton, Florida, USA, 81st edition, 2000)